Fabrication and Studies of a-Si:H Thin Films and Single Side c-Si(n)/a-Si:H(p) Heterojunction Solar Cells

A thesis submitted

by

Venkanna Kanneboina

Roll No: 126121019

In partial fulfillment of the requirement for the award of the degree of

Doctor of Philosophy

Department of Physics
Indian Institute of Technology Guwahati
Guwahati - 781 039, Assam, India

November 2018

TH-2097_126121019

DECLARATION

The work contained in this thesis entitled "**Fabrication and Studies of a-Si:H Thin Films and Single Side c-Si(n)/a-Si:H(p) Heterojunction Solar Cells**" has been carried out by me under the supervision of Dr. Pratima Agarwal, Professor, Department of Physics, Indian Institute of Technology, Guwahati, Assam, India. This thesis does not contain any materials previously submitted for the award of any degree or diploma.

Date: 28th November, 2018

Venkanna Kanneboina
Roll No: 126121019
Department of Physics
Indian Institute of Technology Guwahati
Guwahati-781039, Assam, India

TH-2097_126121019

भारतीय प्रौद्योगिकी संस्थान गुवाहाटी
Indian Institute of Technology Guwahati
North Guwahati, Guwahati
PIN- 781 039, Assam State, INDIA
Phone: +91 361 2583000 Extn 2702, 2582702
Fax: +91 361 2690 762 (Institute), 2582749 (Department)

Dr. Pratima Agarwal
Professor
Department of Physics
E-mail:pratima@iitg.ernet.in

Dated: Nov 28, 2018

Certificate

This is certified that the work contained in this thesis entitled **"Fabrication and Studies of a-Si:H Thin Films and Single Side c-Si(n)/a-Si:H(p) Heterojunction Solar Cells"** submitted by Mr. Venkanna Kanneboina, a Ph. D. student at Department of Physics, Indian Institute of Technology, Guwahati, Assam, India, for the award of the degree of Doctor of Philosophy, has been carried out under my supervision. This work has not been submitted elsewhere for the award of any degree or diploma.

(Dr. Pratima Agarwal)

TH-2097_126121019

Dedicated

to

My Parents

(Smt. Venkatamma and Sri. Ramulu),

Paternal Uncle (Sri. Uppalaiah)

and My Friends

TH-2097_126121019

Acknowledgements

First of all, I would like to express my sincere gratitude to my thesis supervisor, Prof. Pratima Agarwal, for giving the opportunity to carry out my doctoral study under her supervision. I am very thankful to her for help, support, encouragement and motivation throughout my Ph.D research work. I am very thankful to her for giving the opportunity to learn many experimental techniques, critical analysis and understanding of different topics. I would like to thank her for sharing knowledge and valuable suggestions on many things.

I would like to thank my doctoral committee members Dr. Ashwini Kumar Sharma (Chairman), Dr. D. Pamu and Prof. Roy Paily Palathinkal for their valuable suggestions, advices, critical review of my research work and fruitful discussions at various stages of my research work.

I express my sincere thanks to the former and present Head of the Department of Physics Prof. Saurabh Basu, Prof. Poulose Poulose and Prof. Subradip Gosh, for their encouragement and allowing me to use departmental facilities throughout my research work. I am also thankful to Prof. Perumal Alagarsamy, Prof. Girish Sampath Setlur, Prof. Subhradip Gosh, Dr. Charudatt Y Kadolkar, Prof. Bipul Buyan, Dr. Tarak Nath Dey for their teaching during course work and all other faculty members of the Physics department.

I also thank to Department of Science and Technology (DST) and Defence Research and Development Organization (DRDO), New Delhi, India for providing fund to install multi-chamber RFPECVD and HWCVD system for deposition of Si films and solar cells.

I am thankful to Dr. Sidanada Sarma, scientific officer, Dept. of Physics, for his help throughout my research work.

My special thanks to Mr. Basab Bijoy Purkayastha for his help during external quantum efficiency measurement setup and other technical and office staff.

I am grateful to Prof. S. C. Agarwal, visiting faculty in the Department of Physics for valuable discussions in different area of research.

TH-2097_126121019

I would like to acknowledge my lab mates Dr. Himanshu S. Jha, Dr. Mukesh Singh, Dr. Lalhriatzuala, Dr. Asha Yadav, Dr. Ramakrishna Madaka, Mr. Pilik Basumatary, Ms. Juhi kumari, Mr. Manvendra Singh Gangwar, Ms. Jaishree Bharadwaj, Mr. Vivek Ghritlahre, Ms. Shubhangi Bhardwaj and Ms. Niharika Gogoi for creating friendly atmosphere and help throughout my research work.

I would like to thank CIF, IIT Guwahati for using CIF facilities. I am also thankful to former and present HOC Prof. G. Krishnamoorthy and Prof. Mohammed Qureshi, technical officers Mr. Chandan Borgohain, Mr. Madhurjya Borah, Dr. Kula Senapati, Dr. Kesho Singh and Dr.Ashim Malakar.

I would like to thank Prof. P. K. Iyer, Department of Chemistry, for allowing me to do some measurements in his lab.

My special thanks to Mr. Subash Pai (M/s Excel Instruments, Mumbai) for fabricating the multi-chamber RFPECVD system and other instruments as per our design and requirements. I would like to thank Mr. Pramod Prajapathi, Mr. Jeeth Lal and team, M/s Excel Instruments and Mr. Ranjan Kumar Sahoo and team, Pfeiffer vacuum for their responsible service and technical support.

I am very fortunate to have friends, Dr. Santhosh Kumar, Dr. Munendar Pathi, Dr. Rajendar Padam, Dr. Mahesh Peddigari, Dr. Sunil Kumar, Dr. Anil Kumar, Dr. Ravi Kumar Patta, Dr. Rajendar Gone, Dr. Ranganatha Gopal Rao, Mr. Harikrishna Veldandi, Mr. Srinivas, Mr. Jagan who supported me during my research work.

I also thank to my batch mates and friends Dr. Anil, Kallol, Ramiz, Dr.Sudin, Rahul, Abhijith, Dr. Anabil, Sahoo, Bibuti, Saurabh, Omkar, Dr. Ashish, Prahlad, Ram, Dr. Kaushik, Biswaranjan, Kamal, Dr. Junmoni , Dr.Ranjan.

I am thankful to all my friends, seniors, juniors and research scholars, of Department of Physics for their help and wonderful time shared with me.

I would like to thank Dept. of Physics, IIT Guwahati and MHRD for financial support.

I would like to thank my paternal uncle Mr. Uppalaiah for his care, guidance and encouragement since childhood onwards.

TH-2097_126121019

I will be very thankful to God and Goddess for giving positive energy, spiritual motivation, luck and fate.

Finally, my parents are true inspiration to me. Their dedication, hard work, courage, struggle and responsibility taught great lessons to me, which I never found anywhere. I could not find suitable word to say thanks to my parents and family. I think the only way to be thankful to them is to take care of them forever.

Venkanna Kanneboina,
IIT Guwahati.

TH-2097_126121019

Preface

Solar energy demand is growing rapidly due to rapid increase in world's population, power utilization and living life style. Silicon based solar cells are best alternate to fulfil energy need of world's population. The c-Si/a-Si:H heterojunction solar cells have remarkable advantages over c-Si and also a-Si:H based solar cells. The conversion efficiency of c-Si/a-Si:H heterojunction solar cells is comparable with c-Si based solar cells. The c-Si/a-Si:H heterojunction solar cells can be easily fabricated at temperature below 200 ^{o}C, whereas junction formation in conventional c-Si solar cells is usually done by a thermal diffusion step, for which temperature of 800-1000 ^{o}C is needed. This low temperature enables the use of thinner wafers, thermal budget during the heterojunction formation is also considerably reduced compared to homojunction formation. The time required to form the heterojunction and deposit contact layers is also shorter for heterojunctions than for conventional c-Si solar cells. The heterojunction silicon solar cells exhibit a smaller drop in performance with increasing temperature in comparison with conventional c-Si solar cells. In heterojunction solar cells improved surface passivation and reduced recombination losses results in higher open circuit voltage (V_{oc}) values compared to homojunction solar cells. The main motivation of the present thesis work had been to fabricate with high efficiency and open circuit voltage single side c-Si/a-Si:H heterojunction solar cells. Based on this motivation, the objective of the present thesis work had been:

- Optimization of deposition conditions of intrinsic and doped a-Si:H films by different processes such as hydrogen plasma treatment and other parameters.
- Fabrication of c-Si/a-Si:H heterojunction solar cells and study the properties of individual layers and interfaces of cells by different characterization tools.
- Improve the efficiency of solar cells by difference processes such H_2 plasma treatment at interfaces, surface passivation, optimization of layer thickness and doping concentration.

The present thesis contains 8 chapters. Chapter 1 presents the brief introduction of different photovoltaic technology, fabrication and characterization of c-Si/a-Si:H heterojunction solar cells including literature review. Chapter 2 presents a brief description of deposition process of a-Si:H thin films and c-Si/a-Si:H heterojunction solar cells by RFPECVD technique. This chapter also contain discussion on different characterization techniques that are used to the study the structural,

TH-2097_126121019

optical, electrical and morphological properties of a-Si:H and ITO thin films and also performance of c-Si/a-Si:H heterojunction solar cells. Chapter 3 presents the influence of intermittent hydrogen plasma treatment on properties of a-Si:H films during deposition. In order to improve the microstructure, optical and electrical of the a-Si:H films, hydrogen plasma has been introduced during growth of the a-Si:H films. The evolution of nanocrystalline Si phase due to intermittent hydrogen plasma treatment is studied through Ex-Situ Spectroscopic Ellipsometry(SE), Raman, TEM and FTIR absorption spectroscopy. Chapter 4 presents influence of hydrogen flow rate on the microstructure and optical properties of a-Si:H(p) and a-Si:H(n) films. A series of a-Si:H(p) and a-Si:H(n) films were deposited using RFPECVD technique by varying the hydrogen flow rate (HFR) in the range of 30-70 SCCM and 30-80 SCCM respectively. The SE measurements have been performed on these films to study microstructure, thickness, optical bandgap and volume fractions (void, amorphous and crystalline) and also surface roughness. Chapter 5 presents the influence of deposition temperature on microstructure, morphology, optical and electrical properties of Indium tin oxide (ITO) thin films. In order to optimize the deposition parameters to get high quality TCO, ITO thin films were deposited by varying deposition temperature from 50 to 200 ^{o}C by using RF Sputtering technique. These ITO films were characterized by different techniques. Chapter 6 presents the influence of a-Si:H(i) thickness on the performance of the c-Si/a-Si:H heterojunction solar cells. One sided c-Si/a-Si:H heterojunction solar cells (*Ag/Al/c-Si(n)/a-Si:H(i)/a-Si:H(p)/ITO/Ag*) were fabricated by RFPECVD technique in multi-chamber system. The cells were fabricated with hydrogen plasma treatment of a-Si:H(i) layer of different thicknesses prior to the deposition of top a-Si:H(p) layer. The thickness, optical band gap and microstructure of different a-Si:H layers in the cells were estimated using SE. This chapter also presents the influence of H_2 plasma treatment on performance of solar cells, which resulted in record high V_{oc} of the SHJ solar cells. Spectral response of the solar cells was measured by quantum efficiency (QE) technique. Chapter 7 deals with influence of boron doping concentration and thickness of a-Si:H(p) layer on the performance of the *Ag/Al/c-Si(n)/a-Si:H(i)/a-Si:H(p)/ITO/Ag* solar cells. The V_{oc}, J_{sc}, FF and efficiency (η) of solar cells were estimated by *I-V* measurements. EQE measurements were carried out on the cells with and without external reverse bias to study interface properties and significance of electric field at interface. Chapter 8 presents overall conclusions of present thesis work and also future scope of this research area is included in this chapter.

TH-2097_126121019

List of Abbreviations and Symbols

AFM	Atomic force microscope
Ag	Silver
Al	Aluminium
Ar	Argon
a-Si	Amorphous silicon
a-Si:H	Hydrogenated amorphous silicon
BEMA	Bruggeman effective medium approximation
CCD	Charge coupled device
c-Si	Crystalline silicon
Cu	Copper
CVD	Chemical vapor deposition
CZ	Czochralski
D	Operator
DBFR	Diborane (B_2H_6) flow rate
DC	Direct current
DI	Deionized water
Dep. rate	Deposition rate
Dep. temp	Deposition temperature
EQE	External quantum efficiency
FESEM	Field emission scanning electron microscopy
Fig.	Figure
FTIR	Fourier transform infrared spectroscopy
FWHM	Full width at half maxima
HCl	Hydrogen chloride
HFR	Hydrogen flow rate
HF	Hydrogen fluoride
HPT	Hydrogen plasma treatment
HRTEM	High resolution transmission electron microscopy
IR	Infrared
ITO	Indium tin oxide
LA	Longitudinal acoustic
LO	Longitudinal optical
MRO	Medium range order
nc-Si:H	Hydrogenated nano crystalline silicon
PFR	Phosphine flow rate
PP	Process pressure
PVD	Physical vapor deposition
RFPECVD	Radio frequency plasma enhanced chemical vapor deposition
SAED	Selective area electron diffraction
SCCM	Standard cubic centimeter per minute
SE	Spectroscopic ellipsometry
SFR	Silane (SiH_4) flow rate
SHJ	Silicon heterojunction
Si	Silicon
SR	Spectral response
SRO	Short range order
TA	Transverse acoustic
TCO	Transparent conducting oxide
TEM	Transmission electron microscopy
TL	Tauc-Lorentz
TO	Transverse optical
UV-Vis-NIR	Ultraviolet visible near infrared
XRD	X-Ray diffraction
b_s	Incident spectral photon flux density
d	Thickness of film
d_{layer}	Layer thickness
d_{bulk}	Bulk layer thickness
d_i	a-Si:H(i) or i- layer thickness
d_p	a-Si:H(p) or p- layer thickness
d_s	Surface roughness
d_{RMS}	RMS surface roughness
d_{XRD}	Crystallite size
k	Extinction coefficient
k_{XRD}	Proportionality constant (Scherrer constant)
l	length
n	Refractive index

TH-2097_126121019

Symbol	Description
n_i	Ideality factor
t	Separation or distance
I	Current
V	Voltage
J	Current density
J_0	Saturation current density
J_{sc}	Short circuit current density
J_{ill}	Illumination current density
J_{ph}	Photo current density
J_{dark}	Dark current density
P_{in}	Input power density
P_{out}	Output power density
V_{oc}	Open circuit voltage
FF	Fill factor
η	Efficiency
R_s	Series resistance
R_{sh}	Shunt resistance
R_{sheet}	Sheet resistance
$\Delta\theta$	Tetrahedral bond angle deviation
α_a	Absorption coefficient
Γ_{TO}	Full width at half maxima of TO mode
B	Broadening due to crystallite size
β_{hkl}	Full width at half maxima (FWHM) (in radian)
ρ	Resistivity
ϵ	Strain
$< \varepsilon(E) >$	Pseudo dielectric function
$< \varepsilon_1(E) >$	Real part of pseudo dielectric function
$< \varepsilon_2(E) >$	Imaginary part of pseudo dielectric function
$\varepsilon_{eff}(E)$	Effective dielectric function
$\varepsilon_i(E)$	Dielectric function of ith phase
f_i	Volume fraction of ith phase
f_v	Void fraction
f_a	Amorphous fraction
f_c	Crystalline fraction
A	Amplitude parameter
C	Broadening parameter
C_H	Hydrogen content
R^*	Microstructure parameter
E_0	Band to band transition energy
E	Photon energy
E_g	Optical bandgap
E_A	Activation energy
λ	Wavelength
h	Planks constant
ν	Frequency
ω	wavenumber
σ	Conductivity
σ_d	Dark conductivity
σ_{ph}	Photo conductivity
σ_a	FWHM of the oscillator
σ_0	Pre factor
K_B	Boltzmann constant
T	Temperature in kelvin
$\Delta\omega$	Shift from peak position of c-Si
ψ	Amplitude ratio
Δ	Phase difference
ρ_{SE}	Polarization ratio
r_p and r_s	Complex Fresnel reflection coefficients of *p*- and *s*-polarized light
θ_0	Angle of incidence.
q	Electron charge

TH-2097_126121019

Contents

Declaration i
Certificate ii
Dedication iii
Acknowledgements iv
Preface vii
List of Abbreviations and Symbols ix
Contents xi
List of Figures xv
List of Tables xix
Chapter 1: Introduction 1
1.1 Silicon photovoltaic technology 3
1.2 c-Si/a-Si:H heterojunction solar cells 3
1.3 Limiting issues for the solar cells 5
1.4 Motivation, objectives and content of the thesis 6
1.5 References 9
Chapter 2: Experimental Techniques 15
2.1 Preparation of thin films and solar cells 15
2.1.1 Radio frequency plasma enhanced chemical vapour deposition technique 15
2.1.1.1 Growth mechanism of a-Si:H thin films........ 17
2.1.2 RF sputtering technique........ 17
2.1.3 Fabrication of solar cells........ 18
2.1.3.1 Crystalline silicon cleaning process........ 18
2.2 Characterization techniques........ 19
2.2.1 Raman Scattering spectroscopy........ 19
2.2.2 Transmission electron microscopy technique........ 21
2.2.3 Spectroscopic Ellipsometry (SE)........ 21
2.2.3.1 Tauc-Lorentz model........ 23
2.2.3.2 Bruggeman effective medium approximation model....... 23
2.2.3.3 Gauss model........ 24

TH-2097_126121019

2.2.4 X-Ray diffraction technique…………………………………………… 24
2.2.5 Fourier transform infrared spectroscopy ……………………………….. 25
2.2.6 UV-Vis-NIR spectroscopy ………………………………………………... 26
2.2.7 Field emission scanning electron microscopy…………………………. 27
2.2.8 Atomic force microscopy ……………………………………………….. 27
2.2.9 Current-Voltage (*I-V*) measurements…………………………………… 28
2.2.9.1 *I-V* measurements of a-Si:H thin films…………………….... 28
2.2.9.2 Four probe *I-V* measurement of ITO thin films………….. 28
2.2.9.3 Current-Voltage (*I-V*) measurements of solar cells……… 29
2.2.10 External quantum efficiency (EQE) measurements……………….. 30
2.3 References………………………………………………………………………….. 32
Chapter 3: Influence of Hydrogen Plasma Treatment on Microstructural, Optical and Electrical Properties of a-Si:H(i) Thin Films………………………………………….. 37
3.1 Experimental details ………………………….. 37
3.2 Results and discussion…………………………………………………………… 38
3.2.1 Structure evaluation by TEM analysis ……………………………… 38
3.2.2 Structure evaluation by Raman studies……………………………… 39
3.2.3 FTIR analysis for the evaluation of hydrogen content …………… 41
3.2.4 UV-Vis-NIR studies for band gap and thickness evaluation……… 42
3.2.5 SE analysis for evaluation of optical constants and microstructure. 43
3.2.6 Morphology studies by AFM……………………………………… 51
3.2.7 Electrical conductivity……………………………………………….. 52
3.3 Conclusion……………………………………………………………………….. 53
3.4 References……………………………………………………………………….. 54
Chapter 4: Influence of Hydrogen Flow Rate on Microstructural and Optical Properties of a-Si:H(p) and a-Si:H(n) Thin Films…………………………………... 59
4.1 Experimental details……………………………………………………….... 59
4.2 Results and discussion………………………………………………………… 60
4.2.1 Influence of hydrogen flow rate on a-Si:H(p) films……………… 60
4.2.1.1 SE studies……………………………………………………... 60
4.2.1.2 UV-Vis-NIR studies………………………………………….. 64
4.2.1.3 AFM morphology studies…………………………………….. 64
4.2.2 Influence of hydrogen flow rate on a-Si:H(n) films……………… 65

TH-2097_126121019

4.2.2.1 SE studies 65
4.2.2.2 UV-Vis-NIR studies.......... 69
4.2.2.3 AFM morphology studies.......... 70
4.3 Conclusion.......... 71
4.4 References.......... 72
Chapter 5: Influence of Deposition Temperature on Structural, Optical and Electrical Properties of ITO Thin Films.......... 75
5.1 Experimental details.......... 75
5.2 Results and discussion.......... 76
5.2.1 X-ray diffraction analysis 76
5.2.2 UV-Vis-NIR spectroscopy studies.......... 77
5.2.3 FESEM morphology studies.......... 78
5.2.4 AFM morphology studies 79
5.2.5 Four probe *I-V* measurements.......... 80
5.3 Conclusion.......... 80
5.4 References.......... 81
Chapter 6: Influence of a-Si:H(i) Layer Thickness on the Performance of c-Si/a-Si:H Heterojunction Solar Cells.......... 83
6.1 Experimental details.......... 83
6.1.1 Fabrication of c-Si/a-Si:H heterojunction solar cells.......... 83
6.2 Results and discussion.......... 85
6.2.1 Spectroscopic ellipsometry analysis.......... 85
6.2.2 FESEM morphology studies.......... 94
6.2.3 AFM morphology studies.......... 95
6.2.4 Current-Voltage measurement.......... 96
6.2.5 Quantum efficiency measurement.......... 99
6.3 Conclusion.......... 101
6.4 References.......... 101
Chapter 7: Influence of Boron Doping and Thickness of a-Si:H(p) Layer on the Performance of c-Si/a-Si:H Heterojunction Solar Cells.......... 105
7.1 Experimental details.......... 105
7.1.1 Fabrication of c-Si/a-Si:H heterojunction solar cells.......... 105
7.2 Results and discussion.......... 106

TH-2097_126121019

7.2.1 Current voltage measurement of solar cells………………………….. 106
7.2.2 Quantum efficiency measurement of solar cells…………………... 109
7.3 Conclusion………………………………………………………………….. 112
7.4 References………………………………………………………………….. 112
Chapter 8: Conclusions and Future Scope……………………..……………………… 115
8.1 Thesis conclusions ….…………………………………………………………. 115
8.2 Future scope………………………………………………………………………. 117
Appendix ………………………………………………………………………………. 119
List of Publications ……………………………………………………………………. 121

TH-2097_126121019

List of Figures

1.1 Best solar cell efficiency with different materials and technology by different groups........ 2

1.2 PV industry global annual production by different region in recent years............ 2

1.3 Schematic band bending diagram of single side and double side c-Si(n)/a-Si:H(p) heterojunction solar cells........ 4

2.1 Multi chamber RFPECVD and HWCVD system........ 16

2.2 Schematic diagram and possible reactions of growth mechanism of a-Si:H films. 17

2.3 (a). Schematic of SE and (b). Real image of spectroscopic ellipsometer instrument........ 22

2.4 Current density-voltage (*J-V*) characteristics of solar cell under dark and illumination........ 29

2.5 Schematic diagram of quantum efficiency measurement setup........ 31

3.1 Hydrogen plasma treatment steps during a-Si:H film growth........ 38

3.2 (a,b) TEM images of *HP_0*, *HP_3* films and (c,d) SAED patterns of *HP_0*, *HP_3* films and (e) HRTEM image of *HP_3* film........ 39

3.3 Raman spectra of *HP_0* to *HP_3* (a) and deconvulated spectra of *HP_2* (b) films 40

3.4 Ratio of I_{TA} to I_{TO} (I_{TA}/I_{TO}) and bond angle deviations as a function of number of H_2 plasma steps........ 41

3.5 FTIR transmission spectra of *HP_0* to *HP_3* films........ 42

3.6 Hydrogen content and microstructure factor of *HP_0* to *HP_3* films as a function of H_2 plasma steps........ 42

3.7 Transmission spectra of *HP_0* to *HP_3* films........ 43

3.8 Thickness, band gap (E_g) and refractive index plotted as function of H_2 plasma steps........ 43

3.9 a) Real ($< \varepsilon_1 >$) and b) Imaginary ($< \varepsilon_2 >$) part of pseudo dielectric function measured as a function of photon energy for *HP_0* to *HP_3* films and c-Si........ 44

3.10 a) Schematic Two-layer model for TL, TL+Gauss and b) TL +BEMA model..... 45

3.11 Measured and fitted values of real ($< \varepsilon_1 >$) and imaginary ($< \varepsilon_2 >$) part of pseudo dielectric function as a function of photon energy, a) *HP_0*, *HP_1* films (fitted with TL model) and b) *HP_2*, *HP_3* films (fitted with TL and Gauss

TH-2097_126121019

model).. 46
3.12 Measured and fitted values of $<\varepsilon_1>$ and $<\varepsilon_2>$ as a function of photon energy, a) *HP_0*, *HP_1* films and b) *HP_2*, *HP_3* films (fitted with TL and BEMA model).. 47
3.13 Void and crystalline fraction plotted as function of H_2 plasma steps................ 48
3.14 Surface and RMS roughness of films as a function of number of H_2 plasma steps 49
3.15 Microstructure factor and void fraction as a function of number of H_2 plasma steps.. 50
3.16 a) Refractive index and b) excitation coefficient of *HP_0* to *HP_3* films measured as a function of photon energy by using TL and BEMA model......... 50
3.17 TL model parameters (A, E_0, E_g and C) of *HP_0-HP_3* films as a function of hydrogen content (C_H).. 51
3.18 (a-d). Surface morphology of *HP_0 - HP_3* films measured from AFM measurements.. 52
3.19 Room temperature conductivity of films as a function of number of H_2 plasma steps.. 53
3.20 The dark and photo conductivity of *HP_0* to *HP_3* films as a function of temperature.. 53
4.1 a) Real ($<\varepsilon_1>$) and b) Imaginary ($<\varepsilon_2>$) part of pseudo dielectric function measured as a function of photon energy of a-Si:H(p) films along with c-Si substrate. In case of c-Si, the spectra are normalised by a factor of two to fit in the range.. 61
4.2 (a, b). Measured and fitted (TL model) values of real ($<\varepsilon_1>$) and imaginary ($<\varepsilon_2>$) part of pseudo dielectric function of a-Si:H(p) films as a function of photon energy.. 61
4.3 TL model fitted parameters (A, E_0, C and E_g) of a-Si:H(p) film as a function of HFR.. 62
4.4 (a, b). Measured and fitted (BEMA model) values of $<\varepsilon_1>$ and $<\varepsilon_2>$ of a-Si:H(p) films as a function of photon energy.. 63
4.5 Void, amorphous and crystalline volume fractions of a-Si:H(p) film corresponding to HFR.. 64
4.6 Transmission spectra of a-Si:H(p) thin films... 64
4.7 (a-e). AFM surface morphology of *MP120-MP124* films............................ 65

TH-2097_126121019

4.8 a) Real ($< \varepsilon_1 >$) and b) Imaginary ($< \varepsilon_2 >$) part of pseudo dielectric function measured as a function of photon energy for a-Si:H(n) films along with c-Si substrate.......... 66
4.9 (a, b): Measured and fitted (TL model) values of $< \varepsilon_1 >$ and $< \varepsilon_2 >$ of a-Si:H(n) films as a function of photon energy.......... 66
4.10 TL model fitted parameters (A, E_0, C and E_g) of a-Si:H(n) film as a function of HFR.......... 67
4.11 (a, b). Measured and fitted (BEMA model) values of $< \varepsilon_1 >$ and $< \varepsilon_2 >$ of a-Si:H(n) films as a function of photon energy.......... 68
4.12 Void, amorphous and crystalline volume fractions of a-Si:H(n) film corresponding to HFR.......... 69
4.13 The UV-Vis-NIR transmission spectra of a-Si:H(n) thin films.......... 69
4.14 (a-f). AFM surface morphology of *MN87-MN92* films.......... 70
5.1 (a) XRD pattern of *SP335-SP338* ITO films, (b) Fitted peaks in *SP338* film...... 76
5.2 Williamson-Hall plot of *SP338* ITO thin film.......... 77
5.3 (a). UV-Vis-NIR transmission spectra, (b). Plot of $(\alpha h\nu)^2$ as function of $h\nu$ of ITO films.......... 78
5.4 (a-d). FESEM surface morphology of the *SP335-SP338* (50-200 °C) ITO films 78
5.5 (a-d). AFM morphology of ITO films.......... 79
6.1 a) Real ($< \varepsilon_1 >$) and b) Imaginary ($< \varepsilon_2 >$) part of pseudo dielectric function measured as a function of photon energy for *nip1* to *nip4* solar cells along with c-Si substrate. In case of c-Si, the spectra are normalized by a factor of two to fit in the range.......... 86
6.2 Schematic four-layer model for a) TL and b) BEMA model.......... 86
6.3 Measured and fitted (TL model) values of real ($< \varepsilon_1 >$) and imaginary ($< \varepsilon_2 >$) part of pseudo dielectric function as a function of photon energy, (a)-(d) *nip1-nip4* solar cells.......... 87
6.4 TL model parameters (A, E_0, C and E_g) of a-Si:H(i) layer of *nip1-nip4* cells as a function of estimated thickness of a-Si:H(i) layer.......... 88
6.5 Measured and fitted values of real ($< \varepsilon_1 >$) and imaginary ($< \varepsilon_2 >$) part of pseudo dielectric function as a function of photon energy, (a)-(d) *nip1-nip4* solar cells (fitted with BEMA model).......... 89
6.6 The volume fraction of a-Si:H a) intrinsic and b) p layers of *nip1-nip4* cells...... 90

TH-2097_126121019

6.7 (a, b). The volume fraction of interface (i_1, i_2) layers of *nip1-nip4* cells………… 90
6.8 (a-d). Real ($< \varepsilon_1 >$) and Imaginary ($< \varepsilon_2 >$) part of pseudo dielectric function measured as a function of photon energy for 35 and 50 nm thick a-Si:H(i) films before and after 2 min HPT…………………………………………………… 92
6.9 Schematics model for TL and BEMA fitting……………………………………… 92
6.10 (a-d): Measured and fitted (TL model) values of $< \varepsilon_1 >$ and $< \varepsilon_2 >$ as a function of photon energy for 35 and 50 nm thick a-Si:H(i) films before and after 2 min HPT……………………………………………………………... 93
6.11 (a-d): Measured and fitted (BEMA model) values of $< \varepsilon_1 >$ and $< \varepsilon_2 >$ a function of photon energy for 35 and 50nm thick a-Si:H(i) films before and after 2 min HPT……………………………………………………………... 94
6.12 FESEM image of i) c-Si(n) substrate a) before and b) after 10 min H_2 plasma; ii) a-Si:H(i) films (35nm thick) on c-Si c) before and d) after 2 minutes H_2 plasma treatment……………………………………………………………….. 95
6.13 AFM image of i) c-Si(n) substrate a) before and b) after 10 min H_2 plasma; ii) a-Si:H(i) films (35nm thick) on c-Si c) before and d) after 2 minutes H_2 plasma treatment……………………………………………………………….. 96
6.14 Dark *J-V* characteristics of *nip0*, *nip2, nip3* and *nip4* cells (open symbols represent reverse bias, whereas filled symbols represent forward bias)………… 97
6.15 *J-V* characteristics of c-Si/a-Si:H heterojunction solar cells…………………….. 98
6.16 The maximum of $< \varepsilon_2 >$ spectra, fill factor and efficiency of *nip1-nip4* cells….. 99
6.17 EQE spectra of c-Si/a-Si:H heterojunction solar cells…………………………… 100
7.1 Dark *J-V* characteristics of cells under reverse and forward bias condition……... 107
7.2 *J-V* characteristics of *Ag/Al/c-Si(n)/a-Si:H(i)/a-Si:H(p)/ITO/Ag* heterojunction solar cells………………………………………………………………… 108
7.3 EQE spectra of c-Si/a-Si:H heterojunction solar cells…………………………… 110
7.4 (a-f). EQE spectra of c-Si/a-Si:H heterojunction solar cells with and without reverse biasing………………………………………………………… 111

TH-2097_126121019

List of Tables

1.1 Reported results of c-Si/a-Si:H heterojunction solar cells on n-type c-Si wafers by few research groups... 5

2.1 Different absorption peak positions and corresponding vibrational modes for a-Si:H thin films.. 26

3.1 Crystalline (X_c), nano crystalline (X_{nc}), grain boundary (X_{gb}) fractions and bond angle deviations (I_{TA}/I_{TO} and $\Delta\theta$) calculated from Raman. Hydrogen content (C_H) and microstructure (R^*) factor calculated from FTIR measurements 41

3.2 Thickness (d), band gap (E_g) and refractive index (n) of the films calculated from using UV-Vis-NIR and SE measurements.. 47

3.3 Model fitted parameters (A, E_0, C and E_g) of *HP_0* to *HP_3* films............... 48

3.4 Thickness, void, amorphous and crystalline fraction of bulk and surface roughness layer of *HP_0* to *HP_3* films calculated from SE and RMS roughness from AFM measurements... 48

4.1 TL model fitted parameters (A, E_0, C and E_g) and estimated thickness of a-Si:H(p) films.. 62

4.2 The estimated void (f_v), amorphous (f_a) and crystalline (f_c) volume fractions, thickness and surface roughness (d_s) of a-Si:H(p) films................................ 63

4.3 TL model fitted parameters (A, E_0, C and E_g) and estimated thickness of a-Si:H(n) films.. 67

4.4 The estimated void (f_v), amorphous (f_a) and crystalline (f_c) volume fractions, thickness and surface roughness (d_s) of a-Si:H(n) films................................ 68

5.1 Calculated crystallite size (d_{XRD}) and micro strain (ϵ) in the films.................. 77

5.2 Estimated thickness, optical bandgap (E_g), surface roughness (d_{RMS}), resistivity (ρ) and sheet resistance (R_{sheet}) of films.. 79

6.1 TL model fitted parameters (A, E_0, C and E_g) and estimated thickness of different layers of *nip1-nip4* solar cells.. 87

6.2 Thickness (d_{layer}), void (f_v), amorphous (f_a) and crystalline f_c fraction of layers of cells calculated from SE measurements... 91

6.3 TL model fitted parameters (A, E_0, C and E_g) and estimated thickness of interface

TH-2097_126121019

	and a-Si:H(i) layers…………………………………………………….	93
6.4	Thickness, void, amorphous and crystalline fraction of interface and a-Si:H(i) layers calculated from BEMA model……………………………………………	94
6.5	The estimated solar cell parameters for *nip1-nip4* c-Si/a-Si:H heterojunction solar cells……………………………………………………………………………..	99
7.1	Deposition conditions for c-Si/a-Si:H heterojunction solar cells…………………	106
7.2	The solar cell parameters of c-Si/a-Si:H heterojunction solar cells………………	108

TH-2097_126121019

Chapter 1

Introduction

Solar energy will be the main energy source in future due to drastic changes in geographical and environmental conditions. The solar renewable energy is best alternate among all other renewable energy sources. A solar cell is a solid state electrical device (p-n junction) that converts the energy of light directly into electricity using photovoltaic effect. The photovoltaic effect was reported by Edmund Bequerel in 1839 [1]. The principle of solar cell is (i) creation of electron–hole pairs, that is generation of free charge carriers through the absorption of photons in the material, (ii) separation and (iii) collection of the free charge carriers (free electrons and holes) in order to produce electricity.

Photovoltaic (PV) technology is classified into two categories mainly wafer based and thin film solar cells. In the wafer based solar cells, crystalline silicon wafers are used for fabrication of solar cells. Thin film solar cells divided into Cadmium Telluride (CdTe), Copper Indium Gallium Selenide (CIGS) and thin film silicon solar cells. Other new technologies like Dye sensitized solar cell (DSSC), Organic photovoltaic (OPV) and Perovskite solar cells are being developed. The main drawback of these new technologies are material instability, difficulties in fabrication of solar cells in large area and processing of different layers. Limited availability of material and toxicity are main issues in CdTe and CIGS solar cells. The silicon based solar cells have tremendous advantages over other PV technologies due to stability, durability, abundance, low fabrication temperature and large area with high efficiency.

Fig.1.1 shows the reported world best efficiencies of solar cells with different materials and technology by various research groups. Many research groups are focused on increasing the efficiency of different type of solar cells and decreasing the cost, time and utilization of raw material.

TH-2097_126121019

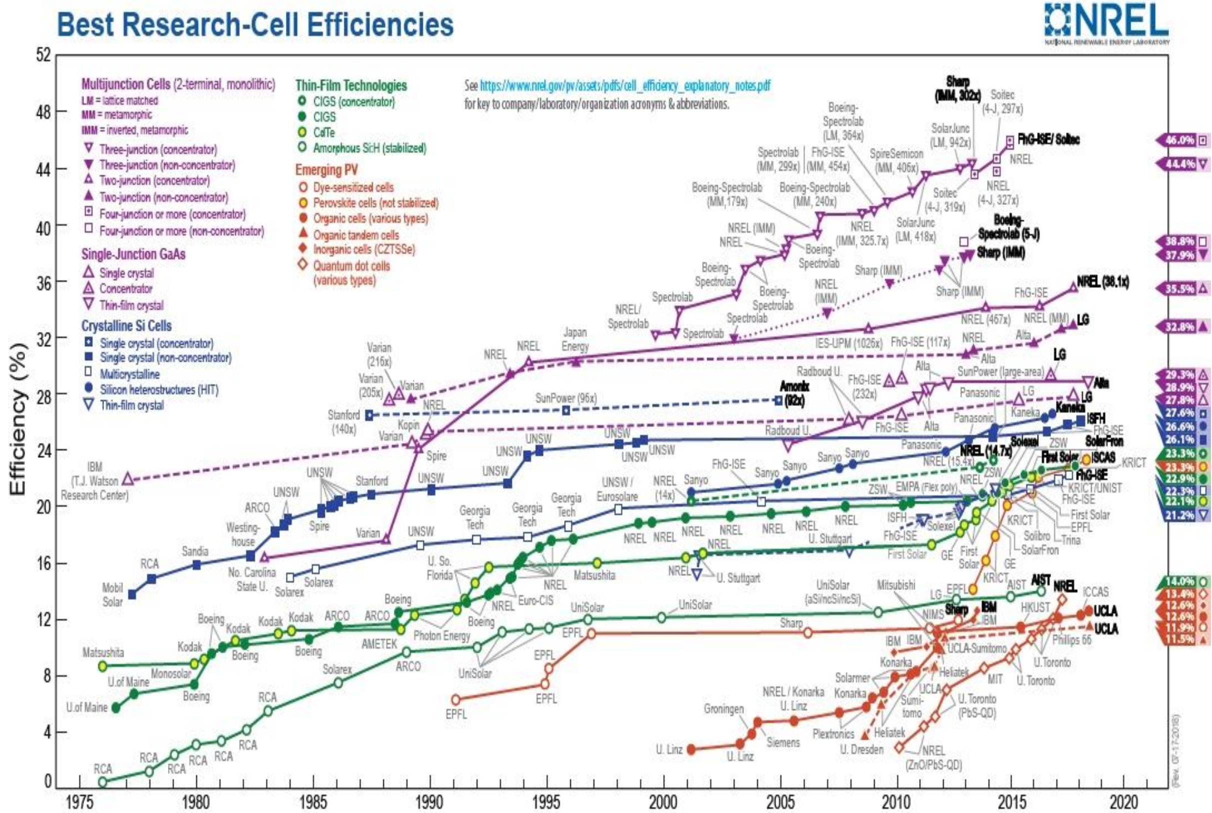

Fig.1.1. Best solar cell efficiency with different materials and technology by different groups [2].

Fig. 1.2 shows the annual production of PV power by different regions in the last eight years. The global annual PV production is dominated by China with 68% share of market in 2017 and PV technology and production in India is growing steadily in recent years [3].

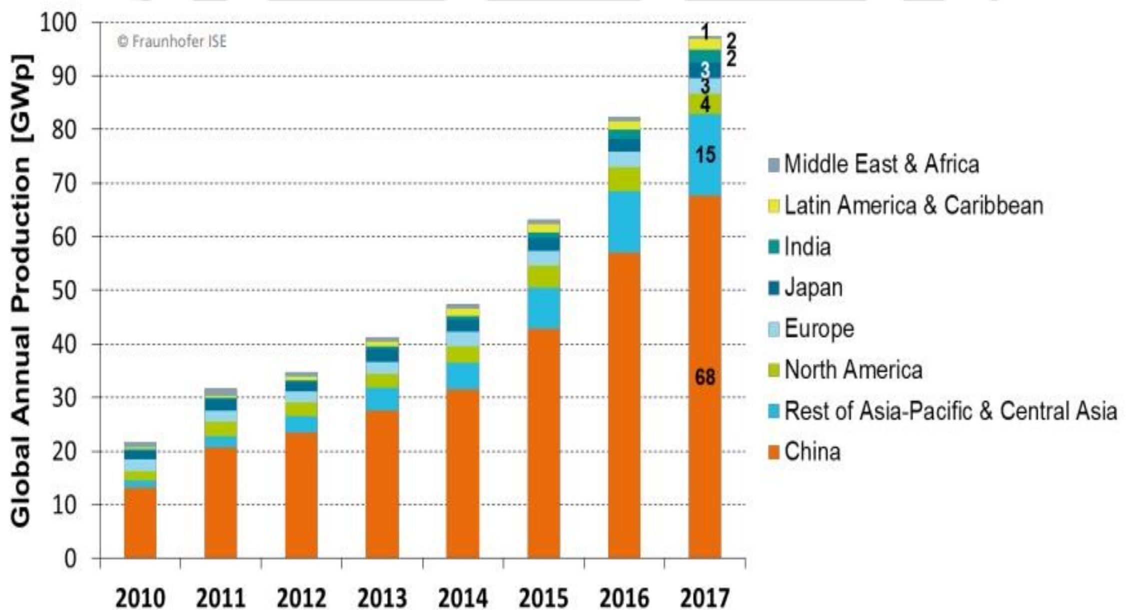

Fig. 1.2. PV industry global annual production by different region in recent years [3].

TH-2097_126121019

1.1. Silicon photovoltaic technology

Silicon based solar cells are mainly divided into two categories: crystalline silicon (c-Si) and thin film silicon based solar cells. The c-Si solar cells are further divided into different categories according to crystallinity and crystal size resulting in single crystalline wafers, multi-crystalline wafers, ribbons based solar cells. Thin film silicon solar cells are divided into two categories based on different active absorber material, which are hydrogenated amorphous silicon (a-Si:H), hydrogenated microcrystalline silicon (μc-Si:H) and their alloys. The first reported c-Si solar cell fabricated by Bell laboratory in 1954 achieved a conversion efficiency of 6% [4,5]. Since then there is a steady increase in efficiency, current highest efficiency is 26% [6–8]. The crystalline silicon (c-Si) photovoltaic (PV) technology is dominating the market with a share of 95% in the present days and it is likely to continue in forthcoming years also due to its durability, stability, abundance, environment friendly and higher efficiency, whereas, other thin film technology is about 5% of market share [3] and in this 5%, a-Si:H thin film based solar cells accounted 0.3% [3] due to higher defect density, instability of material [9] and low conversion efficiency of solar cells [7].

1.2. c-Si/a-Si:H heterojunction solar cells

Heterojunction is a semiconductor junction formed by two different band gap material, whereas two same band gap materials form homojunction [10]. In heterojunction, electrons from n-type material diffuse towards the junction due to gradient in their concentration, leaving behind positively charged donors and resulting in upward band bending on n-side. This results in built in potential barrier at conduction band. Similarly, holes from p-type material diffuse towards the junction and leaving behind negatively charged acceptors, this leads to downward band bending and built in potential at valence band. Injection of the electrons from the n-type (absorber) into the p-type semiconductor can be minimized by choosing p-type material with a larger bandgap than that of the n-type, which form the band offset at the conduction band. Due to this band discontinuity, heterojunction allows only electrons to n-type and holes to p-type material for transportation and avoids recombination losses [11,12]. This results in a more efficient use of photo generated carriers and consequently a higher photocurrent from the cell [13]. Fig. 1.3 show the schematic band bending of single side and double side c-Si(n)/a-Si:H(p) heterojunction solar cells [13].

TH-2097_126121019

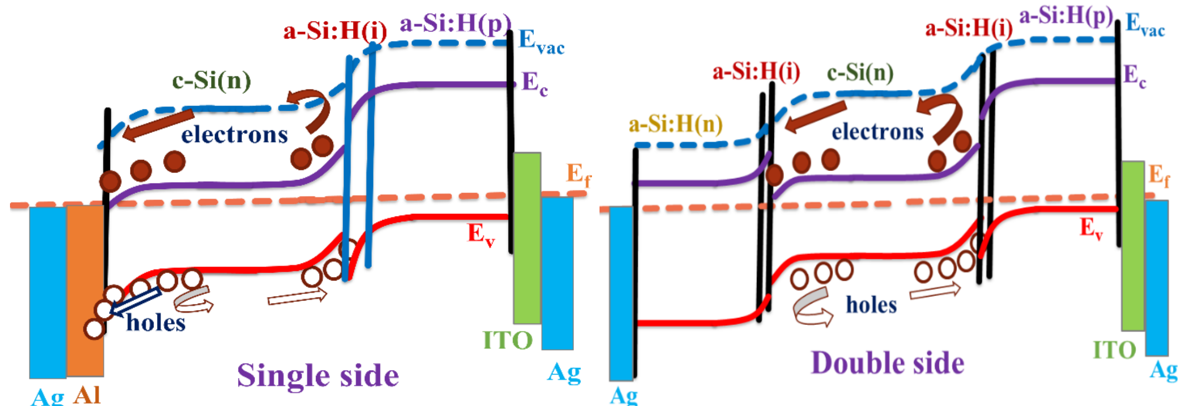

Fig. 1.3. Schematic band bending diagram of single side and double side c-Si(n)/a-Si:H(p) heterojunction solar cells [13].

The c-Si/ a-Si:H heterojunction solar cells offer an attractive alternative to pure c-Si solar cells. These c-Si/a-Si:H heterojunction solar cells can be easily fabricated at temperature below 200ºC, whereas, junction formation in conventional c-Si solar cells is usually done by a thermal diffusion step, for which temperature of 800-1000 ºC is needed [6]. This low temperature processing enables the use of thinner wafers and reduction of thermal budget during the heterojunction formation. Wafer bowing is suppressed due to the low processing temperature of the heterojunction silicon solar cells and its symmetric structure [14]. The time required to form the heterojunction and deposit contact layers is also shorter for heterojunctions than for conventional c-Si solar cells. The silicon heterojunction (SHJ) solar cells exhibit smaller drop in performance with increasing temperature in comparison with conventional c-Si solar cells [15]. In SHJ solar cells, improved surface passivation and reduced recombination losses resulting in higher open circuit voltage values can be observed as compared to c-Si solar cells. The conversion efficiency of c-Si/a-Si:H heterojunction solar cells is comparable with c-Si solar cells [6,16,17].

In 1974, Fuhs et.al reported first a-Si/c-Si heterojunction [18] and later in 1983, Okuda et.al reported first a-Si/poly c-Si heterojunction solar cell with efficiency of 12% [19]. In 1992, researchers at Sanyo have developed new technology of c-Si/a-Si:H heterojunction solar cells and achieved high efficiency of 18.1% [20]. In this PV technology, the heterojunction with intrinsic thin layer (HIT) SHJ solar cells are fabricated by inserting a very thin layer of a-Si:H(i) between c-Si wafer and doped emitter layer, where a-Si:H(i) layer is mainly used for surface passivation of c-Si [20]. The configuration is registered as HIT by Sanyo in 1992. The a-Si:H(i) layer can supress surface defects and recombination sites at interface between c-Si wafer and doped a-Si:H layers. After Sanyo’s record efficiency with breakthrough technology in Si

TH-2097_126121019

photovoltaics, many research groups are attracted towards c-Si/a-Si:H heterojunction solar cells [15,21]. In 2014, The Sanyo has reported highest efficiency of 25.6% [16] and open circuit voltage of 750 mV on n-type c-Si substrates with double side HIT solar cell structure [22]. This HIT technology scheme has been applied to passivated rear and emitter contact (PERC) Si [23,24], tunnel oxide passivated contact (TOPCon) Si [25], point contact Si and interdigitated back contact (IBC) Si solar cells etc [24,26–28]. The highest reported efficiency is 26.7% on n-type [29,30] and 26.1% on p-type c-Si wafer with interdigitated back contact silicon heterojunction (IBC-SHJ) solar cell technology [8]. However, it is very challenging to achieve such high performance solar cells due to lack of quality Si wafers and sophisticated techniques and many complicated process steps and contamination problems. In order to reduce wafer cost of solar cells, thinner and multi crystalline wafer have been used for fabrication of solar cells. The efficiency of multi crystalline Si solar cells is low compared to pure c-Si as well as c-Si/a-Si:H heterojunction solar cells and reported highest efficiency is 22% [21]. Currently many research groups are working on c-Si/a-Si:H heterojunctions solar cells to improve the performance by addressing many issues which are responsible for deterioration of the performance of the cells [2,7]. Here, a few results of c-Si/a-Si:H heterojunction solar cell on n-type Si wafer by different research groups are given in Table 1.1.

Table 1.1. Reported results of c-Si/a-Si:H heterojunction solar cells on n-type c-Si wafers by few research groups.

	Research group	η (%)	V_{oc} (mV)	J_{sc} (mA/cm^2)	FF	Area(cm^2) (description)	Year	Ref.
1	Kaneka, Japan	26.6	738	42.6	0.85	180 (IBC-SHJ)	2018	[29]
2	FhG-ISE, Germany	25.8	724	42.8	0.83	4 (Top/Rear contact)	2017	[31]
3	Sanyo, Japan	25.6	740	41.8	0.83	143 (HIT(SHJ))	2014	[16]
4	FhG-ISE, Germany	24.0	714	42.4	0.81	100 (TOPCon)	2017	[25]
5	Sanyo , Japan	24.7	750	39.5	0.83	100 (HIT(SHJ))	2014	[22]
6	Kaneka, Japan	22.1	729	38.5	0.79	220 (SHJ)	2011	[32]
7	RRS, Switzerland	21.8	726	37.7	0.77	4 (SHJ)	2011	[33]
8	EPFL, Switzerland	21.8	726	37.8	0.78	4 (SHJ)	2011	[34]
9	SERIS, Singapore	21.1	702	38.3	0.78	(SHJ)	2012	[35]
10	CEA-INES, France	20.5	711	40.1	0.72	105 (Back contact)	2016	[36]
11	HZB, Germany	20.6	710	38.1	0.76	100 (SHJ)	2014	[37]
12	IEC, USA	18.3	694	35.7	0.74	0.55 (SHJ)	2010	[38]
13	LG, Korea	18.2	687	33.3	0.78	1 (SHJ)	2010	[39]
14	AIST, Japan	17.5	656	35.6	0.75	0.2 (SHJ)	2009	[40]

1.3. Limiting issues for the c-Si/a-Si:H heterojunction solar cells

The performance of the c-Si/a-Si:H heterojunction solar cells depends on many parameters such as substrate cleaning, recombination and optical losses, interface defects, series and shunt

TH-2097_126121019

resistances, quality of a-Si:H and TCO layers and metal contacts. In order to improve the performance of the solar cells, following issues need to be addressed.

(i) Surface cleaning and passivation is one of the main challenges to reduce the surface recombination losses.

(ii) In silicon heterojunction solar cells, the thickness of i- and p/n-layer is typically 5-10 nm. However, it is very challenging to deposit very thin (5-10 nm) a-Si:H films with device quality.

(iii) The a-Si:H(p) and a-Si:H(n) layers require sufficiently high doping to form required internal electric field and also good interface properties between intrinsic and doped-layers as well as doped and indium tin oxide (ITO)(TCO) layers.

(iv) Formation of abrupt hetero junctions with less interface defect density to be addressed to reduce recombination states at the interface. Interface layers are very crucial for c-Si/a-Si:H heterojuncton solar cells to reduce recombination losses and improve transport properties.

(v) Optimization of transparent conducting oxide (TCO) layer and metal contacts is important to reduce resistance and optical losses.

(vi) Achieving high efficiency of c-Si/a-Si:H heterojunction solar cells is still a challenge due to complicate processing steps and contamination issues. Efficiency of solar cells can be improved by different processing methods.

(vii) In order to reduce material cost, achieving high efficiency with multicrystalline and thinner wafers is one of the main challenges.

1.4. Motivation, objectives and content of the thesis

Our main motivation has been the fabrication and characterization of high open circuit voltage and high efficiency c-Si/a-Si:H heterojunction solar cells by different processing methods and techniques. Our main focus has been to achieve the high efficiency and open circuit voltage with single side c-Si/a-Si:H heterojunction solar cells. As most of the research groups are focused on double side SHJ solar cells to improve the performance of the devices, less attention is paid to the single side solar cells [41–46]. Single side SHJ solar cells significantly reduces cost, processing steps and fabrication time compared to double side SHJ solar cells. These cells also have potential to achieve high efficiency and high open circuit voltage by interface and surface passivation processes. Typical structure of single side c-Si/a-Si:H heterojunction solar cells in this thesis work is shown in Fig. 1.3.

TH-2097_126121019

Several deposition techniques have been developed to prepare amorphous silicon films and its alloys such as Pulsed laser deposition (PLD) [45], Remote plasma chemical vapor deposition (RPCVD) [46], Very high frequency PECVD (VHFPECVD) [40], Hot wire CVD (HWCVD) [49] and Radio frequency PECVD (RFPECVD) [50]. Among all, RFPECVD is the most promising and widely used for the preparation of amorphous silicon films as well as solar cells. The scientific community has adapted a standard RF frequency of 13.56 MHz for this technique which is also used for industrial applications [51-55]. The advantage of this technique is that high quality films are deposited uniformly over a large area at low substrate temperature.

Many characterization techniques are available to study the microstructural properties of a-Si:H films and interface properties of solar cells such as Transmission electron microscopy (TEM), Raman spectroscopy, Spectroscopic ellipsometry (SE) and Fourier transform infrared spectroscopy (FTIR) techniques. Among all, SE is very useful for characterization of a-Si:H films and interface of solar cells [47–56]. The phase transition from amorphous to nc/ μc-Si:H phase in different stages of film deposition can be studied qualitatively with in-situ and ex-situ technique [53–55]. It is possible to determine the optical constants, band gap, thickness, amorphous, crystalline and void fraction, thickness of rough surface layer of single and multi-layer structures like solar cells through the analysis of dielectric function using suitable models simultaneously [47,57–60]. However, it is very important to choose suitable model and ensure that best fitting to obtain precise and valid results.

We have chosen a few objectives with above mentioned motivation, which are i) optimization of both intrinsic and doped a-Si:H films and ITO thin films by different processes, ii) fabrication of c-Si/a-Si:H heterojunction solar cells and iii) improve the performance of the solar cells by surface, interface passivation and varying thickness and doping of a-Si:H layers with improved microstructure. With these objectives, we have achieved high open circuit voltage of 711 mV and efficiency of 17.3% for single side c-Si/a-Si:H heterojunction solar cells with optimized a-Si:H and ITO layers.

The present thesis contains 8 chapters. Chapter 1 presents the brief introduction of silicon PV technology and fabrication and characterization of c-Si/a-Si:H heterojunction solar cells and its advantages over c-Si solar cells including literature review. The motivation and objective of the thesis work are also included in this chapter.

Chapter 2 presents a brief description of deposition process of a-Si:H thin films by RFPECVD technique, which is also used for fabrication of c-Si/a-Si:H heterojunction solar cells. This

TH-2097_126121019

chapter also contain brief discussion of different characterization techniques that are used to the study the structural, optical, electrical and morphological properties of a-Si:H and ITO thin films and also evaluate the performance of c-Si/a-Si:H heterojunction solar cells.

Chapter 3 presents the influence of hydrogen plasma treatment on the growth of nano crystalline silicon phase in a-Si:H films. In order to improve the microstructure, optical and electrical properties of the a-Si:H films, hydrogen plasma was introduced during growth of the a-Si:H films in number of steps. The evolution of nanocrystalline Si phase due to intermittent hydrogen plasma treatment is studied through Ex-Situ SE, Raman, TEM and FTIR absorption spectroscopy. It is observed that exposure to hydrogen plasma during deposition of a-Si:H films improves the microstructure of the films by etching the amorphous phase and replacing the weak Si-Si bonds and Si-H_2 bonds by strong Si-H bonds. The overall deposition rate of these nc-Si films is higher than that obtained by hydrogen dilution of silane for similar films.

Chapter 4 presents influence of hydrogen flow rate on the microstructure and optical properties of boron and phosphorous doped hydrogenated amorphous silicon (a-Si:H(p) and a-Si:H(n)) films. A series of a-Si:H(p) and a-Si:H(n) films were deposited using RFPECVD technique by varying the hydrogen flow rate in the range of 30-70 SCCM and 30-80 SCCM respectively. The SE measurements have been performed on these films to study microstructure, thickness, optical bandgap, void, amorphous and crystalline volume fractions and also surface roughness. It is observed that microstructure of a-Si:H(p) and a-Si:H(n) films changes from amorphous to nano crystalline phase by increasing hydrogen flow rate during film growth.

Chapter 5 presents the influence of deposition temperature on microstructure, morphology, optical and electrical properties of Indium tin oxide (ITO) thin films. In order to optimize the deposition parameters to get high quality transparent conducting oxide (TCO), ITO thin films were deposited on Corning1737 glass substrate at deposition temperature ranging from 50 to 200 °C by using RF Sputtering technique. Structural, optical and electrical properties of ITO films were studied by XRD, UV-Vis-NIR and *I-V* measurements. Morphology of ITO films was studied by AFM and FESEM techniques. It is observed that the films deposited at 50°C were nanocrystalline in nature. The film crystallinity was enhanced with increases in deposition temperature and saturated at 150 °C. It is found that the films deposited at 150 °C have high transmission of 90-98% in the wavelength range of 400-1500 nm, low sheet resistance of 7.5 Ω/□ and surface roughness of 6.1 nm.

TH-2097_126121019

Chapter 6 presents the influence of a-Si:H(i) thickness on the performance of the c-Si/a-Si:H heterojunction solar cells. One sided c-Si/a-Si:H heterojunction solar cells (*Ag/Al/c-Si(n)/a-Si:H(i)/a-Si:H(p)/ITO/Ag*) were fabricated on double side polished n- type c-Si wafer by RFPECVD technique in multi-chamber system. The cells were fabricated with hydrogen plasma treatment of a-Si:H(i) layer of different thicknesses prior to the deposition of top a-Si:H(p) layer. The thickness, optical band gap and microstructure of different a-Si:H layers in the cells were estimated using Spectroscopic ellipsometry. This chapter also presents influence of H_2 plasma treatment on the open circuit voltage (V_{oc}), short circuit current density (J_{sc}) and fill factor (FF) of solar cells. Spectral response of the solar cells was measured by external quantum efficiency (EQE) technique. The hydrogen plasma treatment has passivated and improved the n/i, i/p interfaces and a-Si:H layers without deteriorating the electronic quality of layers. We have obtained high open circuit voltage of 711 mV for these single side c-Si/a-Si:H solar cells.

Chapter 7 presents the influence of boron doping concentration and thickness of a-Si:H(p) layer on the performance of the c-Si/a-Si:H heterojunction solar cells. One sided c-Si/a-Si:H heterojunction solar cells (*Ag/Al/c-Si(n)/a-Si:H(i)/a-Si:H(p)/ITO/Ag*) were fabricated by tuning the thickness and doping of a-Si:H(p) layer by RFPECVD technique. The open circuit voltage (V_{oc}), short circuit density (J_{sc}), fill factor (FF) and efficiency (η) of solar cells were estimated by *I-V* measurements. EQE measurements were carried out on the cells with and without external reverse bias to study interface properties and significance of electric field at interface. We have achieved high open circuit voltage of 705 mV and efficiency of 17.3% for these single side c-Si/a-Si:H heterojunction solar cells.

Chapter 8 presents summary and highlights of studies on a-Si:H thin films and c-Si/a-Si:H heterojunction solar cells. The future scope of this research area is also included.

1.5. References

[1] A. E. Becquerel, Recherches sur les effets de la radiation chimique de la lumiere solaire au moyen des courants electriques, Comptes Rendus L'Academie Des Sci. 9 (1839) 145–149. doi:10.1016/S0733-8619(05)70210-3.

[2] NREL, NREL Efficiency Chart. https://www.nrel.gov/pv/assets/pdfs/pv-efficiencies-07-17-2018.pdf (accessed Sep 20, 2018), 2018. doi:10.1159/000293602.

[3] Fraunhofer Institute for Solar Energy Systems, Photovoltaics Report, 27 August 2018, 2018. doi:20.10.2016.

TH-2097_126121019

[4] P. Chappin, Fuller, Bell labs demonstrate the first practical silicon solar cell, April 25, 1954, This Mon. Phys. Hist. APS Phys. 18 (2009) 10–12.

[5] M.A. Green, Silicon photovoltaic modules: A brief history of the first 50 years, Prog. Photovoltaics Res. Appl. 13 (2005) 447–455. doi:10.1002/pip.612.

[6] J. Zhao, A. Wang, M.A. Green, High-efficiency PERL and PERT silicon solar cells on FZ and MCZ substrates, Sol. Energy Mater. Sol. Cells. 65 (2001) 429–435. doi:10.1016/S0927-0248(00)00123-9.

[7] M.A. Green, Y. Hishikawa, E.D. Dunlop, D.H. Levi, J. Hohl-Ebinger, A.W.Y. Ho-Baillie, Solar cell efficiency tables (version 52), Prog. Photovoltaics Res. Appl. 26 (2018) 427–436. doi:10.1002/pip.3040.

[8] F. Haase, C. Hollemann, S. Schäfer, A. Merkle, M. Rienäcker, J. Krügener, R. Brendel, R. Peibst, Laser contact openings for local poly-Si-metal contacts enabling 26.1%-efficient POLO-IBC solar cells, Sol. Energy Mater. Sol. Cells. 186 (2018) 184–193. doi:10.1016/j.solmat.2018.06.020.

[9] R.A.Street, Hydrogenated amorphous silicon, Cambridge Solid State Ser. (1991). doi:10.1017/CBO9780511525247,ISBN:9780521371568.

[10] S.M. Sze, Semiconductor Devices Physics and Technology, 3rd Edition, Willey. (2017). doi:10.1007/978-3-319-63154-7.

[11] T.F. Schulze, L. Korte, F. Ruske, B. Rech, Band lineup in amorphous/crystalline silicon heterojunctions and the impact of hydrogen microstructure and topological disorder, Phys. Rev. B. 83 (2011) 1–11. doi:10.1103/PhysRevB.83.165314.

[12] L. Korte, E. Conrad, H. Angermann, R. Stangl, M. Schmidt, Advances in a-Si:H/c-Si heterojunction solar cell fabrication and characterization, Sol. Energy Mater. Sol. Cells. 93 (2009) 905–910. doi:10.1016/j.solmat.2008.10.020.

[13] L.K. Wilfried G.J. H.M.van Sark, Physics and technology of amorphous-crystalline heterojunction silicon solar cells, Springer. (2012).

[14] Y. Tsunomura, Y. Yoshimine, M. Taguchi, T. Baba, T. Kinoshita, H. Kanno, H. Sakata, E. Maruyama, M. Tanaka, Twenty-two percent efficiency HIT solar cell, Sol. Energy Mater. Sol. Cells. 93 (2009) 670–673. doi:10.1016/j.solmat.2008.02.037.

[15] S. De Wolf, A. Descoeudres, Z.C. Holman, C. Ballif, High-efficiency Silicon Heterojunction Solar Cells: A Review, Green. 2 (2012) 7–24. doi:10.1515/green-2011-0018.

[16] K. Masuko, M. Shigematsu, T. Hashiguchi, D. Fujishima, M. Kai, N. Yoshimura, T. Yamaguchi, Y. Ichihashi, T. Mishima, N. Matsubara, T. Yamanishi, T. Takahama, M. Taguchi, E. Maruyama, S. Okamoto, Achievement of More Than 25% Conversion Efficiency With Crystalline Silicon Heterojunction Solar Cell, IEEE J. Photovoltaics. 4

TH-2097_126121019

(2014) 1433–1435. doi:10.1109/JPHOTOV.2014.2352151.

[17] M.A. Green, Y. Hishikawa, A.W.Y.H. Baillie, E.D. Dunlop, D.H. Levi, Solar cell efficiency tables (version 51), Prog. Photovoltaics Res. Appl. 26 (2018) 3–12. doi:10.1002/pip.2978.

[18] W. Fuhs, K. Niemann, J. Stuke, Heterojunctions of Amorphous Silicon and Silicon Single Crystals, AIP Conf. Proc. 20 (1974) 345–350. doi:10.1063/1.2945985.

[19] Koiji Okudu, Hiroaki Okamoto, Yoshihoro Hamakawa, Amorphous Si Polycrystalline Si Stacked Solar Cell Having More Than 12% Conversion Efficiency, Jpn. J. Appl. Phys. 9 (1983) 605–607.

[20] M. Tanaka, M. Taguchi, T. Matsuyama, T. Sawada, S. Tsuda, S. Nakano, H. Hanafusa, Y. Kuwano, Development of New a-Si/C-Si Heterojunction Solar Cells: ACJ-HIT (Artificially Constructed Junction-Heterojunction With Intrinsic Thin-Layer), Japanese J. Appl. Phys. Part 1-Regular Pap. Short Notes Rev. Pap. 31 (1992) 3518–3522. doi:10.1143/JJAP.31.3518.

[21] J. Benick, R. Müller, F. Schindler, A. Richter, H. Hauser, F. Feldmann, P. Krenckel, S. Riepe, M. C. Schubert, M. Hermle, S. W. Glunz, Approaching 22% efficiency with multicrystalline n-type silicon solar cells, in: PV Sol. Energy Cnference Exhib., 2017: pp. 1188–1197. doi:10.1111/j.1469-7610.2010.02280.x.

[22] M. Taguchi, A. Yano, S. Tohoda, K. Matsuyama, Y. Nakamura, T. Nishiwaki, K. Fujita, E. Maruyama, 24.7% Record efficiency HIT solar cell on thin silicon wafer, IEEE J. Photovoltaics. 4 (2014) 96–99. doi:10.1109/JPHOTOV.2013.2282737.

[23] Emmanual van kerschaver, Back-contact solar cells a review, Prog. Photovoltaics Res. Appl. 14 (2006) 107–123.

[24] Y. Ohshita, T. Kamioka, K. Nakamura, Technology Trends of High Efficiency Crystalline Silicon Solar Cells, AAPPS Bull. 27 (2017) 1–8. doi:10.22661/AAPPSBL.2017.27.3.02.

[25] F. Feldmann, M. Bivour, C. Reichel, M. Hermle, S.W. Glunz, Passivated rear contacts for high-efficiency n-type Si solar cells providing high interface passivation quality and excellent transport characteristics, Sol. Energy Mater. Sol. Cells. 120 (2014) 270–274. doi:10.1016/j.solmat.2013.09.017.

[26] R.V.K. Chavali, S. De Wolf, M.A. Alam, Device physics underlying silicon heterojunction and passivating-contact solar cells: A topical review, Prog. Photovoltaics Res. Appl. 26 (2018) 241–260. doi:10.1002/pip.2959.

[27] M.K. Mat Desa, S. Sapeai, A.W. Azhari, K. Sopian, M.Y. Sulaiman, N. Amin, S.H. Zaidi, Silicon back contact solar cell configuration: A pathway towards higher efficiency, Renew. Sustain. Energy Rev. 60 (2016) 1516–1532. doi:10.1016/j.rser.2016.03.004.

TH-2097_126121019

[28] R. Baxter, N. Hastings, A. Law, E.J.. Glass, Simplified IBC solar cells, Anim. Genet. 39 (2008) 561–563.

[29] K. Yoshikawa, W. Yoshida, T. Irie, H. Kawasaki, K. Konishi, H. Ishibashi, T. Asatani, D. Adachi, M. Kanematsu, H. Uzu, K. Yamamoto, Exceeding conversion efficiency of 26% by heterojunction interdigitated back contact solar cell with thin film Si technology, Sol. Energy Mater. Sol. Cells. 173 (2017) 37–42. doi:10.1016/j.solmat.2017.06.024.

[30] K. Yoshikawa, H. Kawasaki, W. Yoshida, T. Irie, K. Konishi, K. Nakano, T. Uto, D. Adachi, M. Kanematsu, H. Uzu, K. Yamamoto, Silicon heterojunction solar cell with interdigitated back contacts for a photoconversion efficiency over 26%, Nat. Energy. 2 (2017) 17032. doi:10.1038/nenergy.2017.32.

[31] A. Richter, J. Benick, F. Feldmann, A. Fell, M. Hermle, S.W. Glunz, n-Type Si solar cells with passivating electron contact : Identifying sources for efficiency limitations by wafer thickness and resistivity variation, Sol. Energy Mater. Sol. Cells. 173 (2017) 96–105. doi:10.1016/j.solmat.2017.05.042.

[32] K. Yamamoto, D. Adachi, H. Uzu, M. Ichikawa, T. Terashita, High-ef fi ciency heterojunction crystalline Si solar cell and optical splitting structure fabricated by applying thin- fi lm Si technology, Jpn. J. Appl. Phys. 15 (2015) 08KD151-08KD155.

[33] J. Meixenberger, P. Papet, B. Rau, B. Strahm, G. Wahli, F. Wünsch, Characterisation of over 21% efficient silicon heterojunction cells developed at Roth and Rau Switzerland, 26th Eur. Photovolt. Sol. Energy Conf. Exhib. 26 (2000) 1073–1075.

[34] C. Ballif, L. Barraud, A. Descoeudres, Z.C. Holman, S. Morel, S. De Wolf, a-Si:H/c-Si heterojunctions : A future mainstream technology for high - efficiency crystalline silicon solar cells, IEEE J. Photovoltaics. 1 (2011) 1705–1709.

[35] T. Mueller, J. Wong, A.G. Aberle, Heterojunction Silicon Wafer Solar Cells using Amorphous Silicon Suboxides for Interface Passivation, Energy Procedia. 15 (2012) 97–106. doi:10.1016/j.egypro.2012.02.012.

[36] J.R. D. Muñoz, T. Desrues, A. S. Ozanne, N. Nguyen, S. de Vecchi, F. Souche, S.Martin de Nicolàs, C. Denis, Key aspects on development of high efficiency heterojunction and IBC heterojunction solar cells:Towards 22% efficiency on industrial size, Proc. 26th Eur. Photovolt. Sol. Energy Conf. Exhib. 26 (2011) 861–864.

[37] M. Mews, E. Conrad, S. Kirner, N. Mingirulli, L. Korte, Hydrogen plasma treatments of amorphous/crystalline silicon Heterojunctions, Energy Procedia. 55 (2014) 827–833. doi:10.1016/j.egypro.2014.08.066.

[38] R.. Das, U.K, Burrows, M.Z, Lu, M, Bowden, S, Birkmire, Surface passivation and heterojunction cells on Si (100) and (111) wafers using dc and rf plasma deposited Si : H thin films, Appl. Phys. Lett. 92 (2018) 063504. doi:10.1063/1.2857465.

[39] K. S. Ji, J. Choi, W. S. Choi, H. M. Lee, D. Kim, K. S. Ji, J. Choi, W. S. Choi, H. M.

TH-2097_126121019

Lee, D. Kim, surface passivation properties of boron and phosphorous doped a-Si:H films with multi step deposition for Si heterojunction solar cells, 35th IEEE Photovolt. Spec. Conf. (2010) 3190.

[40] H. Fujiwara, H. Sai, M. Kondo, Crystalline Si Heterojunction Solar Cells with the Double Heterostructure of Hydrogenated Amorphous Silicon Oxide, Jpn. J. Appl. Phys. 48 (2009) 064506. doi:10.1143/JJAP.48.064506.

[41] H. Fujiwara, M. Kondo, Effects of a-Si:H layer thicknesses on the performance of a-Si:H/c-Si heterojunction solar cells, J. Appl. Phys. 101 (2007) 054516. doi:10.1063/1.2559975.

[42] H. Fujiwara, M. Kondo, Impact of epitaxial growth at the heterointerface of a-Si:H/c-Si solar cells, Appl. Phys. Lett. 90 (2007) 2005–2008. doi:10.1063/1.2426900.

[43] H. Fujiwara, T. Kaneko, M. Kondo, Optimization of interface structures in crystalline silicon heterojunction solar cells, Sol. Energy Mater. Sol. Cells. 93 (2009) 725–728. doi:10.1016/j.solmat.2008.09.007.

[44] W.K. Oh, S.Q. Hussain, Y.J. Lee, Y. Lee, S. Ahn, J. Yi, Study on the ITO work function and hole injection barrier at the interface of ITO/a-Si:H(p) in amorphous/crystalline silicon heterojunction solar cells, Mater. Res. Bull. 47 (2012) 3032–3035. doi:10.1016/j.materresbull.2012.04.106.

[45] T.H. Wang, M.R. Page, E. Iwaniczko, Q. Wang, Y. Xu, Y. Yan, L. Roybal, D. Levi, R. Bauer, H.M. Branz, 17.5% p-Type Silicon Heterojunction Solar Cells with HWCVD a-Si : H as the Emitter and Back Contact, in: NREL/CP-520-38942, 2005: pp. 1–5. doi:https://digital.library.unt.edu/ark:/67531/metadc892630/m1/3/.

[46] T.H. Wang, E. Iwaniczko, M.R. Page, Q. Wang, Y. Xu, Y. Yan, D. Levi, L. Roybal, R. Bauer, H.M. Branz, High-Efficiency Silicon Heterojunction Solar Cells by HWCVD, in: IEEE 4th World Conf., 2006: pp. 1439–1442. doi:10.1109/WCPEC.2006.279723.

[47] A. Fontcuberta i Morral and P. Roca i Cabarrocas, C.Clerc, Structure and hydrogen content of polymorphous silicon thin films studied by spectroscopic ellipsometry and nuclear measurements, Phys. Rev. B. 69 (2004) 125307. doi:10.1103/PhysRevB.69.125307.

[48] T. Yuguchi, Y. Kanie, N. Matsuki, H. Fujiwara, Complete parameterization of the dielectric function of microcrystalline silicon fabricated by plasma-enhanced chemical vapor deposition, J. Appl. Phys. 111 (2012) 083509. doi:10.1063/1.4704158.

[49] H. Zhang, X. Zhang, G. Hou, C. Wei, J. Sun, X. Geng, S. Xiong, Y. Zhao, The microstructure and optical properties of p-type microcrystalline silicon thin films characterized by ex-situ spectroscopic ellipsometry, Thin Solid Films. 521 (2012) 17–21. doi:10.1016/j.tsf.2012.03.081.

[50] T.D. Kang, H. Lee, S.J. Park, J. Jang, S. Lee, Microcrystalline silicon thin films studied

TH-2097_126121019

using spectroscopic ellipsometry, J. Appl. Phys. 92 (2002) 2467–2474. doi:10.1063/1.1499980.

[51] D. Das, K. Bhattacharya, Characterization of the Si:H network during transformation from amorphous to micro- and nanocrystalline structures, J. Appl. Phys. 100 (2006) 103701. doi:10.1063/1.2384812.

[52] H. Fujiwara, M. Kondo, A. Matsuda, Real-time spectroscopic ellipsometry studies of the nucleation and grain growth processes in microcrystalline silicon thin films, Phys. Rev. B. 63 (2001) 115306. doi:10.1103/PhysRevB.63.115306.

[53] S. Logothetidis. Kiriakidis. C. Paloura, Modifications in a-Si:H during thermal annealing: In situ spectroscopic ellipsometry, J. Appl. Phys. 70 (1991) 2791. doi:10.1063/1.349341.

[54] J.K. Saha, B. Bahardoust, K. Leong, A.B. Gougam, N.P. Kherani, S. Zukotynski, Spectroscopic ellipsometry studies on hydrogenated amorphous silicon thin films deposited using DC saddle field plasma enhanced chemical vapor deposition system, Thin Solid Films. 519 (2011) 2863–2866. doi:10.1016/j.tsf.2010.12.074.

[55] R.W. Collins, A.S. Ferlauto, G.M. Ferreira, C. Chen, J. Koh, R.J. Koval, Y. Lee, J.M. Pearce, C.R. Wronski, Evolution of microstructure and phase in amorphous, protocrystalline, and microcrystalline silicon studied by real time spectroscopic ellipsometry, Sol. Energy Mater. Sol. Cells. 78 (2003) 143–180. doi:10.1016/S0927-0248(02)00436-1.

[56] Ilsin An, H. V. Nguyen, N. V. Nguyen, R. W.Collins, Microstructural evolution of ultrathin amorphous silicon films by real-time spectroscopic ellipsometry, Phys. Rev. Lett. 65 (1990) 2274–2277. doi:10.1103/PhysRevLett.65.2274.

[57] G.E.Jellison and F.A. Modine, Parameterization of the optical functions of amorphous materials in the interband region, Appl. Phys. Lett. 69 (1996) 371–373. doi:10.1063/1.118064.

[58] A.S. Ferlauto, G.M. Ferreira, J.M. Pearce, C.R. Wronski, C.D. Ganguly, Analytical model for the optical functions of amorphous semiconductors from the near- infrared to ultraviolet : Applications in thin film photovoltaics, J. Appl. Phys. 92 (2002) 2424. doi:10.1063/1.1497462.

[59] Y. Liu, G. Xu, C. Song, W. Weng, P. Du, G. Han, Modification on Forouhi and Bloomer model for the optical properties of amorphous silicon thin films, Thin Solid Films. 515 (2007) 3910–3913. doi:10.1016/j.tsf.2006.11.003.

[60] H. Fujiwara, Spectroscopic Ellipsometry Principles and Applications, Willey Publ. (2007). doi:10.1002/9780470060193,ISBN:9780470016084.

TH-2097_126121019

Chapter 2

Experimental Techniques

This chapter presents the brief discussion on fabrication and characterization techniques for a-Si:H thin films and c-Si/a-Si:H heterojunction solar cells. In this thesis work, a-Si:H films were deposited by radio frequency plasma enhanced chemical vapour deposition (RFPECVD) technique. For structural evaluation of a-Si:H films, Raman spectroscopy and Transmission electron microscopy (TEM) measurements have been carried out and for optical properties, UV-Vis-NIR and Fourier transform infrared spectroscopy (FTIR) measurements were done. Ex-situ Spectroscopic ellipsometry (SE) technique was used to study microstructural and optical properties of the films and also interface properties of solar cells. Electrical properties of a-Si:H thin films were studied by current-voltage measurements. Surface morphology of the films was studied by Atomic force microscope (AFM) and Field emission scanning electron microscope (FESEM) technique. The performance of c-Si/a-Si:H heterojunction solar cells was evaluated by current-voltage and external quantum efficiency measurements.

2.1. Preparation of thin films and solar cells

Hydrogenated amorphous silicon (a-Si:H) thin films were deposited on corning 1737 glass and undoped crystalline silicon (c-Si) substrates using radio frequency plasma enhanced chemical vapour deposition (RFPECVD) technique. Indium tin oxide (ITO) thin films were deposited by RF sputtering technique. Brief discussion on these techniques are given below.

2.1.1. Radio frequency plasma enhanced chemical vapour deposition technique

Radio frequency plasma enhanced chemical vapour deposition (RFPECVD) technique is most commonly used in industry to fabricate a-Si:H thin film based solar cells and also silicon heterojunction (SHJ) solar cells. In the capacitively coupled glow discharge technique, plasma is maintained between two parallel plates at an excitation frequency of 13.56 MHz applied by RF power source. One electrode is connected to RF power source and substrate holder is mounted on other electrode, which is grounded. The plasma is generated after gas mixture of SiH_4 and H_2 enters into the deposition chamber and sustained by the oscillating electric field

TH-2097_126121019

between the two parallel plates. In this discharge process, free electrons gain sufficient kinetic energy by the electric field in order to dissociate the gas molecules into free radicals, atoms and molecules, both positive and negative ions, and electrons. Subsequently, the formed radicals, ions and molecules undergo secondary reactions, which have a substantial effect on the electronic and structural properties of the deposited layers[1]. The electrons are easily moved to the electrodes and form sheath (i.e electric field between center of the plasma and substrate) near the grounded electrode. In these regions, positive ions are attracted towards the electrodes, causing ion bombardment. On the substrate, surface reactions and release of hydrogen molecules as well as the relaxation of the silicon matrix finally take place [1,2].

The multi-chamber CVD system used for films and solar cell fabrication consist of three RF PECVD and one hot wire CVD (HWCVD) with load lock facility and is shown in Fig. 2.1. In this system, intrinsic, boron and phosphorous doped a-Si:H layers are deposited in different RF PECVD chambers in order to prevent from contamination. The rf electrode area of RFPECVD system is 45.58 cm^2 and electrode separation is 4 cm. These PECVD and HWCVD systems are individually connected to turbo molecular pump (Pfeiffer, HIPAC 300) backed by rotary pump to create high vacuum (~10^{-7} mbar) in the chamber. The exhaust of each pumps is connected to burn box and soap water tank, where the unutilized gases are completely burnt out and decomposed.

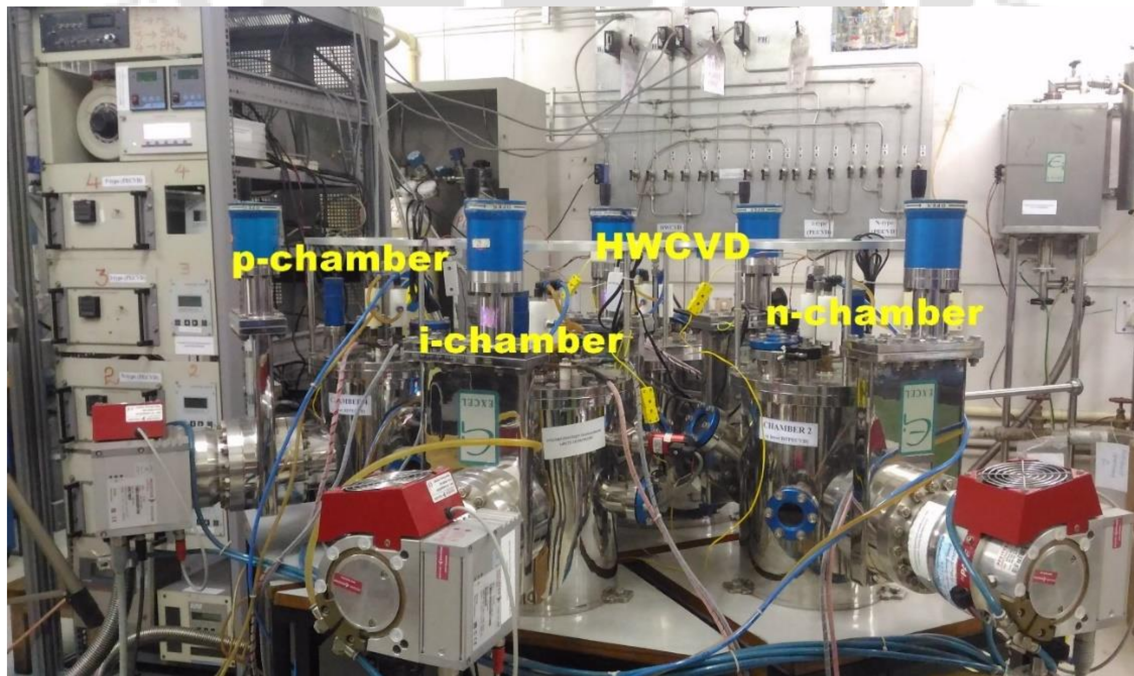

Fig. 2.1. Multi chamber RFPECVD and HWCVD system.

TH-2097_126121019

2.1.1.1. Growth mechanism of a-Si:H thin films

Fig. 2.2 show the schematic diagram and main possible chemical reactions of growth mechanism of a-Si:H films. During the deposition of a-Si:H films, a number of reactive species like SiH_3, SiH_2, SiH, Si, H_2 and H are produced which experience secondary reactions, mostly with parent SiH_4 molecule, forming a steady state. Each secondary reaction has a different rate constant [3,4]. Highly reactive species like SiH_2, SiH and Si have much less density in the plasma compared to SiH_3 and thus SiH_3 is the main film forming precursor on the substrate [4]. The SiH_3 radicals reaching the substrate start to diffuse on the surface. The growing films have a large density of defects like dangling bonds and weakly bonded Si-H_2 bonds along with strong Si-Si and Si-H bonds [4].

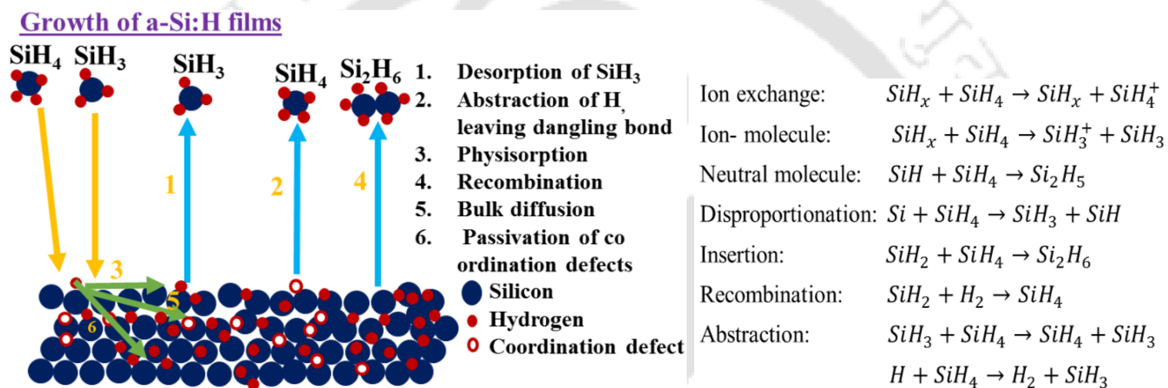

Fig. 2.2. Schematic diagram and possible reactions of growth mechanism of a-Si:H films [4].

SiH_3 is main precursor for deposition of a-Si:H films. It has sticking coefficient of 0.1 and these precursors experience many reactions during film growth, such as desorption of SiH_3 radicals, recombination with another SiH_3 radical and abstraction of hydrogen atom [5,6]. This SiH_3 radical abstracts one hydrogen atom and produces a SiH_4 molecule and leaves surface dangling bond, which interacts with next SiH_3 radical. This leads to growth of a-Si:H films.

2.1.2. RF sputtering technique

Sputtering is one of the physical vapour deposition (PVD) techniques used for deposition of thin films under plasma conditions. Sputtering is basically the physical ejection of atoms from a solid source target due to energetic gas ions bombardment. High vacuum (~10^{-6}-10^{-7} mbar) is created inside chamber prior to the deposition process. Controlled flow of an inert gas, usually Argon (Ar) gas is introduced into the deposition chamber. Further, high voltage is applied between cathode and anode, where target and substrate act as cathode and anode respectively. This high voltage creates excited Ar^+ ions and leads to acceleration toward the

TH-2097_126121019

negatively biased target. Then energetic Ar^+ ions strike the target surface and eject the target atoms. Sputtered atoms are moved onto the substrate and form a thin film [2]. Due to energetic ion bombardment of target, secondary electrons are also ejected. Strong magnetic field is used to trap secondary electrons to the target. This magnetic field confine the plasma close to the target. The sputtered atoms are not affected by the magnetic field due to charge neutrality [2,7]. The area of the rf electrode was 20.25 cm^2. DC power supply is used for pure metals and RF power supply is used for semiconductors and insulators.

2.1.3. Fabrication of solar cells

The c-Si/a-Si:H heterojunction solar cells were fabricated by RF-PECVD in multichamber system. The n-type crystalline silicon wafers (resistivity 5-10 Ωcm, thickness 275-325 µm, double side polished, CZ) have been used for cell fabrication. Many solar cells have been deposited with active area of 0.2 cm^2 on 1x1 $inch^2$ and 2x2 $inch^2$ size wafers.

2.1.3.1. Crystalline silicon cleaning process

Radio Corporation of America (RCA) laboratory has developed cleaning procedure for crystalline silicon wafers. We have followed standard RCA-1 and RCA-2 cleaning process for c-Si cleaning for fabrication of solar cells. The cleaning procedure steps are:

RCA-1 cleaning

RCA-1 cleaning is used for removal of organic and insoluble contaminants. For this process, RCA solution consists of mixture of H_2O: H_2O_2: NH_4OH in the range of 5:1:1 to 7:2:1[8,9].

1. The mixture of 200 ml of deionised (DI) water and 40 ml of NH_4OH (27%) in Pyrex beaker was heated on hot plate around 80 ^oC for 5-10 min for increased activation of the reaction.
2. Beaker with solution was removed from hot plate and 40 ml of H_2O_2 (30%) was added. After 1-2 min, bubbles started coming rigorously from solution. This indicated that solution is ready for use.
3. The c-Si wafer was soaked in this solution for 15 min.
4. The c-Si wafer was removed from the solution and rinsed in DI water for several times (5-6 times).
5. Finally, c-Si wafer was dipped in HF for 1 min to remove native oxide.

TH-2097_126121019

RCA-2 cleaning

This RCA-2 is used to remove the ionic and heavy metal atomic contaminants. For this process, RCA solution consists of mixture of H_2O: H_2O_2: HCl in the range of 6:1:1 to 8:2:1 [8,9].

1. The mixture of 180 ml of deionised (DI) water and 30 ml of HCl (27%) in Pyrex beaker was heated on hot plate around 80 ºC for 5-10 min for activated reaction.
2. Beaker with solution was removed from hot plate and 30 ml of H_2O_2 (30%) was added. After 1-2 min, bubbles started coming rigorously from solution. This indicated that solution is ready for use.
3. The c-Si wafer was soaked in this solution for 15 min.
4. The c-Si wafer was removed from the solution and rinsed in DI water for several times (5-6 times).
5. Finally, c-Si wafer was dipped in HF for 1 min to remove formed oxide layer during cleaning process.

RCA-1 and RCA-2 cleaning process were carried out in fume hood for safety purpose. After cleaning, the wafers were dried with nitrogen gas and then immediately loaded in deposition chamber.

After RCA cleaning of Si wafer, aluminium (Al) was deposited by thermal evaporation on rear surface of wafer. The wafer was subsequently loaded in RFPECVD system and annealed at 400 ºC at 10^{-6} to 10^{-7} mbar pressure for 1 hr to ensure the diffusion of Al in Si for good back contact. The top surface of Si wafer was subjected to 10 min H_2 plasma to clean the surface and passivate the dangling bonds and then a-Si:H(i) layer of varying thickness was deposited. The Si wafers were shifted to a-Si:H(p) layer deposition chamber, where the a-Si:H(i) layer was subjected to 2 min HPT prior to the deposition of top a-Si:H(p) layer. After the deposition of a-Si:H(i) (i-layer) and a-Si:H(p) (p-layer) layer, Indium tin oxide (ITO) on top of the a-Si:H(p) and silver (Ag) layer on back side were deposited by rf sputtering. Finally, front Ag metal bus bars and fingers grid electrodes were made on cell with silver paste.

2.2. Characterization techniques

2.2.1. Raman scattering spectroscopy

Raman spectroscopy is widely used to study the microstructure and bonding modes in a-Si:H thin films. Raman spectroscopy is an optical and non-destructive technique based on the

TH-2097_126121019

inelastic scattering phenomenon of light. Raman studies reported in this thesis work were performed using HORIBA Jobin-Yvon LabRam HR Raman spectroscopy equipped with Ar-ion laser at a wavelength of 514 nm and at room temperature in the backscattering geometry. The spot size of the laser beam was 1 μm in diameter and the incident laser power on the sample was less than 1 mW. In Raman spectra of a-Si:H films, most intense peak at 480 cm^{-1} corresponds to the transverse optic (TO) mode, whereas peaks at 410 cm^{-1}, 310 cm^{-1} and 150 cm^{-1} correspond to longitudinal optic (LO) mode, longitudinal acoustic (LA) mode and transverse acoustic (TA) mode respectively [10,11]. In case of c-Si, the TO peak is observed at 520 cm^{-1}, whereas for nc-Si, the TO peak is shifted from 520 cm^{-1} to lower wave number side depending upon the size of the crystallites [12]. Another peak observed around 490-500 cm^{-1} corresponds to the grain boundaries due to the presence of nano-crystallites in amorphous matrix [13]. The TO phonon mode is sensitive to the root mean square tetrahedral bond angle deviation ($\Delta\theta$) which reflects short range order (SRO) in amorphous network. Beaman et.al have obtained linear relation between the full width at half maxima (FWHM) of TO peak (Γ_{TO}) and $\Delta\theta$, which is used to determine $\Delta\theta$ from Raman measurements (Eq.2.1) [10].

$$\Gamma_{TO} = 15 + 6\Delta\theta \qquad \text{------------- (2.1)}$$

The TA mode is related to the density of dihedral angle fluctuations ($\Delta\phi$), reflecting the medium range order (MRO) of amorphous network. The intensity ratio (I_{TA}/I_{TO}) of the peaks corresponding to TA to TO mode of a-Si:H is used to estimate the MRO in the films [14]. A lower value of ratio reflects the improved MRO in the films.

The crystalline volume fraction (X_c) is given as the ratio between the sum of the integrated intensities of grain boundary and nanocrystalline Si peaks to the sum of integrated intensities of amorphous, grain boundary and nanocrystalline Si peaks (Eq. 2.2).

$$X_c = \frac{I_{gb}+I_{nc}}{I_a+I_{gb}+I_{nc}} \qquad \text{------------- (2.2)}$$

Where I_a, I_{gb} and I_{nc} are the integrated intensities of amorphous, grain boundary and nanocrystalline TO peaks respectively.

The nanocrystalline volume fraction (X_{nc}) and grain boundary volume fraction (X_{gb}) in the films are calculated using Eq. 2.3 and 2.4 respectively.

$$X_{nc} = \frac{I_{nc}}{I_a+I_{gb}+I_{nc}} \qquad \text{------------- (2.3)}$$

TH-2097_126121019

$$X_{gb} = \frac{I_{gb}}{I_a+I_{gb}+I_{nc}}$$ ------------- (2.4)

The mean crystallite size (d_{Raman}) is calculated using Eq. 2.5.

$$d_{Raman} = 2\pi\sqrt{\frac{B}{\Delta\omega}}$$ ------------- (2.5)

Where $\Delta\omega$ is the shift in the peak position from c-Si peak position (520 cm^{-1}) and B=2.0 cm^{-1} nm^2.

2.2.2 Transmission electron microscopy technique

Transmission electron microscopy (TEM) measurements were carried out to evaluate the structure of the films. TEM, selective area electron diffraction (SAED) pattern and high resolution TEM (HRTEM) images were recorded using JEOL-2100. TEM was used to determine the structure and crystallinity of the thin films in dark field mode with a 200 kV acceleration voltage and LaB_6 filament. The a-Si:H and nc-Si:H thin films were scratched out and sonicated in acetone for a few minutes and dispersed on copper (Cu) mesh grid for measurement. The HRTEM image has been used to estimate lattice spacing (d-spacing) of different crystallographic planes of the nc-Si:H thin films [2].

2.2.3. Spectroscopic ellipsometry

Spectroscopic ellipsometry (SE) is a highly accurate, non-destructive and optical technique to investigate the optical, structural properties, and to estimate the thickness, band gap, refractive index and surface roughness of the thin films. The main feature of SE is that it measures the change in polarization state of light upon reflection from the sample. The unpolarised light released from xenon light source passes through polariser and is polarised linearly. The linearly polarised light incidents on the sample and some of light get reflected from sample surface and some fraction of light go inside film and is reflected from interfaces. The reflected light from surface and interfaces has information of films. The phase and amplitude of resultant reflected light changes and it is elliptically polarised. This elliptically polarised light go to detector to record response[15]. Two compensators are used to adjust the phase delay of light. The schematic of SE and spectroscopic ellipsometer instrument (Semilab, Sopra, GES-5E) used for the studies are shown in Fig. 2.3.

TH-2097_126121019

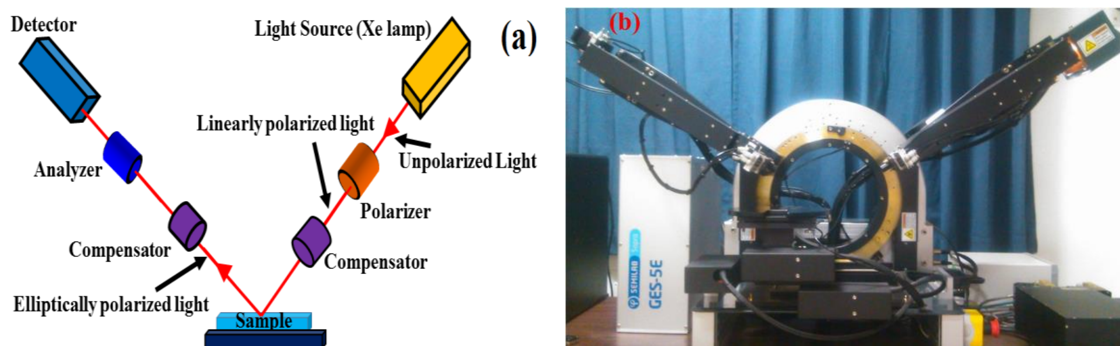

Fig. 2.3. (a). Schematic of SE and (b). Real image of spectroscopic ellipsometer instrument.

SE measures the amplitude ratio (ψ) and phase difference (Δ) of the reflected light oriented in the parallel (p-) and perpendicular (s-) directions with respect to plane of incidence as a function of wavelength or energy [15].

The polarization change (ρ_{SE}) is given by Eq.2.6

$$\rho_{SE} = Tan\psi\, e^{-i\Delta} = {}^{r_p}/_{r_s} \quad \text{------------- (2.6)}$$

Where r_p and r_s are complex Fresnel reflection coefficients of p- and s- polarized light respectively.

The pseudo dielectric function ($<\varepsilon(E)>$) of material is given by Eq.2.7

$$<\varepsilon(E)>= sin^2\theta_0 \left[1 + \left(\frac{1-\rho_{SE}}{1+\rho_{SE}}\right)^2 tan^2\theta_0\right] \quad \text{------------- (2.7)}$$

Where θ_0 is the angle of incidence.

SE is not a direct method to evaluate the optical constant of the materials. The dielectric constants, thickness and optical band gap of the films are deduced from measured (ψ, Δ) values as a function of energy or wavelength applying suitable optical models using single or multilayer structures. Several models like Tauc-Lorentz (TL) [16], Cody-Lorentz (CL) [17], Lorentz, Gauss[15], Forouhi-Bloomer (FB), Modified Forouhi-Bloomer [18,19], Harmonic oscillator[15], Tetrahedral model [20] and Bruggeman effective medium approximation (BEMA) [15] etc. are available for evaluation of a-Si:H films. In this thesis work, both Tauc-Lorentz model, Gauss and BEMA method have been used to estimate the optical constants, thickness and void, amorphous and crystalline volume fractions of the films.

TH-2097_126121019

The complex refractive index of a material is given as $N = n + ik$, where n and k are the refractive index and extinction coefficient respectively. The pseudo dielectric function is given as $\varepsilon(E) = \varepsilon_1(E) + i\varepsilon_2(E)$, where

$$\varepsilon_1(E) = n^2(E) - k^2(E) \text{ and } \varepsilon_2(E) = 2n(E)k(E) \qquad \text{------------- (2.8)}$$

The imaginary part of the pseudo dielectric function $\varepsilon_2(E)$ is thus directly related to absorption of light in the material.

2.2.3.1. Tauc-Lorentz model

The Tauc- Lorentz (TL) dispersion law has been widely used to describe the a-Si:H thin films. This model was developed by Jellison and Modine using the Tauc joint density of states and the Lorentz oscillator model [15,16,21].

An expression for the real part of the dielectric function is obtained by Kramers-Kroning integration and is given by Eq.2.9 [16]

$$\varepsilon_{1,TL}(E) = \varepsilon_1(\infty) + \frac{2}{\pi} P \int_{E_g}^{\infty} \frac{\xi \varepsilon_2(\xi)}{\xi^2 - E^2} d\xi \qquad \text{------------- (2.9)}$$

Where P represents the Cauchy principal part of the integral and $\varepsilon_1(\infty)$ is additional fitting parameter.

The expression for the imaginary part of the dielectric function in Tauc Lorentz model [16] is given (Eq.2.10)

$$\varepsilon_{2,TL}(E) = \begin{cases} \left[\frac{AE_0C(E-E_g)^2}{(E^2-E_0^2)^2+C^2E^2}\frac{1}{E}\right] & \text{for } E > E_g \\ 0 & \text{for } E \leq E_g \end{cases} \qquad \text{------------- (2.10)}$$

Where A is oscillator strength, E_0 is peak transition energy, E_g is optical band gap and C is broadening parameter.

The complete derivation of $\varepsilon_1(E)$ and $\varepsilon_2(E)$ equations is given in Appendix I.

2.2.3.2. Bruggeman effective medium approximation model

The Bruggeman effective medium approximation (BEMA) model is used to calculate void, amorphous and crystalline volume fractions in composite materials and also surface roughness of the films [15,22–24]. When the layer is made up of several mixed phases, each phase having

TH-2097_126121019

its dielectric function $\varepsilon_i(E)$ and volume fraction f_i, the effective dielectric function $\varepsilon_{eff}(E)$ of composite material is given by equation Eq. 2.11 [25].

$$\sum_i f_i \frac{\varepsilon_i(E)-\varepsilon_{eff}(E)}{\varepsilon_i(E)+2\varepsilon_{eff}(E)} = 0 \quad \text{------------- (2.11)}$$

2.2.3.3. Gauss model

The Gauss model is used to fit dielectric function of amorphous silicon films with multiple peaks [15,26]. Multiple transitions in the films are analysed with Gauss model. In this model, the real and imaginary part of dielectric functions of films are given by Eq. 2.12 and Eq. 2.13

$$\varepsilon_1(E) = \frac{2A}{\sqrt{\pi}}\left[D\left(\frac{E+E_0}{\sigma_a}\right) - D\left(\frac{E-E_0}{\sigma_a}\right)\right] \quad \text{------------- (2.12)}$$

$$\varepsilon_2(E) = A\left[exp\left\{-\left(\frac{E-E_0}{\sigma_a}\right)\right\}^2 - exp\left\{-\left(\frac{E+E_0}{\sigma_a}\right)\right\}^2\right] \quad \text{------------- (2.13)}$$

Where A is amplitude of oscillator, E_0 is the oscillator peak position, σ_a is FWHM of the oscillator, D is an operator.

2.2.4. X-Ray diffraction technique

In this thesis, the X-ray diffraction (XRD) system (Rigaku, TTRAX III) is used for determination of structure, crystallite size and micro strain of the ITO thin films [27]. The measurements were done on ITO films deposited on corning1737 glass. The measurements were done in the range of 10-70° of incident angle with Cuk_α wavelength of 0.154 nm with step size of 0.05^o for 2θ at a grazing angle of incidence of 3°. Debye-Scherrer's formula and Williamson-Hall method have been used to estimate crystallite size of ITO thin films.

Debye-Scherrer's formula [28] for crystallite size is given by Eq.2.14

$$d_{XRD} = \frac{k_{XRD}\lambda}{\beta_{hkl}cos\theta_{hkl}} \quad \text{------------- (2.14)}$$

Where, d_{XRD} is crystallite size, λ is wavelength of X-ray radiation, β_{hkl} is full width at half maxima (FWHM) (in Radians), k_{XRD} is proportionality constant (scherrer constant), which is 0.94 for spherical crystals with cubic symmetry and θ_{hkl} is the peak position corresponding to the (hkl) plane.

TH-2097_126121019

Equation of Williamson-Hall (W-H) method [29,30] for determination of crystallite size and micro strain of films is given by Eq.2.15

$$\beta_{hkl}cos\theta_{hkl} = \frac{k_{XRD}\lambda}{d_{XRD}} + 4\epsilon sin\theta_{hkl} \qquad \text{------------- (2.15)}$$

The intercept and slope of linear plot between $\beta_{hkl}cos\theta_{hkl}$ and $sin\theta_{hkl}$ gives the crystallite size (d_{XRD}) and micro strain (ϵ) of the films respectively.

2.2.5 Fourier transform infrared spectroscopy

Fourier transform infrared spectroscopy (FTIR) (Perkin Elmer BX) is a non-destructive technique used to estimate nature of chemical bonding and compositional analysis of material. In this study, FTIR is used to estimate the hydrogen content and microstructure of the a-Si:H films [2,31]. For FTIR measurements, films were deposited on IR transparent substrate such as undoped crystalline Si wafer. The IR spectra was recorded at a step size of 1 cm^{-1} and resolution of 4 cm^{-1} with an average of 64 scans in the range of 400-2300 cm^{-1} for each sample. In order to remove the influence of substrate, background correction was done with bare c-Si substrate. In case of a-Si:H, a peak in absorption spectra at 630-640 cm^{-1} corresponds to the wagging/rocking modes of vibration for Si-H, SiH_2 and SiH_3 bonds. The other prominent absorption peaks corresponding to stretching modes of Si-H and Si-H_2 are present at 2000 and 2100 cm^{-1} respectively. Small peaks corresponding to wagging/twisting modes of Si-H_2 and SiH_3 are present around 820-900 cm^{-1} [32–34]. In FTIR spectra, different absorption peak positions corresponding to different vibrational modes are given in Table 2.1.

The hydrogen concentration (C_H) in the a-Si:H films is calculated from the absorption peak near 640 cm^{-1} using the following Eq. 2.16.

$$C_H = \frac{A_{640}}{N}\int_{\omega 1}^{\omega 2}\frac{\alpha_a(\omega)}{\omega}d\omega \qquad \text{-------------- (2.16)}$$

Where $A_{640} = 2.1\text{x}10^{19}$ cm^{-2} is the oscillator strength and silicon bond density N= $5\text{x}10^{22}$ cm^{-3}, $\alpha_a(\omega)$ is the absorption coefficient [35]. Similarly, the amount of hydrogen bonded as Si-H and Si-H_2 is calculated from the deconvoluted peaks near 2000 and 2100 cm^{-1} using A_{2000} = $9.0\text{x}10^{19}$ cm^{-2} and $A_{2100} = 2.2\text{x}10^{20}$ cm^{-2} respectively [36,37].

The microstructure parameter (R^*) is generally used to determine the quality of a-Si:H thin films. The R^* is defined as the ratio of the integrated intensity of 2100 cm^{-1} peak to sum of integrated intensity of the 2000 and 2100 cm^{-1} peaks (Eq.2.19) [35,38].

TH-2097_126121019

$$R^* = \frac{I_{2100}}{I_{2000}+I_{2100}} \qquad \text{------------- (2.17)}$$

A low value of R^* corresponds to the case when most of the hydrogen is bonded to silicon atoms as mono hydride. The films with low R^* show good optoelectronic quality, low defect density and high stability, whereas high R^* films show poor quality and higher defect density with large void or vacancy fraction [39,40].

Table 2.1: Different absorption peak positions and corresponding vibrational modes for a-Si:H thin films.

Bonding Configuration	Vibrational Mode	Peak Position (cm^{-1})
Si-H	Wagging	640
	Stretching	2000
$Si\text{-}H_2$	Rocking	640
	Twisting	820
	Wagging	850
	Scissor Bending	880
	Stretching	2100
$Si\text{-}H_3$	Wagging	640
	Symmetric Deformation	862
	Degenerate Deformation	907
	Stretching	2140
Si-O-Si	Stretching	980-1080
Si-O-Si-H	Stretching	780
O-Si-Si-O	Stretching	1106
$HSi\text{-}SiO_2$	Stretching	2200
$HSi\text{-}O_3$	Stretching	2260

2.2.6. UV-Vis-NIR spectroscopy

The UV-Vis-NIR spectroscopy has been used to calculate thickness, bandgap and refractive index of thin films. Transmission spectra of the a-Si:H thin films are measured with UV-Vis-NIR spectrometer (Shimadzu 3101PC) in the wavelength range of 200 to 2500 nm. Thickness and refractive index of a-Si:H films calculated using swanepoel's method [41] and optical band gap is obtained from the Tauc's plot [42].

The refractive index of the films is calculated using following relation Eq.2.18

$$n = \left(N + ((N^2 - S^2))^{1/2}\right)^{1/2} \qquad \text{------------- (2.18)}$$

TH-2097_126121019

Where, $N = 2S\left(\frac{T_M - T_m}{T_M T_m}\right) + \frac{S^2+1}{2}$ ------------- (2.19)

Here, S, T_M and T_m are the refractive index of substrate, maximum and minimum of the transmission of the films at a particular wavelength (λ).

Thickness of the films is estimated by given equation Eq.2.20

$$d = \frac{\lambda_1 \lambda_2}{2(\lambda_1 n_2 - \lambda_2 n_1)} \quad \text{------------- (2.20)}$$

Where n_1 and n_2 are the refractive indices at two adjacent maxima or minima corresponding to λ_1 and λ_2 respectively.

The optical band gap (E_g) of the films is estimated using Tauc's relation [42,43] Eq.2.21

$$(\alpha_a h\nu)^m = A_1(h\nu - E_g) \quad \text{------------- (2.21)}$$

Where, $h\nu$ is the incident photon energy, E_g is optical band gap, α_a is absorption coefficient and A_1 is proportionality constant. The value of exponent m is 1/2 for indirect and 2 for direct bandgap transition respectively [44].

2.2.7. Field emission scanning electron microscopy

The field emission scanning electron microscope (FESEM) (ZEISS, SIGMA) measurements were performed on c-Si substrate, a-Si:H and ITO thin films to study the morphology. In this technique, a field emission cathode in electron gun provides high energy narrow and accelerated electron beam focused on the sample and after interaction of high energetic electrons with sample, secondary electrons are generated from sample. These secondary electrons with different energy were collected by detector. FESEM was operated with an accelerating voltage of 2 to 4 KeV and films were coated with a thin gold layer to avoid charging effect during the measurements.

2.2.8. Atomic force microscopy

Atomic force microscope (AFM) (Agilent 5500) was used to study the surface morphology and estimate surface roughness of the films. AFM is a high resolution surface scanning microscopy technique used to obtain information of the morphology of films. The main principle of AFM is, when the cantilever tip is brought close to the film surface, deflection of the cantilever is observed due to the Van der Waals force between film and tip. The deflection is measured by

TH-2097_126121019

a laser spot reflected from the top surface of the cantilever into an array of photodiodes [45]. Cantilever is generally made with silicon or silicon nitride material. AFM measurements were done in non-contact mode on the films deposited on corning glass 1737 and c-Si substrate in scanning area of 10x10, 5x5 and 2x2 μm^2.

2.2.9. Current-Voltage (*I-V*) measurements

2.2.9.1. *I-V* measurements of a-Si:H thin films

The dark and photo conductivity of a-Si:H films were measured using two probe method in coplanar geometry. Conductivity of the films is given by Eq.2.22

$$\sigma = \frac{It}{Vld} \qquad \text{------------- (2.22)}$$

Where, σ is conductivity of the film, d is the thickness of film, V is applied voltage between equal length (l) Ag electrodes, which are separated by distance t and I is the measured current.

A 100 W halogen lamp under AM1.5 conditions was used for photoconductivity measurements. Temperature dependant conductivity measurements were done under high vacuum of 10^{-5}-10^{-6} mbar conditions. For these measurements, temperature was varied from 30 ^{o}C to 200 ^{o}C under vacuum.

The activation energy (E_A) was determined from temperature dependent dark conductivity data using Arrhenius plot [32]. The relation between the dark conductivity (σ_d) and activation energy (E_A) is given by Eq.2.23.

$$\sigma_d = \sigma_0 exp\left(-\frac{E_A}{k_B T}\right) \qquad \text{------------- (2.23)}$$

where σ_d is the dark conductivity σ_0 prefactor, k_B is Boltzmann constant and T is the absolute temperature (in Kelvin).

2.2.9.2. Four probe *I-V* measurement of ITO thin films

The sheet resistance and resistivity of ITO thin films were determined using four probe *I-V* measurements. In this method, four equally spaced finite radius tungsten metal point probes were placed on sample and then further two probes are used to flow a constant current through the sample and inner two probes are used to measure the voltage drop against the resistance.

TH-2097_126121019

The resistivity (ρ) of films is given by equation Eq.2.24

$$\rho = \frac{\pi d}{ln2}\left(\frac{V}{I}\right) \qquad \text{------------- (2.24)}$$

The sheet resistance (R_{sheet}) is determined by following Eq.2.25

$$R_{sheet} = \frac{\rho}{d} = \frac{\pi}{ln2}\left(\frac{V}{I}\right) \qquad \text{------------- (2.25)}$$

2.2.9.3. Current-Voltage (*I-V*) measurements of solar cells

Electrical performance of a solar cell was determined from the current-voltage (*I-V*) measurement. The *I-V* characteristics measurements on c-Si/a-Si:H heterojunction solar cells were done under 100 mW/cm^2 of incident power density from a Xenon lamp with AM1.5 conditions. The Keithley 2450 source and measure unit has been used to apply bias voltage and collect current from solar cell. Fig. 2.4 shows the schematic diagram of *J-V* characteristics of solar cell under dark and illumination conditions.

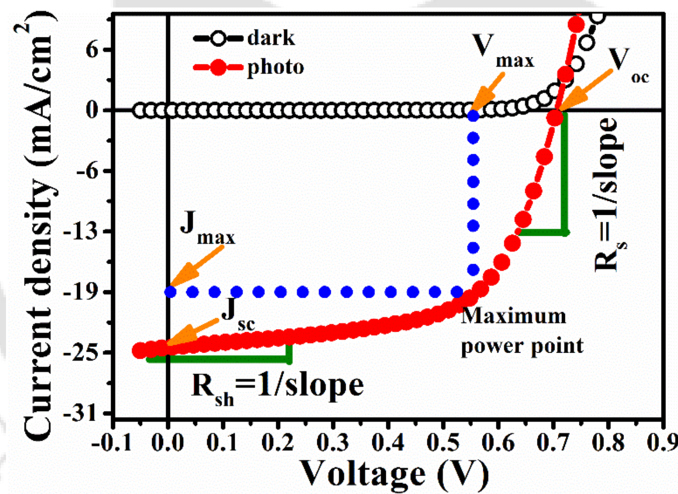

Fig. 2.4. Current density-voltage (*J-V*) characteristics of solar cell under dark and illumination.

The illuminated current density (J_{ill}) of solar cell is given by Eq.2.26 [1]

$$J_{ill} = J_{ph} - J_{dark} \qquad \text{------------- (2.26)}$$

Where J_{ph} is photo current density and J_{dark} is dark current density.

The short circuit current density (J_{sc}) is defined as maximum current through solar cell when the solar cell is short circuited (voltage across the device is zero). This is equal to the total current density through solar cell under illumination in ideal conditions (Eq.2.27).

TH-2097_126121019

$$J_{sc} = J_{ph} \qquad \text{------------- (2.27)}$$

The open circuit voltage (V_{oc}) is defined as maximum potential difference between two terminals of the solar cell when the solar cell is opened (no external current flow) in ideal conditions (Eq.2.28).

$$V_{oc} = \frac{qV}{n_i k_B T} ln\left(\frac{J_{sc}}{J_0} + 1\right) \qquad \text{------------- (2.28)}$$

Fill factor (FF) is measure of squareness of the J-V curve and describes the maximum power utilization of solar cell. The FF is estimated by Eq.2.29

$$FF = \frac{J_{max}V_{max}}{J_{sc}V_{oc}} \qquad \text{------------- (2.29)}$$

The power conversion efficiency (η) is the ratio of maximum output power density to the incident power density [1,46,47]. This is given by Eq.2.30.

$$\eta(\%) = \frac{J_{sc}V_{oc}FF}{P_{in}} \times 100 \qquad \text{------------- (2.30)}$$

Where, J_{max} and V_{max} are short circuit current density and open circuit voltage at maximum power point, FF is fill factor, P_{in} and P_{out} are input and output power density.

The shunt (R_{sh}) and series (R_s) resistance of solar cell were estimated through slope of J-V curve near short circuit and open circuit points respectively using following equations Eq.2.31 and Eq.2.32 [1,46,47].

$$R_{sh} = \frac{1}{\left(\frac{dJ}{dV}\right)_{V=0}} \qquad \text{------------- (2.31)}$$

$$R_s = \frac{1}{\left(\frac{dJ}{dV}\right)_{J=0}} \qquad \text{------------- (2.32)}$$

2.2.10. External quantum efficiency (EQE) measurements

Spectral response and passivation quality of interfaces of solar cells were studied by external quantum efficiency (EQE) measurements with and without external reverse bias conditions. The EQE measurements were carried out in the wavelength range 350-1100 nm on c-Si/a-Si:H heterojunction solar cells. Si photo diode calibrated for global AM1.5 spectra was used as reference to estimate the EQE of the cells [22,48,49]. The EQE measurements were performed at room temperature using an in-house built dual beam set up. Fig. 2.5 shows the schematic

TH-2097_126121019

diagram of the quantum efficiency measurement setup. The Xenon lamp was used as light source for EQE measurements, which is connected through a monochromator (Horiba Jovin Yvon-Triax). The lamp was switched on at least 30 min before any measurements for stable light spectra.

Optical chopper (Stanford Research Systems Model SR540) was used for periodically interrupt the light beam. Incident light beam pass through this optical chopper and with the help of beam spiltter one half of the light beam fall on the solar cell and other half on calibrated photo diode by beam splitter. The optical lenses were installed on the way of light beam from monochromator to optimize the focusing and position of light beam on solar cell as well as reference Si photo diode. The slit width was kept at 3 mm diameter for incident light beam. Second order filters of 400 nm and 610 nm cut off wavelengths were used to block second harmonics of light when the sample was exposed to the light at longer wavelengths. The chopper controller contain a phase locked loop speed control motor to precisely maintain the chopping speed and phase relative to the reference signal. We have used 6 slots blade set and 17 Hz of chopper frequency. The output of optical chopper was connected to two lock-in amplifiers (Stanford Research Systems Model SR-810). One lock-in amplifier was connected to the reference photodiode and another was connected to the solar cell. Lock-in amplifier measures a single output for the component of the signal at a specific reference frequency and reject noise signals corespond to other the frequency and do not affect measurements. The monocromator and lock-in amplifiers were controlled by LabVIEW program through general purpose interface bus (GPIB) card and the output signals were collected from reference diode and solar cell in terms of volts.

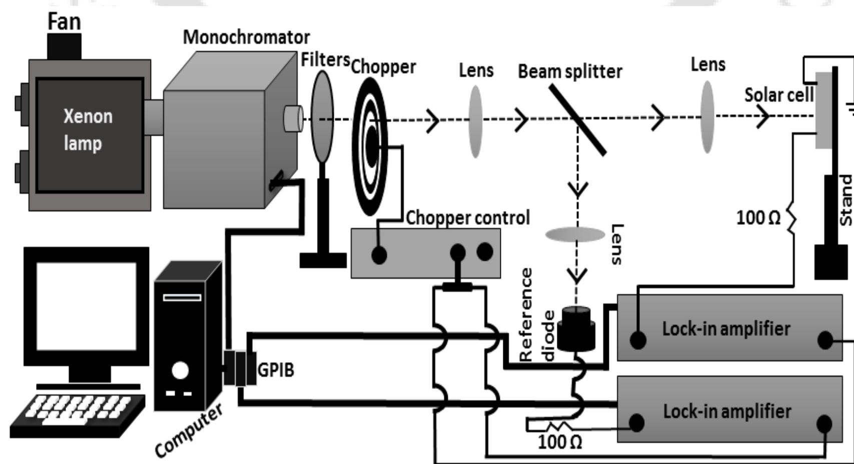

Fig. 2.5. Schematic diagram of quantum efficiency measurement setup.

TH-2097_126121019

The external quantum efficiency (EQE) is defined as ratio of the electrons colleted as photo current to incident photons. The EQE of solar cell is given by Eq.2.33 [1,46,47]

$$EQE(\%) = \frac{hc}{q\lambda} \times SR_{cell} \times 100 \qquad \text{------------- (2.33)}$$

where h, c, q, λ and SR_{cell} are planks constant, velocity of light, charge of electron, wave length of light and spectral response of the measured solar cell respectively.

Spectral response of the measured solar cell is given by the Eq.2.34

$$SR_{cell} = SR_{ref}\left(\frac{V_{cell}}{V_{std}}\right) \times \left(\frac{V_{ref/std}}{V_{ref/cell}}\right) \qquad \text{------------- (2.34)}$$

where SR_{ref}, V_{cell}, V_{std}, $V_{ref/std}$ and $V_{ref/cell}$ are the spectral response of standard reference diode, voltage of the solar cell, voltage of a standard diode, voltage of reference diode when standard diode voltage was measured and voltage of reference diode when solar cell voltage was measured respectively.

The short circuit current density of solar cells estimated from EQE is given by Eq.2.35 [1,46]

$$J_{sc} = \int_{\lambda}^{\lambda+\Delta\lambda} b_s EQE(\lambda) d\lambda \qquad \text{------------- (2.35)}$$

Where b_s is incident spectral photon flux density, λ is wavelength.

2.3. References

[1] A. Shah, Thin film silicon solar cells, EPFL Press. (2010).

[2] Milton Ohring, Materials science of thin films, Acad. Press. (2002).

[3] M.J. Kushner, A model for the discharge kinetics and plasma chemistry during plasma enhanced chemical vapor deposition of amorphous silicon, J. Appl. Phys. 63 (1988) 2532–2551. doi:10.1063/1.340989.

[4] Akihisa Matsuda, Microcrystalline silicon. Growth and application, J. Non. Cryst. Solids. 338–340 (2004) 1–12. doi:10.1016/j.jnoncrysol.2004.02.012.

[5] A. Matsuda, M. Takai, T. Nishimoto, M. Kondo, Control of plasma chemistry for preparing highly stabilized amorphous silicon at high growth rate, Sol. Energy Mater. Sol. Cells. 78 (2003) 3–26. doi:10.1016/S0927-0248(02)00431-2.

[6] Wilfried G.J. H.M.van Sark, Methods of deposition of hydrogenated amorphous silicon for device applications, in: Thin Film. Nanostructures, 2002: pp. 1–215.

TH-2097_126121019

doi:10.1016/S1079-4050(02)80004-7.

[7] K. Seshan, Handbook of Thin-Film Deposition Processes and Techniques - Principles, Methods, Equipment and Applications (2nd Edition), 2002. doi:10.1002/ange.19891010662.

[8] W. Kern , Puotinen D A, Cleaning solutions based on hydrogen peroxide for use in silicon semiconductor technology, RCA Rev. 31 (1970) 187–206.

[9] Werner Kern, The Evolution of Silicon Wafer Cleaning Technology, J. Electrochem. Soc. 137 (1990) 1887–1892. doi:10.1149/1.2086825.

[10] D. Beeman, R. Tsu, M. Thorpe, Structural information from the Raman spectrum of amorphous silicon, Phys. Rev. B. 32 (1985) 874–878. doi:10.1103/PhysRevB.32.874.

[11] M.H. Brodsky, M. Cardona, J.J. Cuomo, Infrared and Raman spectra of the silicon-hydrogen bonds in amorphous silicon prepared by glow discharge and sputtering, Phys. Rev. B. 16 (1977) 3556–3571. doi:10.1103/PhysRevB.16.3556.

[12] Y. He, C. Yin, G. Cheng, L. Wang, X. Liu, G.Y. Hu, The structure and properties of nanosize crystalline silicon films, J. Appl. Phys. 75 (1994) 797–803. doi:10.1063/1.356432.

[13] S. Veprek, F.A. Sarott, Z. Iqbal, Effect of grain boundaries on the Raman spectra, optical absorption, and elastic light scattering in nanometer-sized crystalline silicon, Phys. Rev. B. 36 (1987) 3344–3350. doi:10.1103/PhysRevB.36.3344.

[14] D. Han, J.D. Lorentzen, J. Weinberg-Wolf, L.E. McNeil, Q. Wang, Raman study of thin films of amorphous-to-microcrystalline silicon prepared by hot-wire chemical vapor deposition, J. Appl. Phys. 94 (2003) 2930. doi:10.1063/1.1598298.

[15] H. Fujiwara, Spectroscopic Ellipsometry Principles and Applications, Willey Publ. (2007). doi:10.1002/9780470060193,ISBN:9780470016084.

[16] G.E.Jellison and F.A. Modine, Parameterization of the optical functions of amorphous materials in the interband region, Appl. Phys. Lett. 69 (1996) 371–373. doi:10.1063/1.118064.

[17] A.S. Ferlauto, G.M. Ferreira, J.M. Pearce, C.R. Wronski, C.D. Ganguly, Analytical model for the optical functions of amorphous semiconductors from the near- infrared to ultraviolet : Applications in thin film photovoltaics, J. Appl. Phys. 92 (2002) 2424. doi:10.1063/1.1497462.

[18] A.R. Forouhi, I. Bloomer, Optical dispersion relations for amorphous semiconductors and amorphous dielectrics, Phys. Rev. B. 34 (1986) 7018–7026. doi:10.1103/PhysRevB.34.7018.

[19] Y. Liu, G. Xu, C. Song, W. Weng, P. Du, G. Han, Modification on Forouhi and Bloomer

TH-2097_126121019

model for the optical properties of amorphous silicon thin films, Thin Solid Films. 515 (2007) 3910–3913. doi:10.1016/j.tsf.2006.11.003.

[20] A. Fontcuberta i Morral and P. Roca i Cabarrocas, C.Clerc, Structure and hydrogen content of polymorphous silicon thin films studied by spectroscopic ellipsometry and nuclear measurements, Phys. Rev. B. 69 (2004) 125307. doi:10.1103/PhysRevB.69.125307.

[21] D. Gonçalves, E. Irene, Fundamentals and applications of spectroscopic ellipsometry, Quim. Nova. 25 (2002) 794–800. doi:10.1590/S0100-40422002000500015.

[22] Venkanna Kanneboina, R. Madaka, P. Agarwal, High open circuit voltage c-Si/a-Si:H heterojunction solar cells: Influence of hydrogen plasma treatment studied by spectroscopic ellipsometry, Sol. Energy. 166 (2018) 255–266. doi:10.1016/j.solener.2018.03.068.

[23] Venkanna Kanneboina, R. Madaka, P. Agarwal, Spectroscopic ellipsometry studies on microstructure evolution of a-Si:H to nc-Si:H films by H_2 plasma exposure, Mater. Today Commun. 15 (2018) 18–29. doi:10.1016/j.mtcomm.2018.02.023.

[24] D.E. Aspnes, Optical properties of thin films, Thin Solid Films. 89 (1982) 249–262. doi:10.1016/0040-6090(82)90590-9.

[25] M.L. Rizzoli, C.S. Cicala, P. Capezzuto, G. Bruno, Anatomy of μc -Si thin films by plasma enhanced chemical vapor deposition : An investigation by spectroscopic ellipsometry, J. Appl. Phys. 88 (2000) 2408. doi:10.1063/1.1287129.

[26] D.D.S. Meneses, M. Malki, P. Echegut, Structure and lattice dynamics of binary lead silicate glasses investigated by infrared spectroscopy, J. Non. Cryst. Solids. 352 (2006) 769–776. doi:10.1016/j.jnoncrysol.2006.02.004.

[27] B.D.Cullity, Elements of X-Ray Diffraction, Addison-Wesley Pub. Co. (1956) 1–519.

[28] A.L. Patterson, The scherrer formula for X-ray particle size determination, Phys. Rev. 56 (1939) 978–982. doi:10.1103/PhysRev.56.978.

[29] G.K. Williamson, W.H. Hall, X-ray line broadening from filed aluminium and wolfram, Acta Metall. 1 (1953) 22–31. doi:10.1016/0001-6160(53)90006-6.

[30] G.K. Williamson, W.H. Hall, Discussion of the Theories of Line Broadening, Acta Metall. 1 (1953) 22. doi:10.1016/0001-6160(53)90006-6.

[31] Barbara Stuart, Infrared spectroscopy: Fundamentals and Apllications, Willey. (2010). doi:10.1002/0470011149.

[32] R.A.Street, Hydrogenated amorphous silicon, Cambridge Solid State Ser. (1991). doi:10.1017/CBO9780511525247,ISBN:9780521371568.

[33] Z. Remes , M. Vanecek P. Torres , U. Kroll, A.H. Mahan, R.S. Crandall, Optical

TH-2097_126121019

determination of the mass density of amorphous and microcrystalline silicon layers with different hydrogen contents, J. Non. Cryst. Solids. 227–230 (1998) 876–879. doi:10.1016/S0022-3093(98)00207-5.

[34] U. Kroll, J. Meier, A. Shah, S. Mikhailov, J. Weber, Hydrogen in amorphous and microcrystalline silicon films prepared by hydrogen dilution, J. Appl. Phys. 80 (1996) 4971–4975. doi:doi:10.1063/1.363541.

[35] C. Fang, K. Gruntz, L. Ley, The hydrogen content of a-Ge: H and a-Si: H as determined by IR spectroscopy, gas evolution and nuclear reaction techniques, J. Non. Cryst. Solids. 36 (1980) 255–260. doi:10.1016/0022-3093(80)90603-1.

[36] A.A. Langford, M.L. Fleet, B.P. Nelson, W.A. Lanford, N. Maley, Infrared absorption strength and hydrogen content of hydrogenated amorphous silicon, Phys. Rev. B. 45 (1992) 13367–13377. doi:10.1103/PhysRevB.45.13367.

[37] H. Shaik, G.M. Rao, Critical investigation on hydrogen bonding by Fourier Transform Infrared spectroscopy in hydrogenated amorphous silicon thin films, J. Non. Cryst. Solids. 375 (2013) 88–94. doi:10.1016/j.jnoncrysol.2013.04.062.

[38] M.H. Brodsky, M.A. Frisch, J.F. Ziegler, W.A. Lanford, Quantitative analysis of hydrogen in glow discharge amorphous silicon, Appl. Phys. Lett. 30 (1977) 561–563. doi:10.1063/1.89260.

[39] P. Gogoi, H.S. Jha, P. Agarwal, Effect of Silane flow rate on microstructure of Silicon films deposited by HWCVD, J. Non. Cryst. Solids. 358 (2012) 1990–1994. doi:10.1016/j.jnoncrysol.2011.12.095.

[40] Purabi Gogoi, Pratima Agarwal, Structural and optical studies on hot wire chemical vapour deposited hydrogenated silicon films at low substrate temperature, Sol. Energy Mater. Sol. Cells. 93 (2009) 199–205. doi:10.1016/j.solmat.2008.09.058.

[41] R. Swanepoel, Determination of the thickness and optical constants of amorphous silicon, J. Phys. E. 16 (2000) 1214–1222. doi:10.1088/0022-3735/16/12/023.

[42] J. Tauc, A. Menth, States in the gap, J. Non. Cryst. Solids. 8–10 (1972) 569–585. doi:10.1016/0022-3093(72)90194-9.

[43] J. Tauc, R. Grigorovici, A. Vancu, Optical Properties and Electronic Structure of Amorphous Germanium, Phys. Status Solidi. 15 (1966) 627–637. doi:10.1002/pssb.19660150224.

[44] A.R. Zanatta, I. Chambouleyron, Absorption edge, band tails, and disorder of amorphous semiconductors, Phys. Rev. B. 53 (1996) 3833–3836. doi:10.1103/PhysRevB.53.3833.

[45] Matthew Pelliccione and Toh Ming Lu, Evolutionn of thin film morphology: Modeling and simulations, Springer. (2008).

TH-2097_126121019

[46] H. Antonio, S. Hegedus, Handbook of photovoltaic science and engineering, Willey. (2003). doi:10.1002/9780470974704.

[47] Stephen J Fonash, Solar cell device physics, Elsevier. (2010). doi:10.1016/0025-5408(82)90173-8.

[48] Ramakrishna Madaka, Venkanna Kanneboina, Pratima Agarwal, Low-Temperature Growth of Amorphous Silicon Films and Direct Fabrication of Solar Cells on Flexible Polyimide and Photo-Paper Substrates, J. Eectronic Mater. 47 (2018) 4710–4720. doi:10.1007/s11664-018-6344-0.

[49] Ramakrishna Madaka, Venkanna Kanneboina, Pratima Agarwal, Enhanced performance of amorphous silicon solar cells (110°C) on flexible substrates with a-SiC:H(p) window layer and H_2 plasma treatment at n/i and i/p interface, Semicond. Sci. Technol. 33 (2018) 3.

TH-2097_126121019

Chapter 3

Influence of Hydrogen Plasma Treatment on Microstructural, Optical and Electrical Properties of a-Si:H(i) Thin Films

This chapter presents the influence of hydrogen plasma treatment on the growth of nano crystalline silicon phase in a-Si:H films. Very thin and good quality layer of a-Si:H films play a crucial role in passivation of defect states on the c-Si wafer and interfaces of silicon heterojunction (SHJ) solar cells [1–4]. In order to improve the microstructure, optical and electrical properties of the a-Si:H films for c-Si/a-Si:H heterojunction solar cells, a-Si:H films have been subjected to intermittent hydrogen plasma during growth of the films. The evolution of nanocrystalline Si phase due to intermittent hydrogen plasma treatment of a-Si:H films is studied through Spectroscopic Ellipsometry(SE), Raman, TEM and FTIR absorption spectroscopy. SE and UV-Vis-NIR measurements were used to determine the optical constants, thickness and band gap of the films. Electrical properties were studied by conductivity measurements.

3.1. Experimental details

The intrinsic a-Si:H thin films were deposited on corning 1737 glass and undoped silicon substrates using capacitively coupled radio frequency plasma enhanced chemical vapour deposition (RFPECVD) technique. During the growth of a-Si:H films, the silane plasma was interrupted and films were exposed to pure H_2 plasma to improve the microstructure of the films. The total deposition time for each film was kept constant at 60 min and each hydrogen plasma treatment step was of 5 min duration. The deposition parameters used for SiH_4 plasma for deposition of a-Si:H(i) layer were: Silane flow rate (SFR) of 6 SCCM, RF power of 35 W, substrate temperature of 200 ^{o}C and process pressure (PP) of 0.42 mbar. For hydrogen plasma treatment (HPT), hydrogen flow rate (HFR) of 26 SCCM at PP of 0.42 mbar, RF power of 60 W (RF frequency of 13.56 MHz) and substrate temperature of 200 ^{o}C were used. For *HP_0* film, no hydrogen plasma treatment was carried out during deposition, whereas for *HP_1*, after 30 min of film deposition (SiH_4 plasma), the films were subjected to 5 min of H_2 plasma

treatment followed by another 30 min of deposition (SiH_4 plasma). Similarly, for *HP_2* and *HP_3*, the films were subjected to 5 min hydrogen plasma after each 20 min and 15 min of deposition (for 2 and 3 times) respectively. No plasma treatment was carried out on the top surface of the films. The schematic of deposition and hydrogen plasma treatment for each series is shown in Fig. 3.1.

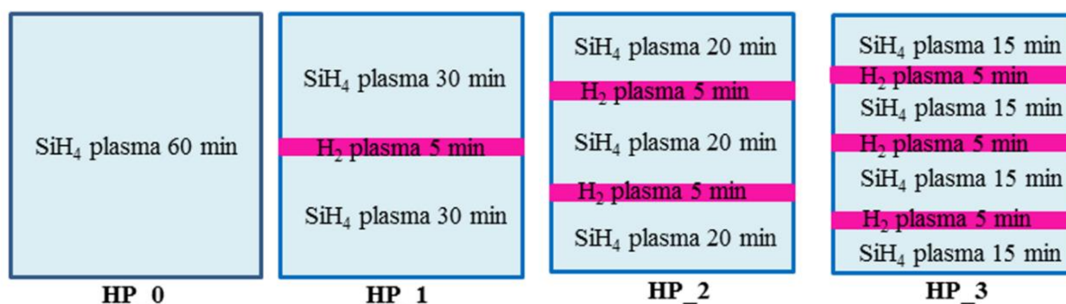

Fig. 3.1. Hydrogen plasma treatment steps during a-Si:H film growth.

Raman scattering studies were performed on a-Si:H films deposited on corning substrate at room temperature. The SE measurements were carried out on films deposited on corning substrate in the range of 2-5 eV at an incident angle of 70° and data analysis was performed using SEA software as described in section 2.2.3, Chapter 2. Transmission spectra of the a-Si:H thin films were measured with UV-Vis-NIR spectrometer in the wavelength range of 200 to 2500 nm. AFM was used to study the surface morphology and roughness of the films. The dark and photo conductivity of the films deposited on corning 1737 substrate were measured under vacuum (~10^{-6} mbar) in coplanar geometry with Ag electrodes of 5 mm length at a separation of 1 mm in the temperature range 300-475K to estimate the activation energy. For TEM measurements, *HP_0* and *HP_3*, films were scratched and sonicated in acetone for a few minutes and dispersed on copper mesh. The FTIR transmission measurements were done on the films, which were simultaneously deposited on undoped crystalline silicon, in the range of 400-2300 cm^{-1}. All the measurements, except FTIR, were done on films deposited on corning 1737 glass. The details of all these characterization techniques used in the present study are given in Chapter 2.

3.2. Results and discussion

3.2.1. Structure evaluation by TEM analysis

In order to evaluate structure of the a-Si:H films with and without H_2 plasma treatment, TEM measurements were done on the samples transferred on Cu mesh (Section 2.2.2, Chapter 2).

TH-2097_126121019

TEM images of *HP_0* and *HP_3* samples are shown in Fig. 3.2(a, b) and corresponding selective area electron diffraction (SAED) pattern are shown in Fig. 3.2 (c, d). Fig 2e shows HRTEM image of *HP_3* film. A blurred image in Fig. 3.2a and diffused diffraction rings in Fig. 3.2c, correspond to the amorphous structure of the *HP_0* film when no plasma treatment was carried out. Whereas nano-crystallites can be seen in Fig. 3.2b. Bright spots on the diffused diffracted rings (Fig. 3.2d) are strong evidence of nano crystalline nature of the *HP_3* film. The porous nanocrystalline structure of *HP_3* film (Fig. 3.2b) is due to etching effect of H_2 plasma. The inter-planer spacing (d-spacing), as calculated from HRTEM image (Fig. 3.2e), are 0.328 and 0.257 nm corresponding to (111) and (220) planes of Si respectively [5,6].

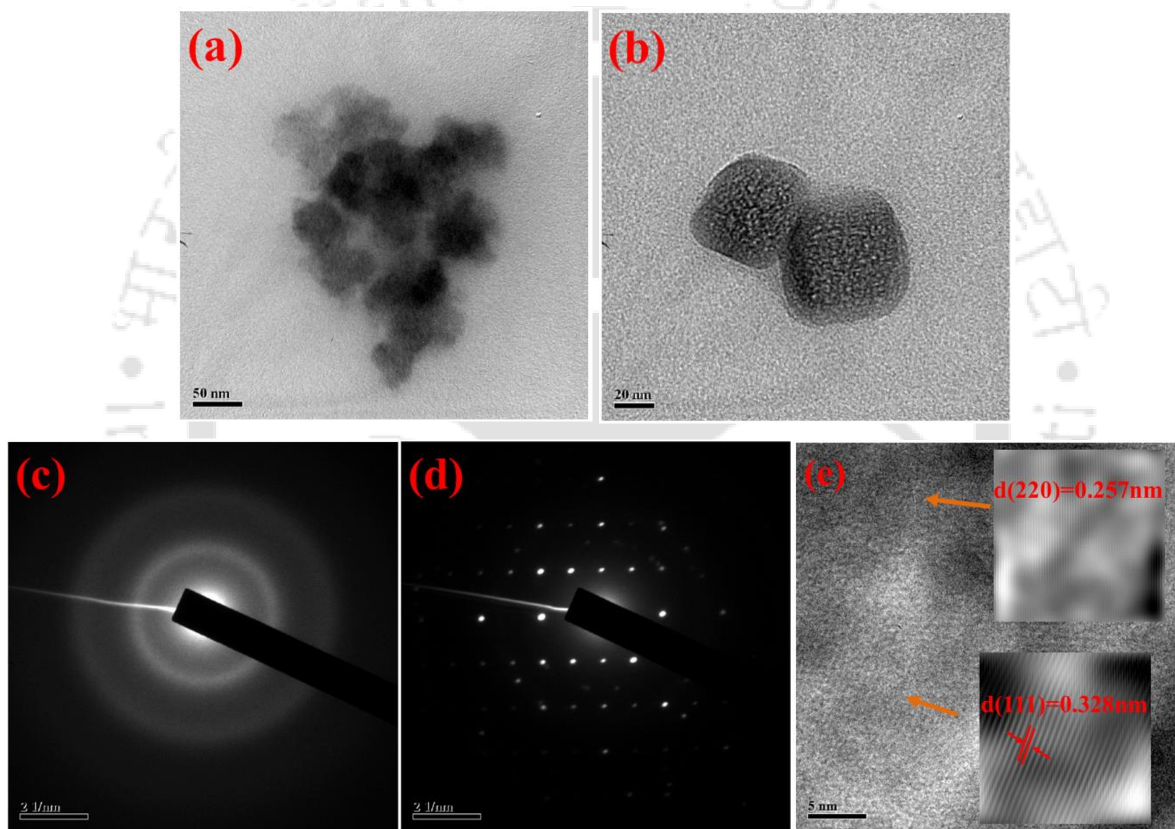

Fig. 3.2 (a,b) TEM images of *HP_0*, *HP_3* films and (c,d) SAED patterns of *HP_0*, *HP_3* films and (e) HRTEM image of *HP_3* film.

3.2.2. Structure evaluation by Raman studies

Fig. 3.3(a, b) show the Raman spectra of *HP_0-HP_3* films and deconvoluted Raman spectra of *HP_ 2* film respectively. In Raman spectra, for *HP_0* and *HP_1* films, most intense peak at 480 cm^{-1} corresponds to the transverse optic (TO) mode of a-Si:H, whereas peaks at 410 cm^{-1}, 310 cm^{-1} and 150 cm^{-1} correspond to longitudinal optic (LO) mode, longitudinal acoustic (LA) mode and transverse acoustic (TA) mode respectively [7,8]. For *HP_0* and *HP_1* films, peak

TH-2097_126121019

at 480 cm^{-1} indicates amorphous nature of these films [9–11]. The observation of these peaks indicate that one step plasma did not affect the microstructure of the films significantly. In case of *HP_2* and *HP_3*, another peak near 500-510 cm^{-1} corresponding to the TO mode for nc-Si, is observed. Raman spectra of *HP_2* and *HP_3* could be deconvoluted in to the peaks corresponding to TO mode of a-Si:H (480 cm^{-1}), grain boundaries (~500 cm^{-1}) and nc-Si (~510 cm^{-1}) [12]. The ratio of intensities of peaks corresponding to TA and TO mode of a-Si (I_{TA}/I_{TO}), which is a measure of dihedral bond angle deviation $\Delta\phi$ provides the information on medium range order (MRO). The tetrahedral bond angle deviation $\Delta\theta$ was estimated from FWHM of TO mode of the films (Eq. 2.1) [7], which is measure of the short range order (SRO) of the films. The crystalline (X_c) (Eq. 2.2), nano crystalline (X_{nc}) (Eq. 2.3), grain boundary (X_{gb}) (Eq. 2.4) volume fractions and crystallite size (d_{Raman}) (Eq. 2.5) of the films were calculated as described in section 2.2.1, Chapter 2 [13–15] and the values are listed in Table 3.1. Fig. 3.4. shows the ratio of I_{TA} to I_{TO} (I_{TA}/I_{TO}) and bond angle deviations ($\Delta\theta$) as a function of number of H_2 plasma steps. As it is evident from Table 3.1 and Fig. 3.4 that both $\Delta\theta$ and I_{TA}/I_{TO} ($\Delta\phi$) have decreased with increase in HPT steps. This reflects an improvement in structural ordering upon HPT of the films. As films are subjected to the hydrogen plasma, bonding disorder is reduced and weak Si-Si bonds are replaced with strong Si-Si bonds. The crystallite size as well as crystalline volume fraction of *HP_3* film are also higher than that of *HP_2* film. The HPT initiates the formation of nanocrystallite in the films. During subsequent HPT, the amorphous phase around the crystalline regions is further etched and the crystalline growth is enhanced in *HP_2* and *HP_3* [16–19].

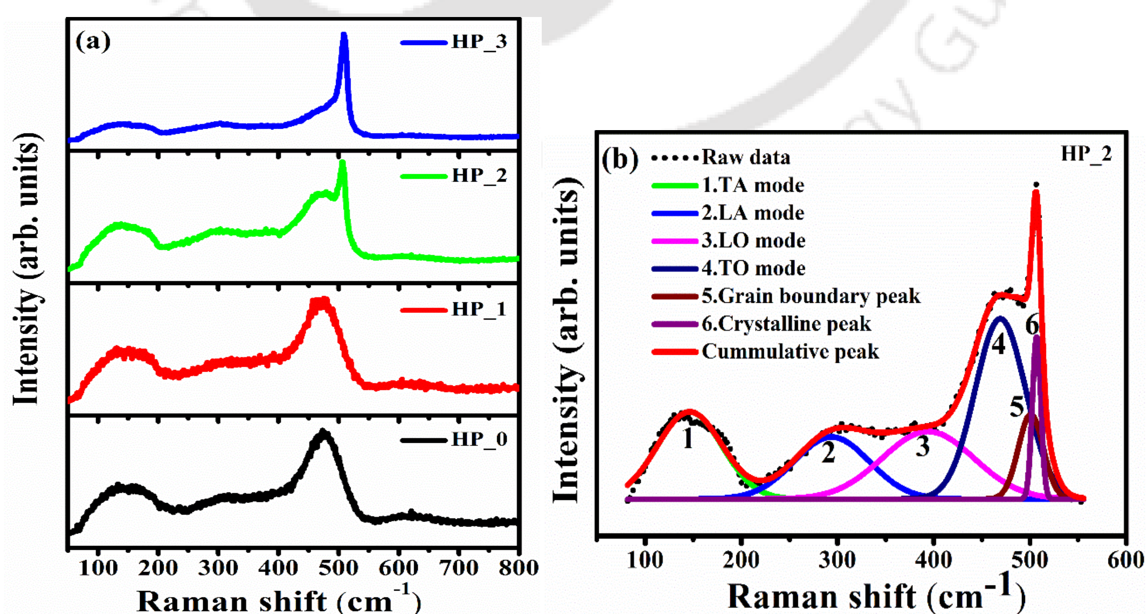

Fig. 3.3. Raman spectra of *HP_0* to *HP_3* (a) and deconvulated spectra of *HP_2* (b) films.

TH-2097_126121019

Table 3.1. Crystalline (X_c), nano crystalline (X_{nc}), grain boundary(X_{gb}) volume fractions and bond angle deviations (I_{TA}/I_{TO} and $\Delta\theta$) calculated from Raman spectra. Hydrogen content (C_H) and microstructure (R^*) factor calculated from FTIR measurements.

	Raman						FTIR	
Sample	X_c (%)	X_{nc} (%)	X_{gb} (%)	d_{Raman} (nm)	I_{TA}/I_{TO}	$\Delta\theta$ (°)	C_H (%) at 640 cm^{-1}	R^*
HP_3	50.4	26.0	24.3	2.7	0.55	7.5	12.6	0.38
HP_2	27.6	10.8	16.7	2.4	0.59	7.8	11.3	0.46
HP_1					0.67	7.8	10.6	0.54
HP_0					0.73	8.2	9.6	0.57

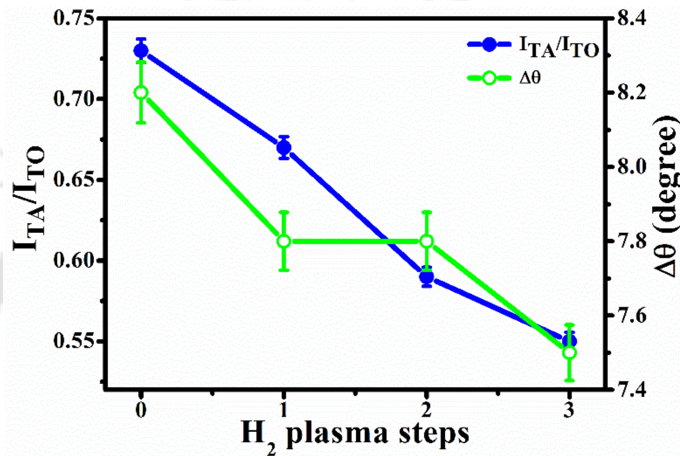

Fig. 3.4. Ratio of I_{TA} to I_{TO} (I_{TA}/I_{TO}) and bond angle deviations as a function of number of H_2 plasma steps (Error bars are included in figure).

3.2.3. FTIR analysis for the evaluation of hydrogen content

Fig. 3.5 shows the FTIR transmission spectra of *HP_0* to *HP_3* films. In Fig. 3.5, wagging and stretching modes of Si–H bonds are present at 640 cm^{-1} and 2000 cm^{-1} respectively. The total hydrogen content (C_H) and microstructure factor R^* were estimated using Eq. 2.16 and Eq. 2. 17 as described in section 2.2.5, Chapter 2 [13–15] and the values are listed in Table 3.1 and also shown in Fig. 3.6. It is observed that H_2 content in the films increases whereas R^* decreases with increase in HPT steps. These results indicate that HPT results in breaking of weak Si-H_2 bonds and favours the strong Si-H bonds, thus producing a more ordered and relaxed network with low void fraction [20]. The increase in hydrogen content also results in an increase in band gap as estimated using UV-Vis-NIR transmission and SE measurements (discussed later). The amount of hydrogen bonded as Si-H and Si-H_2 is also calculated from the deconvoluted absorption peaks near 2000 and 2100 cm^{-1} as described in section 2.2.5, Chapter 2 and also shown in Fig. 3.6.

TH-2097_126121019

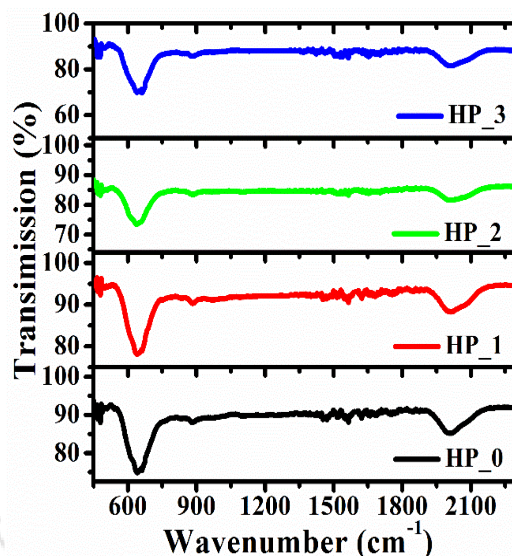

Fig. 3.5. FTIR transmission spectra of *HP_0* to *HP_3* films.

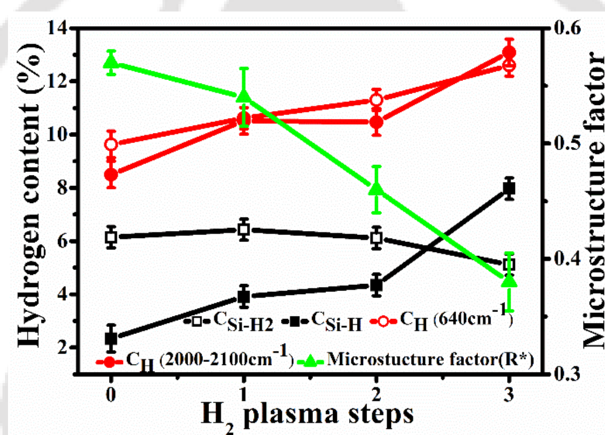

Fig. 3.6. Hydrogen content and microstructure factor of *HP_0* to *HP_3* films as a function of H_2 plasma steps.

3.2.4. UV-Vis-NIR spectroscopy studies for band gap and thickness evaluation

Fig. 3.7 shows the UV-Vis-NIR transmission spectra of *HP_0* to *HP_3* films. It is observed that the all the films are very uniform and highly transparent in high wavelength region. Refractive index (Eq. 2.18) and thickness (Eq. 2.20) of a-Si:H films are calculated using swanepoel's method [21] as described in section 2.2.6, Chapter 2 and band gap is obtained from the Tauc's plot using Eq. 2. 21 [22]. These values are listed in Table 3.2. The thickness of *HP_0* film, without any plasma treatment, is estimated as 1475 nm. Further, thickness of films is found to decrease with increase in number of HPT steps; thickness of *HP_0* to *HP_3* films being 1475, 1060, 730 and 670 nm respectively (Table 3.2). This observed decrease in thickness with increase in number of HPT steps is because of etching of film during HPT and subsequently different growth mechanism which influences the deposition rate. The effective

TH-2097_126121019

deposition rate of these films is estimated as 24.58, 17.66, 12.16 and 11.16 nm correspond to *HP_0* to *HP_3* films respectively. It is also observed that optical band gap of the a-Si:H films has increased from 1.79 to 1.86 eV and refractive index (at 632 nm) from 3.3 to 3.9 with increase in number of H_2 plasma treatments (Fig. 3.8). This is due to increase in hydrogen content in the films and rearrangement of Si network with improved microstructure as confirmed by the Raman and FTIR spectroscopy measurements discussed in the earlier sections (3.2.2 and 3.2.3).

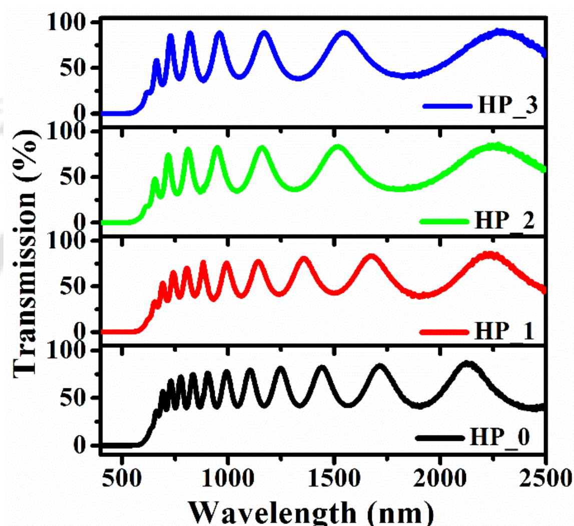

Fig. 3.7. Transmission spectra of *HP_0* to *HP_3* films.

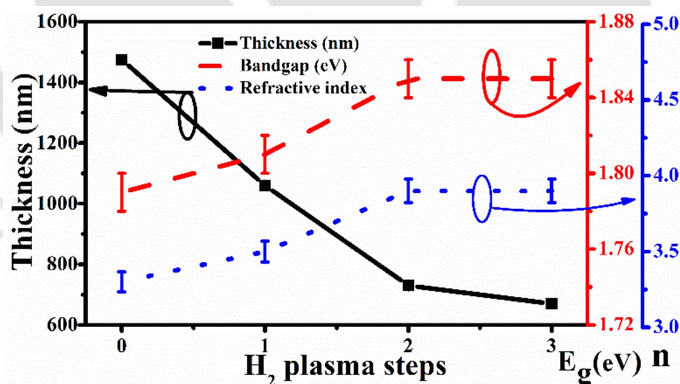

Fig. 3.8. Thickness, band gap (E_g) and refractive index plotted as function of H_2 plasma steps.

3.2.5. Spectroscopic ellipsometry (SE) analysis for evaluation of optical constants and microstructure

Fig. 3.9 show the real ($< \varepsilon_1 >$) and imaginary ($< \varepsilon_2 >$) parts of pseudo dielectric function as a function of photon energy, as derived from the measured ψ and Δ values in SE. Details of $< \varepsilon_1 >$ and $< \varepsilon_2 >$ expressions are given in section 2.2.3, Chapter 2 (Eq. 2.7). For reference, the dielectric function for the c-Si wafer, derived from SE measurements, is also shown in Fig.

TH-2097_126121019

3.9. The distinct peaks in $<\varepsilon_2>$ spectra at 3.4 eV and 4.2 eV correspond to direct band to band transitions in crystalline and nano/micro crystalline silicon thin films [23–25]. A first look at these figures indicates that both $<\varepsilon_1>$ and $<\varepsilon_2>$ for the *HP_3* film have a similar variation with energy as that for c-Si, suggesting that the microstructure of this sample is very similar to that of c-Si. Though, the magnitude of $<\varepsilon_2>$ for *HP_3* film at these positions is smaller compared to that for c-Si, which could be due to smaller size of grains in the film [26,27]. For *HP_2* film, though no distinct peak and dip in $<\varepsilon_1>$ and peaks at 3.4 eV and 4.2 eV in $<\varepsilon_2>$ are seen, however a shallow peak and dip in $<\varepsilon_1>$ and broad hump in $<\varepsilon_2>$ corresponding to two broad overlapping peaks is clearly observed, which suggests that this film has improved microstructure. The magnitude of $<\varepsilon_2>$ near 3.4 and 4.2 eV for *HP_2* is also same as that for *HP_3* film at these positions. This suggests the partial crystallization of the *HP_2* and *HP_3* films.

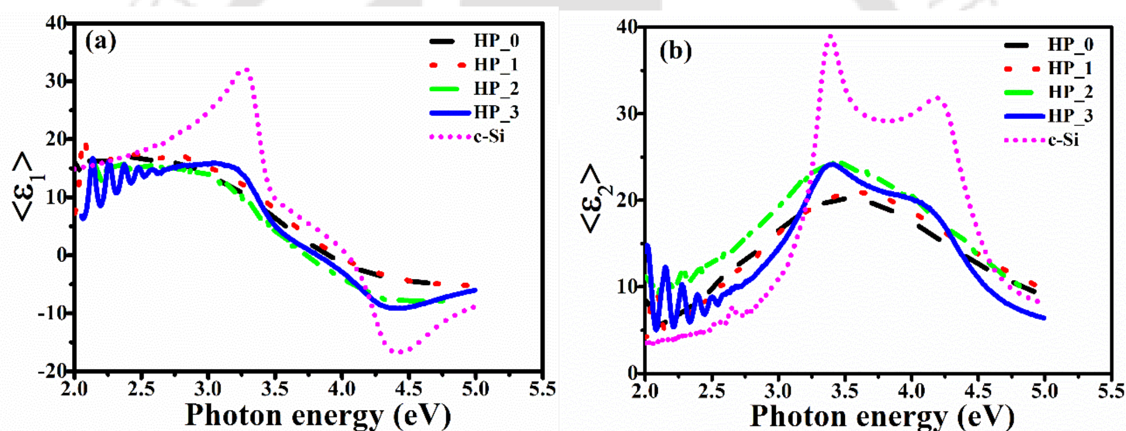

Fig. 3.9. a) Real ($<\varepsilon_1>$) and b) Imaginary ($<\varepsilon_2>$) part of pseudo dielectric function measured as a function of photon energy for *HP_0* to *HP_3* films and c-Si.

For *HP_0* and *HP_1* films, the trend that $<\varepsilon_1>$ decaying non-linearly with energy whereas $<\varepsilon_2>$ having a broad hump with peak position near 3.5-3.6 eV, is similar to the trend reported for a-Si:H films [23,28,29]. A peak at 3.5-3.6 eV in $<\varepsilon_2>$ is characteristic of a-Si:H films. The amplitude of $<\varepsilon_1>$ for *HP_1* film is slightly more than that of *HP_0* and the peak position in $<\varepsilon_2>$ for *HP_1* is slightly shifted toward higher energy (~3.6 eV) as compared to that for *HP_0* (3.5 eV). These observations suggest that though one time HPT does not significantly alter the microstructure of the a-Si:H films (*HP_1*), however there is a slight improvement in bonding configuration and reduction in defect density which lead to a shift in peak position to higher energy.

The amplitude of $< \varepsilon_2 >$ in SE spectra is a measure of refractive index and thus the density of the films [30]. In case of a-Si:H, where hydrogen atoms are present in silicon matrix, the dense network with higher refractive index is formed when H_2 is bonded as monohydride (Si-H) and the atomic percent of hydrogen is low. On the other hand, if hydrogen is bonded as Si-H_2, Si-H_n, the voids are formed and effective refractive index is lowered. Now if we look at the amplitude of $< \varepsilon_1 >$ and $< \varepsilon_2 >$ for a-Si:H films with and without hydrogen plasma treatment, it is observed that amplitudes of both $< \varepsilon_1 >$ and $< \varepsilon_2 >$ increase with increase in HPT steps for *HP_0* to *HP_2* films. This can be attributed to increase in density of films due to the improvement in bonding arrangement and microstructure of these films when subjected to hydrogen plasma. During HPT, a large flux of atomic hydrogen arriving on the film surface breaks the weak Si-Si bonds and replaces these with strong Si-Si bonds. Hydrogen atoms also diffuse in to the bulk of the films and improve the structure of the films [31]. During subsequent growth, the Si atoms arriving on the surface prefer to maintain this structural ordering rather than forming a random network. However, this process continues for a few atomic layers only and once again a random network of Si atoms is formed resulting in growth of a-Si:H. For *HP_1*, the film is subjected to HPT only once and subsequent deposition was for a longer period (30 min), which did not change the microstructure of the films. However, for *HP_2* film, with two times H_2 plasma steps followed by smaller deposition times (20 min each), transformation from a-Si:H to nc-Si:H started which resulted in to a mixed phase of amorphous and nano crystalline films. For *HP_3*, one more HPT step was introduced followed by further reduced deposition time (5 min H_2 plasma after each 15 min SiH_4 deposition), which resulted in to the formation of nanocrystallites in the films and increase in intensity of the peaks at 3.4 eV and 4.2 eV.

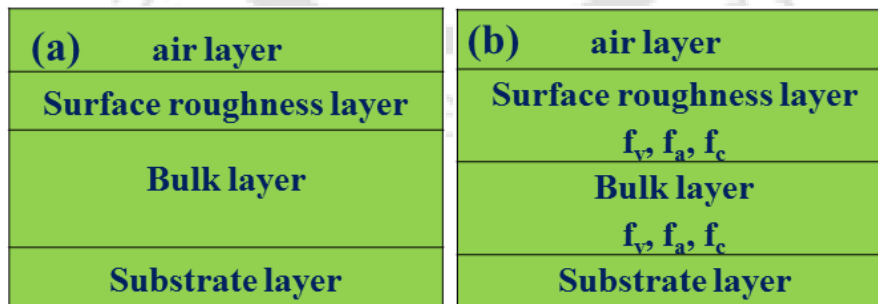

Fig. 3.10: a) Schematic Two-layer model for TL, TL+Gauss and b) TL +BEMA model.

Several models have been used for investigation of a-Si:H/nc-Si:H films through the analysis of dielectric function such as Tauc-lorentz (TL)[32], Cody-Lorentz model [33], Forouhi-Bloomer model [34,35], Tetrahedral model [25], Harmonic oscillator model and Bruggman

TH-2097_126121019

effective medium approximation model (BEMA) etc. However, it is very important to choose suitable model and ensure the best fitting to obtain precise and valid results. Among these models, TL model [36], Gauss model [30] and combination of these models are mostly used and details of those models are given in section 2.2.3, Chapter 2.

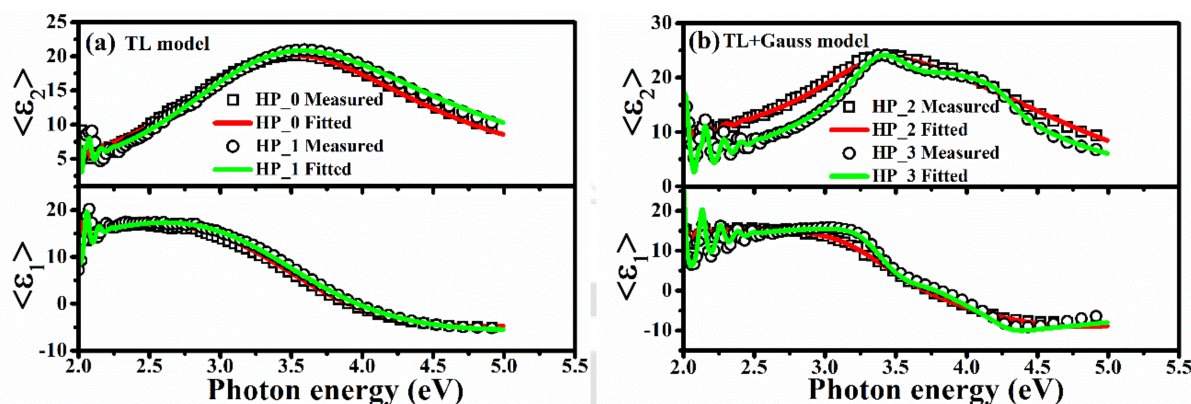

Fig. 3.11: Measured and fitted values of real ($<\varepsilon_1>$) and imaginary ($<\varepsilon_2>$) part of pseudo dielectric function as a function of photon energy, a) *HP_0*, *HP_1* films (fitted with TL model) and b) *HP_2*, *HP_3* films (fitted with TL and Gauss model).

The TL model (Eq. 2.9 and Eq.2. 10) along with BEMA (Eq. 2.11) has also been used to determine the amorphous, nanocrystalline and void fraction in a-Si:H/nc-Si:H films [30,37]. In our case, we have used TL and a combination of TL and Gauss models (Eq. 2.12 and Eq. 2.13) to fit the dielectric function of amorphous films (*HP_0* and *HP_1*) and mixed phase films (*HP_2* and *HP_3*) respectively. Two-layer structure; *corning substrate/bulk layer/surface roughness layer/air* (Fig. 3.10a) is used to estimate the band gap, optical constants and thickness of these films. The measured values of dielectric constant as a function of photon energy and those obtained using model fitting are shown in Fig. 3.11. For amorphous films (*HP_0* & *HP_1*), TL model alone could give a good fitting to the experimental data with single peak in $<\varepsilon_2>$ corresponding to a-Si:H around 3.5-3.6 eV, whereas for films with signature of nanocrystallinity (*HP_2* & *HP_3*), Gauss model is used to fit the two band to band transition near 3.4 and 4.2 eV along with the TL model used for fundamental transition near 3.6 eV. The initial values of different peaks for the fitting were obtained by deconvoluting the peak in $<\varepsilon_2>$ spectra of these samples using the peak fit program of the software ORIGIN 8.5. The calculated values of thickness, band gap and refractive index (at 632 nm) of the films from SE measurements are listed in Table 3.2 along with the corresponding values obtained from the UV-Vis-NIR transmission data. The values of the fitted parameters A, E_0, C and E_g are listed in Table 3.3. The thickness and band gap values obtained from UV-Vis-NIR transmission and

TH-2097_126121019

SE measurements match quite well. The quality of fitting (goodness of fitting) (R^2) of these models is 99% and estimated errors are included in figures.

Table 3.2. Thickness (d), band gap (E_g) and refractive index (n) of the films calculated from using UV-Vis-NIR and SE measurements.

	UV-Vis-NIR			TL+Gauss model[#]/ TL model[*]				TL+BEMA model			
Sample	d (nm)	E_g (eV)	n	d_{bulk} (nm)	E_g (eV)	n	d_s (nm)	d_{bulk} (nm)	E_g (eV)	n	d_s (nm)
[#]*HP_3*	670	1.85	3.9	665	1.86	4.2	7.59	663	1.86	3.8	8.8
[#]*HP_2*	730	1.84	3.9	723	1.84	4.1	3.78	725	1.84	3.7	4.7
[*]*HP_1*	1060	1.81	3.5	1062	1.81	3.6	2.46	1060	1.81	3.7	2.3
[*]*HP_0*	1475	1.79	3.3	1466	1.80	3.4	2.13	1475	1.80	3.2	1.9

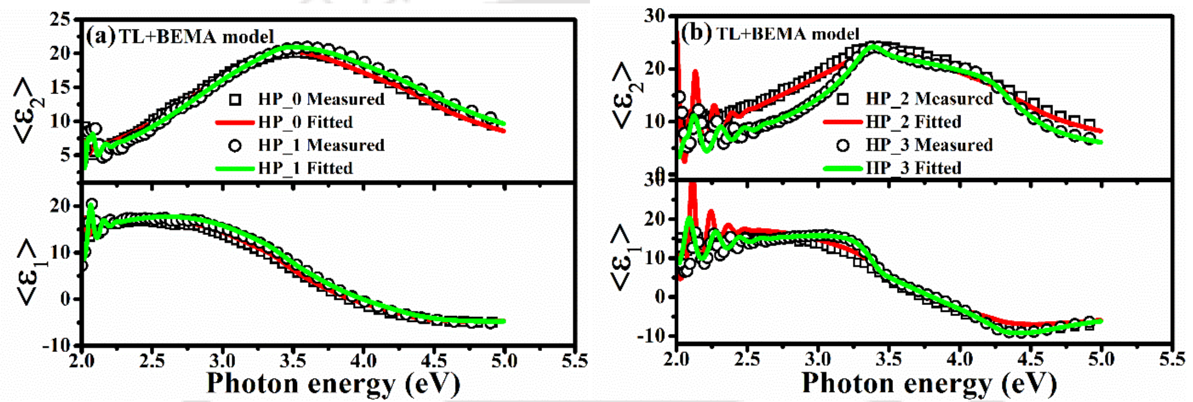

Fig. 3.12: Measured and fitted values of $< \varepsilon_1 >$ and $< \varepsilon_2 >$ as a function of photon energy, a) *HP_0*, *HP_1* films and b) *HP_2*, *HP_3* films (fitted with TL and BEMA model).

We have also used TL model along with BEMA to estimate the amorphous (f_a), crystalline (f_c) and void (f_v) volume fractions, thickness of bulk and surface layer along with band gap and optical constants of the bulk layer of the films. For this, we have taken two-layer structure; *corning substrate/bulk layer/surface roughness layer/air* (Fig. 3.10b). Both, bulk as well as surface layers consist of a mixture of amorphous, crystalline and void phases [30,38,39]. The measured values of dielectric constant as a function of photon energy were fitted using TL+BEMA as shown in Fig. 3.12. The values of the fitted parameters A, E_0, C and E_g as obtained using TL+BEMA, are also listed in Table 3.3 and corresponding values of thickness, band gap and refractive index (at 632 nm) are listed in Table 3.2. The calculated values of amorphous, crystalline and void fraction for both bulk layer and rough surface layer are listed in Table 3.4 along with the surface roughness values obtained from AFM. It is evident from these tables that there is a good agreement between the values of A, E_0, C and E_g between the two models, (TL/TL+Gauss and TL+BEMA). The value of amplitude parameter (A) is found to increase and broadening parameter (C) is found to decrease with increase in number of H_2

TH-2097_126121019

plasma steps (Table 3.3). These observations suggest an improvement in structural ordering with HPT. It is also observed that amorphous and void volume fractions have decreased and that of crystalline phase has increased with increase in hydrogen plasma steps (Fig. 3.13).

Table 3.3. Model fitted parameters (A, E_0, C and E_g) of *HP_0* to *HP_3* films.

	TL+Gauss model#/ TL model*				TL+BEMA model			
Sample	A (eV)	E_0 (eV)	C (eV)	E_g (eV)	A (eV)	E_0 (eV)	C (eV)	E_g (eV)
#*HP_3*	247.6	E_1:3.42 E_2:3.65 E_3:4.20	2.15	1.86	245	3.66	2.12	1.86
#*HP_2*	247.4	E_1:3.41 E_2:3.65 E_3:4.18	2.16	1.84	245	3.65	2.13	1.84
**HP_1*	238	3.64	2.36	1.81	235	3.61	2.35	1.81
**HP_0*	235	3.59	2.51	1.80	234	3.51	2.43	1.80

Table 3.4. Thickness, void, amorphous and crystalline fraction of bulk and surface roughness layer of *HP_0* to *HP_3* films calculated from SE and RMS roughness from AFM measurements.

	Bulk layer				Surface roughness layer				AFM
Sample	d_{bulk} (nm)	f_v (%)	f_a (%)	f_c (%)	d_s (nm)	f_v (%)	f_a (%)	f_c (%)	d_{RMS} (nm)
HP_3	663	6.8	43.0	50.1	8.81	11.5	51.0	37.4	7.4
HP_2	725	9.2	71.8	19.0	4.76	16.0	71.7	12.2	3.7
HP_1	1060	10.2	84.7	5.0	2.34	24.5	71.5	3.9	1.9
HP_0	1475	18.7	80.5	0.7	1.99	31.9	67.7	0.3	1.5

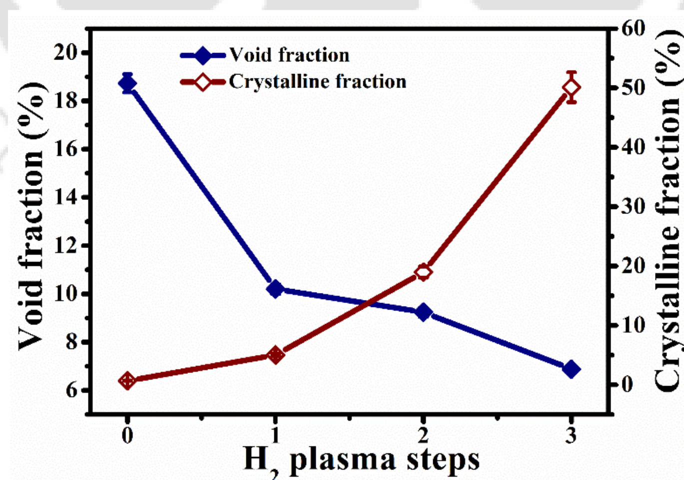

Fig. 3.13. Void and crystalline fraction plotted as function of H_2 plasma steps.

TH-2097_126121019

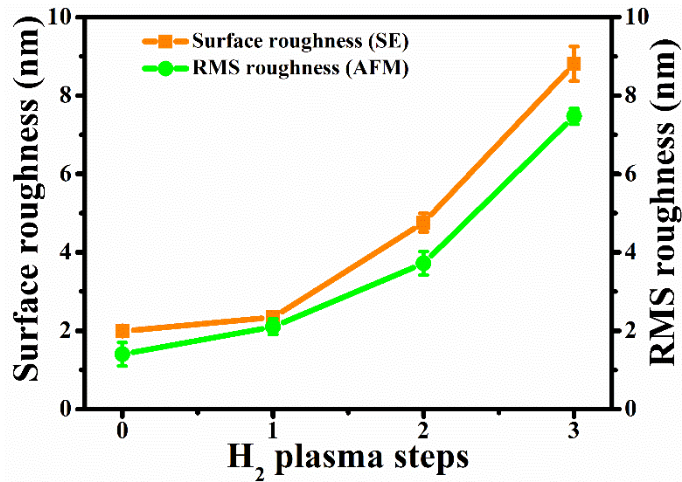

Fig. 3.14. Surface and RMS roughness of films as a function of number of H_2 plasma steps.

The thickness, band gap and refractive index (at 632 nm) calculated using two models also agree well with the values obtained from the UV-Vis-NIR transmission data. The roughness of the films from the AFM studies is also quite similar to thickness of the rough surface layer (d_s) (Fig. 3.14).

The amplitude of the $< \varepsilon_2 >$ spectra is related to the refractive index n and extinction coefficient k as $\varepsilon_2(E) = 2n(E)k(E)$. As seen in Fig. 3.9b, amplitude of $< \varepsilon_2 >$ for amorphous films *HP_0* and *HP_1* is 20.20 and 20.93 respectively, which is much less than the corresponding values 24.03 and 24.16 for nanocrystallites embedded *HP_2* and *HP_3* respectively. Amorphous film (*HP_0*) without any hydrogen plasma treatment show a larger void fraction (~19%), which is significantly reduced to 10% with one-time hydrogen plasma treatment (*HP_1*) and is further reduced with increasing number of HPT steps (Table 3.4). FTIR analysis also shows a larger microstructure factor R^* for amorphous films, which indicates that a larger fraction of total hydrogen present in these films is bonded as SiH_2, SiH_3 or SiH_n (higher hydride).

A direct correlation is observed between the R^* and void fraction in these films (Fig. 3.15). Though an increase in amount of total hydrogen content is observed with increase in HPT steps, the amount of hydrogen bonded as SiH_2, SiH_n is found to decrease slightly (Fig. 3.6). This implies that atomic hydrogen arriving at the surface during plasma treatment steps not only breaks weak Si-Si bonds but also diffuses in to the bulk and passivates the coordination defects, replaces weak Si-H_2 bonds with strong Si-H bonds resulting in a dense structure which is evident as an increase in refractive index (Table 3.2). At first sight, it may appear to contradict the perception that an increase in hydrogen content would result in a decrease in density of the

TH-2097_126121019

films and thus refractive index. However, as the bond length of Si-H bonds is low compared to that of Si-Si bonds, hydrogen bonded as Si-H increases the density of the films [40].

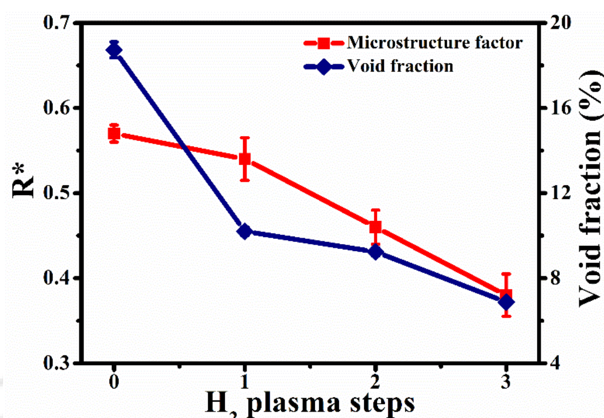

Fig. 3.15. Microstructure factor and void fraction as a function of number of H_2 plasma steps.

Fig. 3.16 shows the calculated values of n and k as a function of photon energy for the films and a clear and systematic trend is observed near the fundamental (3.6 eV) and band to band transition (4.2 eV) positions. A shift in peak position of the fundamental mode towards the higher energy for hydrogen plasma treated films (~3.64 eV) compared to that for untreated film (3.59 eV) also indicates an improvement in structural ordering of the films after subjecting the growing surface to hydrogen plasma. This conjecture is further supported by the decrease in broadening parameter (Table 3.3 and Fig. 3.17), which is a measure of the disorder in the films[28,30].

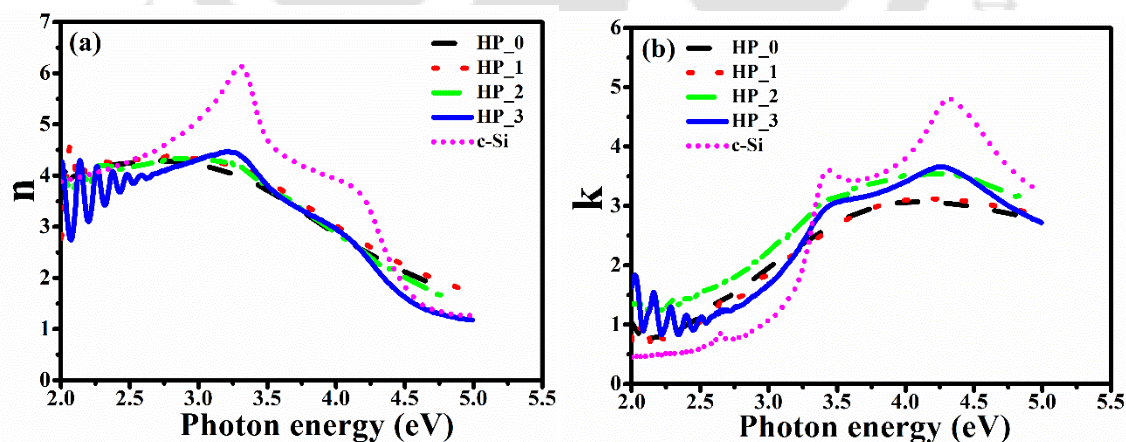

Fig. 3.16: a) Refractive index and b) excitation coefficient of *HP_0* to *HP_3* films measured as a function of photon energy by using TL and BEMA model.

Our results show that with increase in HPT steps, not only the total hydrogen content in the films is increased but the amount of hydrogen bonded as strong Si-H bonds is also increased (Fig. 3.6). The band gap is thus increased as Si-H bonds have larger energy compared to Si-Si

TH-2097_126121019

bonds and the valence band is lowered in the films [40]. Figure 3.17 shows the increase in band gap with total hydrogen content in the films. It is observed that the band gap increases almost linearly with the total hydrogen content. The peak amplitude of $< \varepsilon_2 >$ is also found to increase with C_H and broadening parameter is reduced (Fig. 3.17). The thickness of the film (Fig. 3.8) decreases with increasing plasma treatment steps due to i) etching of the amorphous phase and ii) lower growth rate of nc-Si:H phase [41]. Initially, when a large portion of amorphous phase is to be etched out, thickness decreases rapidly, however, when a major portion of the a-Si:H phase is etched out by subsequent plasma treatment and a stable nc-Si phase remains, the rate of decrease of total thickness is lowered. The microvoids in a-Si:H films have been identified as the source of light induced degradation in a-Si:H films. A decrease in its density upon one-time plasma treatment without changing the amorphous nature of the films is expected to improve the stability of these films against exposure to light [42].

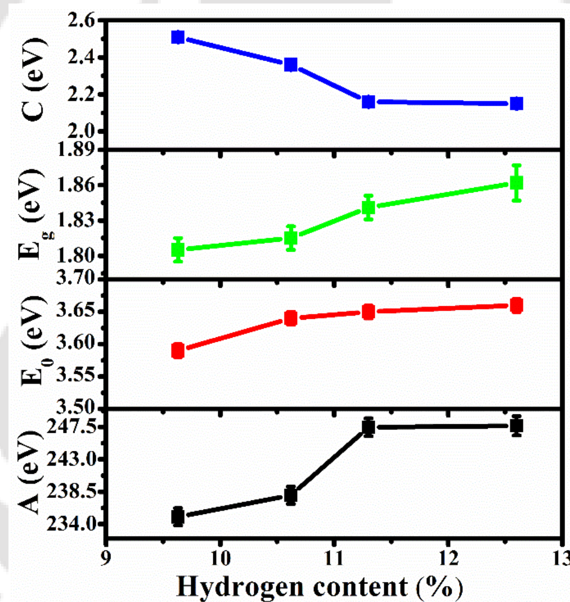

Fig. 3.17. TL model parameters (A, E_0, E_g and C) of *HP_0-HP_3* films as a function of hydrogen content (C_H).

3.2.6. Morphology studies by AFM

To study the morphology of the films, AFM measurements were performed in non-contact mode on the films deposited on corning glass. Fig. 3.18 show the surface morphology of the *HP_0* to *HP_3* on 2x2 μm^2 area of the films. It is clearly observed that films are very uniform throughout the area. The small size grains are observed in *HP_0* and *HP_1* films with grain size increasing in *HP_2*, *HP_3* films. This is due to changes in nucleation and growth process in the films by HPT. The RMS surface roughness (d_{RMS}) values of the films obtained from

TH-2097_126121019

AFM measurements are found to be 1.55, 1.92, 3.73 and 7.47 nm corresponding to *HP_0* to *HP_3* films respectively and also listed in Table 3.4.

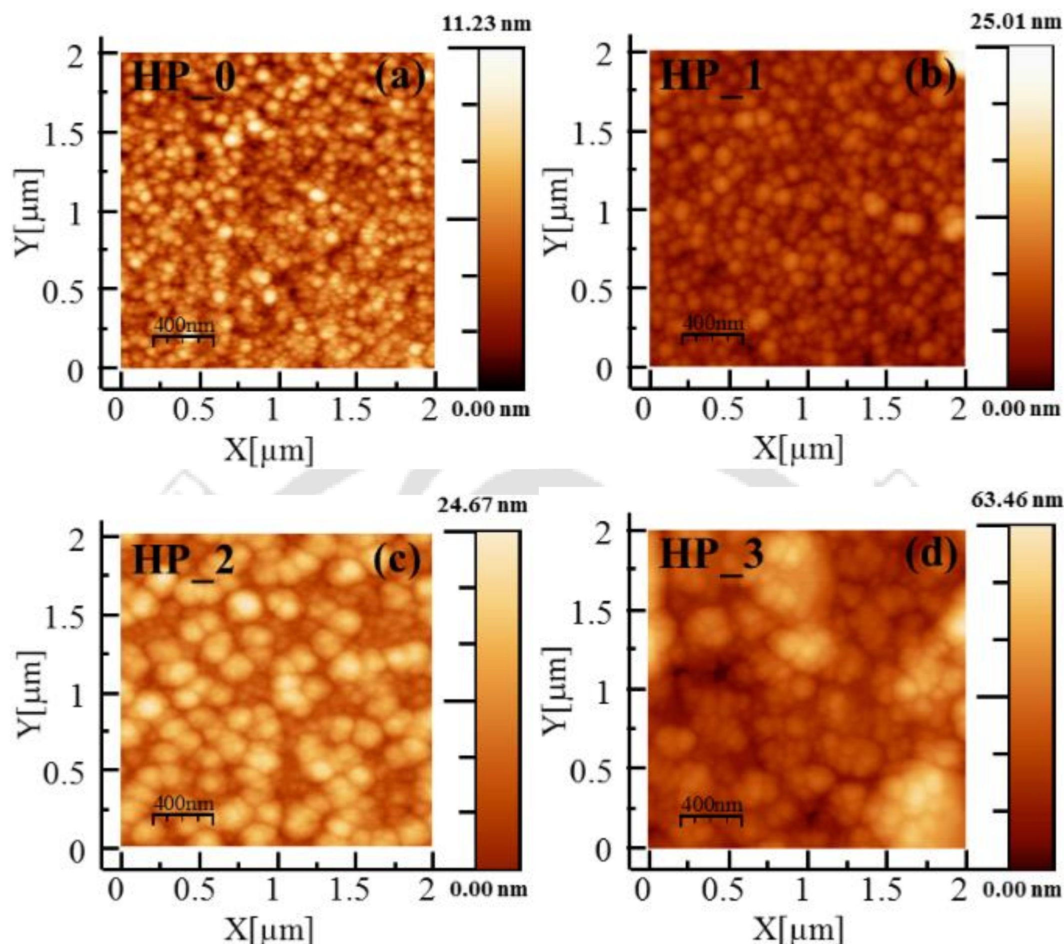

Fig. 3.18 (a-d). Surface morphology of *HP_0 - HP_3* films measured from AFM measurements.

3.2.7. Electrical conductivity

The dark (σ_d) and photo (σ_{ph}) conductivity of films deposited on corning substrate were measured in a coplanar geometry using 100 W halogen lamp at incident power density of 100 mW/cm^2 (Eq. 2.22). The dark and photoconductivity of these films at 300 K are shown in Fig. 3.18. All the films show about 4 orders of magnitude change in conductivity under illumination. The temperature dependence of the conductivity for these films is shown in Fig. 3.19. At room temperature, both dark and photoconductivity are found to be nearly same for all the films. The films have good photosensitivity at 475 K also, with highest value for *HP_1* which can be attributed to the improvement in structural ordering of this films after one step HPT, while films being still amorphous in nature. With increased number of HPT steps, though the structural ordering is improved, however nanocrystalline phase also develops, which lowers the photosensitivity at higher temperature as compared to one step HPT. The estimated

TH-2097_126121019

activation energy (E_A) in the range of 370-430 K (Eq. 2.23) of films obtained from cooling data of dark conductivity is 0.49, 0.50, 0.56 and 0.62 eV correspond to *HP_0* to *HP_3* films respectively.

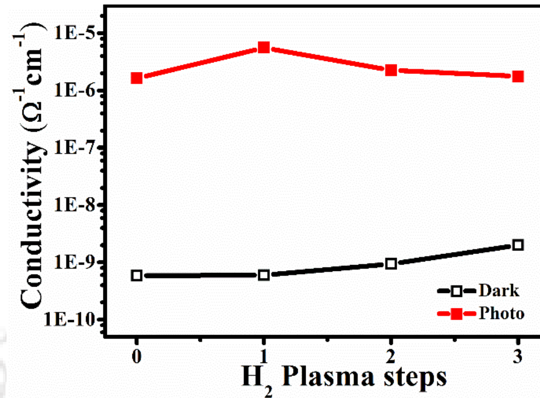

Fig. 3.19. Room temperature conductivity of films as a function of number of H_2 plasma steps.

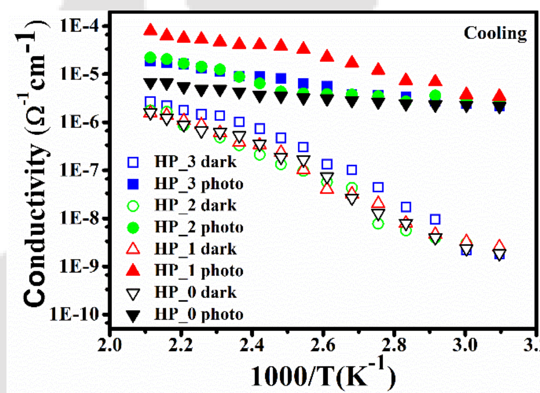

Fig. 3.20. The dark and photo conductivity of *HP_0* to *HP_3* films as a function of temperature.

This is for the first time, when thin a-Si:H films with improved microstructure are deposited using the hydrogen plasma treatment followed by subsequent silane plasma. In the work reported in literature, no subsequent silane plasma was introduced to deposit the a-Si:H films on hydrogen plasma treated surface. In order to achieve nc-Si:H films, most of researchers deposited thin a-Si:H films and subjected it to HPT followed by high temperature annealing [18,20,43]. Pangal et.al reported that the HPT had created seed nuclei of microcrystalline silicon. These seed nuclei enhanced the overall crystallization rate[18].

3.3. Conclusion

Thick nc-Si:H films were deposited with intermittent H_2 plasma treatment during the deposition of a-Si:H films in continuous process, with a small time gap between the two steps,

TH-2097_126121019

silane plasma and hydrogen plasma. The influence of hydrogen plasma treatment on the microstructure of a-Si:H films is studied. It is observed that exposure to hydrogen plasma during deposition of a-Si:H films improves the microstructure of the films by etching the amorphous phase and replacing the weak Si-Si bonds and Si-H_2 bonds by strong Si-H bonds. We observed that microstructure factor is directly related to void fraction in the films and also to the amplitude of the imaginary part of pseudo dielectric function. The single TL model could not give accurate results in case of mixed phase films and TL+Gauss model has been used to calculate the optical constants, thickness and band gap of the those mixed phase films. Further, results obtained from the TL+Gauss model have been compared with those obtained using TL+BEMA for accuracy of the model. These estimated optical constants, thickness and band gap of the films match well with those obtained from the analysis of UV-Vis-NIR Transmission data. Further the void, amorphous and crystalline volume fractions and surface roughness of the films from BEMA model values are well correlated with those obtained from FTIR, Raman and AFM measurements results. The overall deposition rate of these nc-Si films is higher without any annealing than that obtained by hydrogen dilution of silane for similar films. Process of H_2 plasma treatment of a-Si:H films is used to fabricate stable c-Si/a-Si:H solar cells presented in Chapter 6 and Chapter 7 and also to increase the efficiency of c-Si/a-Si:H heterojunction solar cells by reducing the interface defects and improving the passivation of coordination defects.

3.4. References

[1] S. De Wolf, A. Descoeudres, Z.C. Holman, C. Ballif, High-efficiency Silicon Heterojunction Solar Cells: A Review, Green. 2 (2012) 7–24. doi:10.1515/green-2011-0018.

[2] M. Taguchi, A. Yano, S. Tohoda, K. Matsuyama, Y. Nakamura, T. Nishiwaki, K. Fujita, E. Maruyama, 24.7% Record efficiency HIT solar cell on thin silicon wafer, IEEE J. Photovoltaics. 4 (2014) 96–99. doi:10.1109/JPHOTOV.2013.2282737.

[3] M.R. Page, E. Iwaniczko, Y. Xu, L. Roybal, F. Hasoon, Q. Wang, R.S. Crandall, Amorphous / crystalline silicon heterojunction solar cells with varying i-layer thickness, Thin Solid Films. 519 (2011) 4527–4530. doi:10.1016/j.tsf.2011.01.293.

[4] Jason T. Drotar, Y.P.Zhao, T.M.Lu, and G.C.Wang, Surface roughening in low-pressure chemical vapor deposition, Phys. Rev. B. 64 (2001) 125411.

[5] R. Goswami, S. Ray, Structural studies on Si:H network before and after solid phase crystallization using spectroscopic ellipsometry: Correlation with Raman spectroscopy

TH-2097_126121019

and transmission electron microscopy, Appl. Surf. Sci. 282 (2013) 615–623. doi:10.1016/j.apsusc.2013.06.021.

[6] S. Toko, Y. Torigoe, W. Chen, D. Yamashita, H. Seo, N. Itagaki, K. Koga, M. Shiratani, Effects of cluster incorporation into hydrogenated amorphous silicon films in initial discharge phase on film stability, Thin Solid Films. 587 (2015) 126–131. doi:10.1016/j.tsf.2015.02.052.

[7] D. Beeman, R. Tsu, M. Thorpe, Structural information from the Raman spectrum of amorphous silicon, Phys. Rev. B. 32 (1985) 874–878. doi:10.1103/PhysRevB.32.874.

[8] M.H. Brodsky, M. Cardona, J.J. Cuomo, Infrared and Raman spectra of the silicon-hydrogen bonds in amorphous silicon prepared by glow discharge and sputtering, Phys. Rev. B. 16 (1977) 3556–3571. doi:10.1103/PhysRevB.16.3556.

[9] R. Tsu, J. Gonzalez-Hernandez, F.H. Pollak, Determination of the energy barrier for structural relaxation in amorphous Si and Ge by Raman scattering, Solid State Commun. 54 (1985) 447–450. doi:10.1016/0038-1098(85)90947-0.

[10] J. He, C. Wang, W. Li, K.C. Qi, Y.D. Jiang, Effect of gas temperature on the structural and optoelectronic properties of a-Si:H thin films deposited by PECVD, Surf. Coat. Technol. 214 (2013) 131–137. doi:10.1016/j.surfcoat.2012.11.014.

[11] M. Marinov, N. Zotov, Model investigation of the Raman spectra of amorphous silicon, Phys. Rev. B. 55 (1997) 2938–2944. doi:10.1103/PhysRevB.55.2938.

[12] S. Veprek, F.A. Sarott, Z. Iqbal, Effect of grain boundaries on the Raman spectra, optical absorption, and elastic light scattering in nanometer-sized crystalline silicon, Phys. Rev. B. 36 (1987) 3344–3350. doi:10.1103/PhysRevB.36.3344.

[13] P. Gogoi, H.S. Jha, P. Agarwal, High band gap nanocrystallite embedded amorphous silicon prepared by hotwire chemical vapour deposition, Thin Solid Films. 518 (2010) 6818–6828. doi:10.1016/j.tsf.2010.06.040.

[14] Purabi Gogoi, Pratima Agarwal, Structural and optical studies on hot wire chemical vapour deposited hydrogenated silicon films at low substrate temperature, Sol. Energy Mater. Sol. Cells. 93 (2009) 199–205. doi:10.1016/j.solmat.2008.09.058.

[15] Ramakrishna Madaka,Venkanna Kanneboina, Pratima Agarwal, Evolution of nanostructure in hydrogenated amorphous silicon thin films with substrate temperature studied by Raman mapping, Raman scattering and spectroscopic ellipsometry, J. Mater. Sci. Mater. Electron. 28 (2017) 8885–8894. doi:10.1007/s10854-017-6618-y.

[16] M. Mews, E. Conrad, S. Kirner, N. Mingirulli, L. Korte, Hydrogen plasma treatments of amorphous/crystalline silicon Heterojunctions, Energy Procedia. 55 (2014) 827–833. doi:10.1016/j.egypro.2014.08.066.

[17] M. Mews, T.F. Schulze, N. Mingirulli, L. Korte, Hydrogen plasma treatments for

TH-2097_126121019

passivation of amorphous-crystalline silicon-heterojunctions on surfaces promoting epitaxy, Appl. Phys. Lett. 102 (2013) 2011–2015. doi:10.1063/1.4798292.

[18] K. Pangal, J.C. Sturm, S. Wagner, T.H. Büyüklimanli, Hydrogen plasma enhanced crystallization of hyrdogenated amorphous silicon films, J. Appl. Phys. 85 (1999) 1900–1906. doi:10.1063/1.369182.

[19] K. Saitoh, M. Kondo, M. Fukawa, T. Nishimiya, A. Matsuda, Role of the hydrogen plasma treatment in layer-by-layer deposition of microcrystalline silicon, Appl. Phys. Lett. 71 (1997) 3403–3405. doi:10.1063/1.120324.

[20] J. Shi, M. Boccard, Z. Holman, Plasma-initiated rehydrogenation of amorphous silicon to increase the temperature processing window of silicon heterojunction solar cells, Appl. Phys. Lett. 109 (2016) 031601. doi:10.1063/1.4958831.

[21] R. Swanepoel, Determination of the thickness and optical constants of amorphous silicon, J. Phys. E. 16 (2000) 1214–1222. doi:10.1088/0022-3735/16/12/023.

[22] J. Tauc, A. Menth, States in the gap, J. Non. Cryst. Solids. 8–10 (1972) 569–585. doi:10.1016/0022-3093(72)90194-9.

[23] A. Hadjadj, N. Pham, P. Roca I Cabarrocas, O. Jbara, G. Djellouli, Ellipsometry investigation of the amorphous-to-microcrystalline transition in a-Si:H under hydrogen-plasma treatment, J. Appl. Phys. 107 (2010) 083509. doi:10.1063/1.3393273.

[24] R.W. Collins, A.S. Ferlauto, G.M. Ferreira, C. Chen, J. Koh, R.J. Koval, Y. Lee, J.M. Pearce, C.R. Wronski, Evolution of microstructure and phase in amorphous, protocrystalline, and microcrystalline silicon studied by real time spectroscopic ellipsometry, Sol. Energy Mater. Sol. Cells. 78 (2003) 143–180. doi:10.1016/S0927-0248(02)00436-1.

[25] A. Fontcuberta i Morral and P. Roca i Cabarrocas, C.Clerc, Structure and hydrogen content of polymorphous silicon thin films studied by spectroscopic ellipsometry and nuclear measurements, Phys. Rev. B. 69 (2004) 125307. doi:10.1103/PhysRevB.69.125307.

[26] Yen-Ho Chu,Chien-Chieh Lee, I.-C.C. Shan-Yuan Chang, Jenq-Yang Chang, Tomi Li, Investigation of hydrogenated amorphous silicon as passivation layer by high density plasma, Thin Solid Films. 570 (2014) 591–594. doi:10.1016/j.tsf.2014.03.064.

[27] T. Yuguchi, Y. Kanie, N. Matsuki, H. Fujiwara, Complete parameterization of the dielectric function of microcrystalline silicon fabricated by plasma-enhanced chemical vapor deposition, J. Appl. Phys. 111 (2012) 083509. doi:10.1063/1.4704158.

[28] S. Kageyama, M. Akagawa, H. Fujiwara, Dielectric function of a-Si:H based on local network structures, Phys. Rev. B. 83 (2011) 195205. doi:10.1103/PhysRevB.83.195205.

[29] H. Fujiwara, M. Kondo, A. Matsuda, Real-time spectroscopic ellipsometry studies of

TH-2097_126121019

the nucleation and grain growth processes in microcrystalline silicon thin films, Phys. Rev. B. 63 (2001) 115306. doi:10.1103/PhysRevB.63.115306.

[30] H. Fujiwara, Spectroscopic Ellipsometry Principles and Applications, Willey Publ. (2007). doi:10.1002/9780470060193,ISBN:9780470016084.

[31] Akihisa Matsuda, Microcrystalline silicon. Growth and application, J. Non. Cryst. Solids. 338–340 (2004) 1–12. doi:10.1016/j.jnoncrysol.2004.02.012.

[32] G.E.Jellison and F.A. Modine, Parameterization of the optical functions of amorphous materials in the interband region, Appl. Phys. Lett. 69 (1996) 371–373. doi:10.1063/1.118064.

[33] A.S. Ferlauto, G.M. Ferreira, J.M. Pearce, C.R. Wronski, C.D. Ganguly, Analytical model for the optical functions of amorphous semiconductors from the near- infrared to ultraviolet : Applications in thin film photovoltaics, J. Appl. Phys. 92 (2002) 2424. doi:10.1063/1.1497462.

[34] A.R. Forouhi, I. Bloomer, Optical dispersion relations for amorphous semiconductors and amorphous dielectrics, Phys. Rev. B. 34 (1986) 7018–7026. doi:10.1103/PhysRevB.34.7018.

[35] Y. Liu, G. Xu, C. Song, W. Weng, P. Du, G. Han, Modification on Forouhi and Bloomer model for the optical properties of amorphous silicon thin films, Thin Solid Films. 515 (2007) 3910–3913. doi:10.1016/j.tsf.2006.11.003.

[36] G.E.Jellison and F.A. Modine, Parameterization of the optical functions of amorphous materials in the interband region, Appl. Phys. Lett. 69 (1996) 371–373. doi:10.1063/1.118064.

[37] D.E. Aspnes, Optical properties of thin films, Thin Solid Films. 89 (1982) 249–262. doi:10.1016/0040-6090(82)90590-9.

[38] H. Zhang, X. Zhang, C. Wei, J. Sun, X. Geng, S. Xiong, Y. Zhao, Microstructure characterization of microcrystalline silicon thin films deposited by very high frequency plasma-enhanced chemical vapor deposition by spectroscopic ellipsometry, Thin Solid Films. 520 (2011) 861–865. doi:10.1016/j.tsf.2011.04.166.

[39] S. Hazra, I. Sakata, M. Yamanaka, E. Suzuki, Evolution of an amorphous silicon network from silicon paracrystallites studied by spectroscopic ellipsometry, Phys. Rev. B. 69 (2004) 235204. doi:10.1103/PhysRevB.69.235204.

[40] R.A.Street, Hydrogenated amorphous silicon, Cambridge Solid State Ser. (1991). doi:10.1017/CBO9780511525247,ISBN:9780521371568.

[41] F.I. Morral, P. Roca i Cabarrocas, Etching and hydrogen diffusion mechanisms during a hydrogen plasma treatment of silicon thin films, J. Non. Cryst. Solids. 299–302 (2002) 196–200. doi:10.1016/S0022-3093(01)01001-8.

TH-2097_126121019

[42] K.L. M.Fehr, A. Schnegg, B. Rech, O. Astakhov, F. Finger, R. Bittl, C. Teutloff, Metastable Defect Formation at Microvoids Identified as a Source of Light-Induced Degradation in a-Si:H, Phys. Rev. Lett. 112 (2014) 066403. doi:10.1103/PhysRevLett.112.066403.

[43] A.N. Nazarov, V.S. Lysenko, T.M. Nazarova, Hydrogen plasma treatment of silicon thin-film structures and nanostructured layers, Semicond. Physics, Quantum Electron. Optoelectron. 11 (2008) 101–123.

TH-2097_126121019

Chapter 4

Influence of Hydrogen Flow Rate on Microstructural and Optical Properties of a-Si:H(p) and a-Si:H(n) Thin Films

This chapter presents influence of hydrogen flow rate on the microstructure and optical properties of boron and phosphorous doped hydrogenated amorphous silicon (a-Si:H(p) and a-Si:H(n)) films. The quality of a-Si:H(p) and a-Si:H(n) layer is very crucial to improve the performance of c-Si/a-Si:H heterojunction solar cells, which have demonstrated very promising performance [1–4]. The essential requirements for the p and n-layer in silicon based heterojunction solar cells are high conductivity and wide bandgap [5]. The high conductivity reduces the series resistance between the p/n-layer and the transparent conducting oxide (TCO) layer, while a wide bandgap allows more sunlight transmitting through the p/n-layer and being absorbed by the c-Si respectively [5,6]. This can be achieved by tuning the deposition parameters, such as hydrogen flow rate, substrate temperature and rf power. With this motivation, a series of a-Si:H(p) and a-Si:H(n) films were deposited using RFPECVD technique by varying the hydrogen flow rate in the range of 30-70 SCCM and 30-80 SCCM respectively. The SE measurements have been performed on these films to study microstructure, thickness, optical bandgap and volume fractions (void, amorphous and crystalline) and also surface roughness. Further these results were compared with UV-Vis-NIR and AFM measurements.

4.1. Experimental details

Boron doped hydrogenated amorphous silicon (a-Si:H(p)) thin films were deposited on corning 1737 glass substrate at hydrogen flow rate (HFR) of 30 to 70 SCCM using RFPECVD in multichamber system with diborane (B_2H_6) (2% of B_2H_6 diluted in H_2) flow rate of 6 SCCM, pure silane (SiH_4) flow rate of 4 SCCM, RF power of 30 W, process pressure of 0.42 mbar and deposition temperature of 200 ºC. For phosphorous doped hydrogenated amorphous silicon (a-Si:H(n)) films, phosphine (PH_3) (1% of PH_3 diluted in H_2) flow rate (PFR) was fixed at 6 SCCM, hydrogen flow rate was varied from 30-80 SCCM and other parameters were maintained same as those for p-layer. The films labelled as *MP120-MP124* and *MN87-MN92*

TH-2097_126121019

correspond to a-Si:H(p) with HFR of 30-70 SCCM and a-Si:H(n) with HFR of 30-80 SCCM respectively.

The a-Si:H(p) and a-Si:H(n) thin films deposited on corning 1737 glass were characterised by Ex-situ SE techniques in the photon energy range of 2-5.5 eV and 70° of incident angle. SEA software is used to analyse the data of films. The UV-Vis-NIR spectrometer is used to record the transmission spectra of the p and n- thin films in the wavelength range of 200 to 2500 nm and the optical band gap of the films is estimated from this transmission data. The surface morphology of a-Si:H(p) and a-Si:H(n)) thin films was studied by atomic force microscopy.

4.2. Results and discussion

4.2.1. Influence of hydrogen flow rate on a-Si:H(p) films

4.2.1.1. SE studies

Fig. 4.1 (a, b) show the measured spectra of real ($< \varepsilon_1 >$) and imaginary ($< \varepsilon_2 >$) part of pseudo dielectric function (Eq. 2.7) of a-Si:H(p) films deposited with different HFR and also c-Si substrate (normalized by a factor of two) as a function of photon energy. The intense peak around 2 eV is due to interference of reflected light from the different interfaces and surface of film [7]. The position of this peak in $< \varepsilon_1 >$ and $< \varepsilon_2 >$ spectra has shifted from 2 to 2.5 eV with increase in hydrogen flow rate of a-Si:H(p) films. This indicates a change in thickness of the films with variation in hydrogen flow rate. In case of c-Si, the peak and dip in $< \varepsilon_1 >$ and two peaks in $< \varepsilon_2 >$ spectra at 3.4 eV and 4.2 eV correspond to direct band to band transition [8]. Similar features have also been reported for nc-Si:H and μc-Si:H films [9,10] and a-Si:H films in Chapter 3.

The $< \varepsilon_2 >$ spectra of *MP120-MP122* films deposited at lower HFR show broad peak at 3.6 eV and which shifts to 3.9 eV in case of *MP123* and *MP124* films deposited at higher hydrogen dilution. The magnitude of $< \varepsilon_1 >$ and $< \varepsilon_2 >$ is highest for *MP123* film. The broad peak around 3.6 eV corresponds to direct band to band transitions in the a-Si:H films [7,11,12]. Presence of this peak confirms that p-layer is amorphous in nature. For films deposited with higher H_2 flow rate (*MP123* and *MP124*), the broad peak shift from 3.6 to 3.99 eV with signature of a shoulder peak at 3.4 eV. This is an indication of change in microstructure of the films from pure amorphous phase to that near the onset of nanocrystalline phase [7,13–16]. A systematic increase in the amplitude of $< \varepsilon_2 >$ spectra is also observed from *MP120* to *MP123* films, which decreases for *MP124* film. The amplitude of $< \varepsilon_2 >$ spectra represents the film

TH-2097_126121019

density, void fraction in films and also type of bonding configuration such as Si-H, Si-H_2 and Si-H_n in a-Si:H network [8]. A decrease in broadening accompanied by a higher amplitude in these spectra suggests an improvement in density and decrease in disorder in the a-Si:H(p) films deposited at higher H_2 flow rate or higher H_2 dilution.

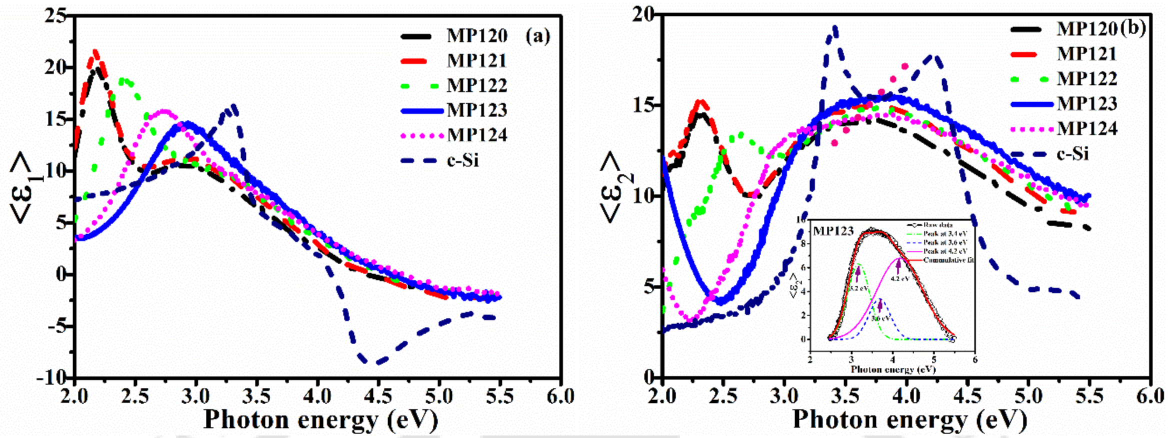

Fig. 4.1. a) Real ($<\varepsilon_1>$) and b) Imaginary ($<\varepsilon_2>$) part of pseudo dielectric function measured as a function of photon energy of a-Si:H(p) films along with c-Si substrate. In case of c-Si, the spectra are normalised by a factor of two to fit in the range.

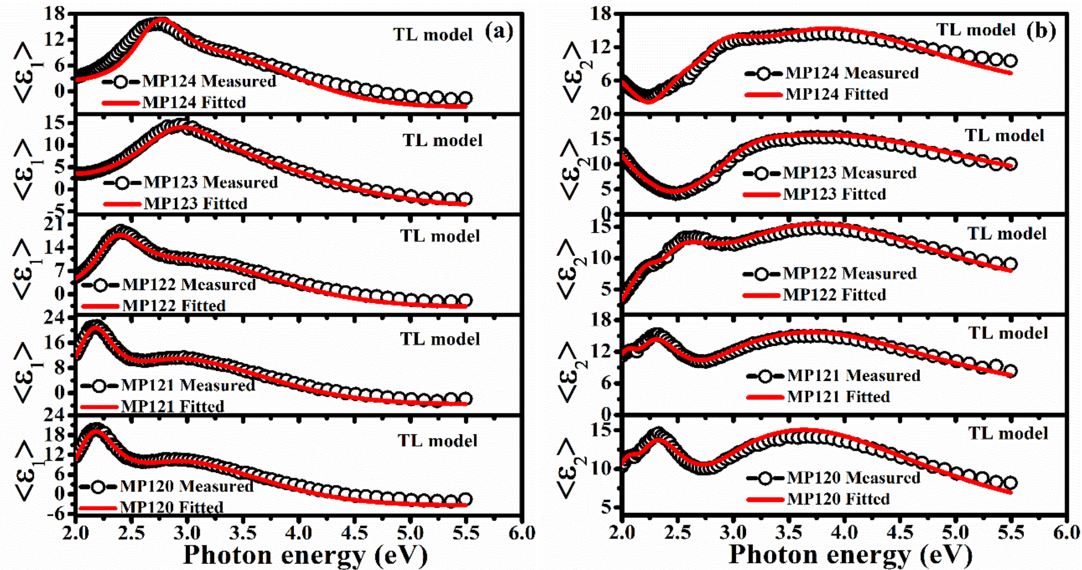

Fig. 4.2. (a, b). Measured and fitted (TL model) values of real ($<\varepsilon_1>$) and imaginary ($<\varepsilon_2>$) part of pseudo dielectric function of a-Si:H(p) films as a function of photon energy.

The Tauc-Lorentz (TL) model has been applied to calculate the thickness and optical bandgap of a-Si:H(p) films as described in section 2.2.3.1, Chapter 2 (Eq. 2.9 and Eq. 2.10) [7,11,12]. We have used two-layer structure (*substrate / bulk layer/surface roughness layer/air*) to determine the thickness, optical band gap and also volume fractions of void, amorphous and crystalline and surface roughness of a-Si:H(p) films as described in section 2.2.3, Chapter 2.

Fig. 4.2(a, b) show the measured and fitted (TL model) values of real ($< \varepsilon_1 >$) and imaginary ($< \varepsilon_2 >$) part of pseudo dielectric function of a-Si:H(p) films as a function of photon energy. Estimated thickness and optical band gap values are listed in Table 4.1. The quality of fitting (goodness of fitting) (R^2) is 99% and estimated errors are included in corresponding figures.

Table 4.1. TL model fitted parameters (A, E_0, C and E_g) and estimated thickness of a-Si:H(p) films.

Sample	HFR (SCCM)	Thickness (nm)	A (eV)	E_0 (eV)	C (eV)	E_g (eV)	d_s (nm)	E_g(eV) (UV-Vis-NIR)
MP120	30	105	176	3.65	2.99	1.82	2.09	1.81
MP121	40	105	193	3.75	2.90	1.82	1.82	1.82
MP122	50	92	194	3.72	2.85	1.84	1.11	1.83
MP123	60	74	210	3.99	2.67	1.85	1.50	1.85
MP124	70	67	186	4.10	2.79	1.87	2.16	1.87

Fig. 4.3 shows the TL model fitted parameters of a-Si:H(p) films as a function of hydrogen flow rate. Amplitude parameter (A) increases whereas the broadening parameter (C) decreases, with increase in the hydrogen flow rate for a-Si:H(p) film except *MP124* film. The main reason for this change is that large flux of atomic hydrogen has passivated co-ordination defects and decreased the band tail states in a-Si:H network. The atomic hydrogen also diffused deeper in to the film and replaced weak Si-Si and Si-H_2 bonds with strong Si-Si and Si-H bonds thus increased the density of the films and also improved the microstructure [12,16,17]. For *MP124* film, the value of A has decreased and C has increased. At HFR of 70 SCCM, hydrogen concentration in the chamber is considerably increased and hydrogen precursors made number of collisions with neighbouring H_2 and SiH_4 molecules, which resulted in an increase in defect density, bond density of Si-H_2 and void fraction in the films.

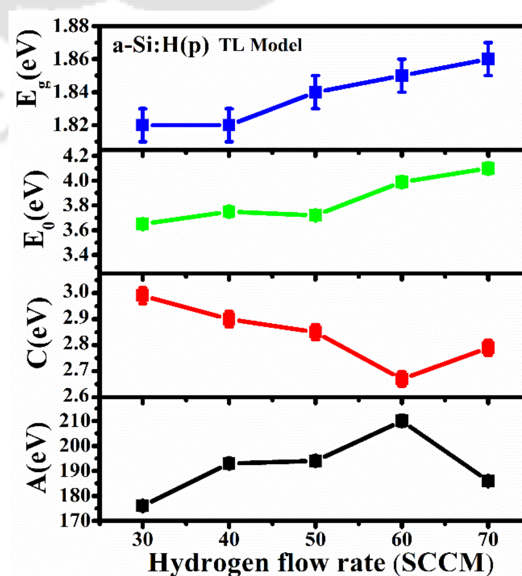

Fig. 4.3. TL model fitted parameters (A, E_0, C and E_g) of a-Si:H(p) film as a function of HFR.

TH-2097_126121019

In order to estimate the amorphous, crystalline and void fraction in the films, BEMA model was used as described in section 2.2.3.2, Chapter 2 (Eq. 2.11) [7,18–20]. Fig. 4.4 show measured and fitted spectra of real ($< \varepsilon_1 >$) and imaginary ($< \varepsilon_2 >$) part of pseudo dielectric function of a-Si:H(p) films as a function of photon energy. Estimated volume fractions and surface roughness of films are given in Table 4.2.

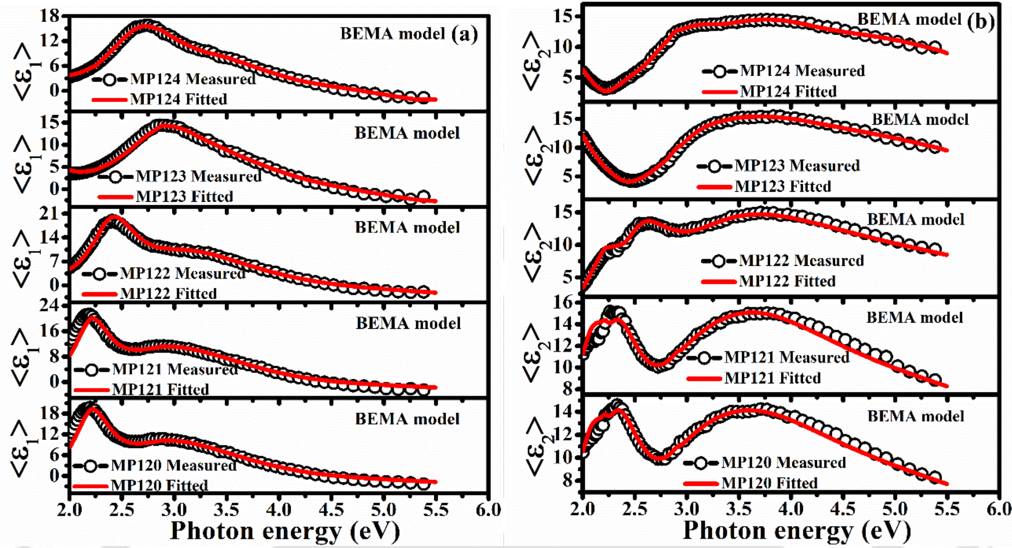

Fig. 4.4(a, b). Measured and fitted (BEMA model) values of $< \varepsilon_1 >$ and $< \varepsilon_2 >$ of a-Si:H(p) films as a function of photon energy.

Table 4.2. The estimated void (f_v), amorphous (f_a) and crystalline (f_c) volume fractions, thickness and surface roughness (d_s) of a-Si:H(p) films.

Sample	HFR (SCCM)	Thickness (nm)	f_v (%)	f_a (%)	f_c (%)	d_s (nm)	d_{RMS} (nm) (AFM)
MP120	30	111	15.42	83.50	1.05	1.23	1.10
MP121	40	101	14.85	84.10	1.05	1.56	1.27
MP122	50	93	9.16	87.80	3.02	2.19	1.89
MP123	60	73	7.14	84.35	8.50	2.46	2.12
MP124	70	67	13.22	74.40	12.37	3.19	3.11

Fig. 4.5 shows the estimated void (f_v), amorphous (f_a) and crystalline (f_c) volume fractions of a-Si:H(p) films as a function of hydrogen flow rate. It is observed that void fraction has decreased up to 60 SCCM of HFR and then increased at 70 SCCM of HFR. The least void fraction of 7.14% was observed at 60 SCCM of HFR (*MP123*), whereas crystalline fraction has continuously increased. The maximum crystalline fraction of 12.37% was observed at 70 SCCM of HFR. The amorphous fraction has increased up to 50 SCCM of HFR and then decreased with further increase in HFR. The surface roughness of the films is found to increase from 1 to 3 nm with increase in HFR due to increased ion bombardment on growing surface of the films.

TH-2097_126121019

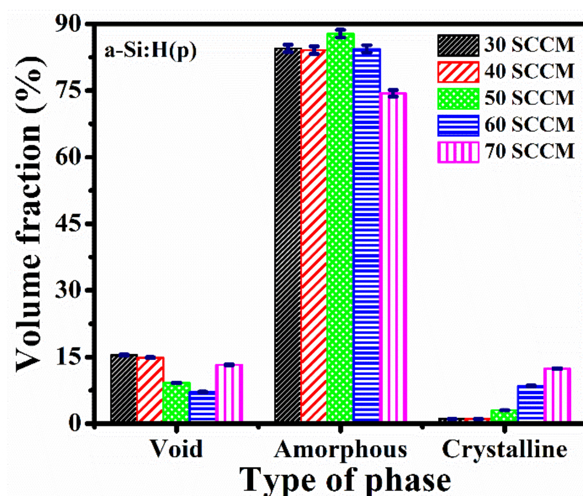

Fig. 4.5. Void, amorphous and crystalline volume fractions of a-Si:H(p) film corresponding to HFR.

4.2.1.2. UV-Vis-NIR studies

Fig. 4.6 shows the UV-Vis-NIR transmission spectra of *MP120-MP124* films. In Fig. 4.6, a clear shift in absorption edge of transmission spectra of films, towards higher energy is observed with increase in HFR. The optical band gap of the films was calculated using Tauc's plot (Eq. 2.21) [21,22] and the values are listed in Table 4.1. These values are in good agreement with those estimated from SE analysis. It is observed that thickness of the films has decreased and band gap has increased with increase in hydrogen flow rate during deposition.

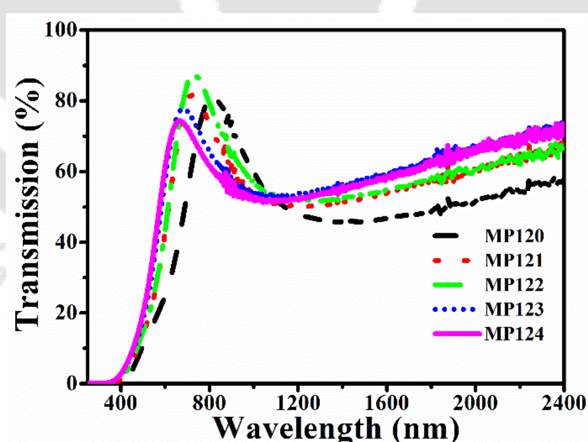

Fig. 4.6. Transmission spectra of a-Si:H(p) thin films.

4.2.1.3. AFM morphology studies

Fig. 4.7(a-e) show the AFM surface morphology of *MP120-MP123* thin films. It is observed that all the films are uniform throughout the sample and voids are formed in films at lower HFR. The RMS surface roughness (d_{RMS}) values are found to be 1.1 to 3.1 nm corresponding to *MP120-MP123* films respectively and listed in Table 4.2. The roughness of the films from

TH-2097_126121019

the AFM measurements is comparable with the estimated surface roughness of the films from SE measurements.

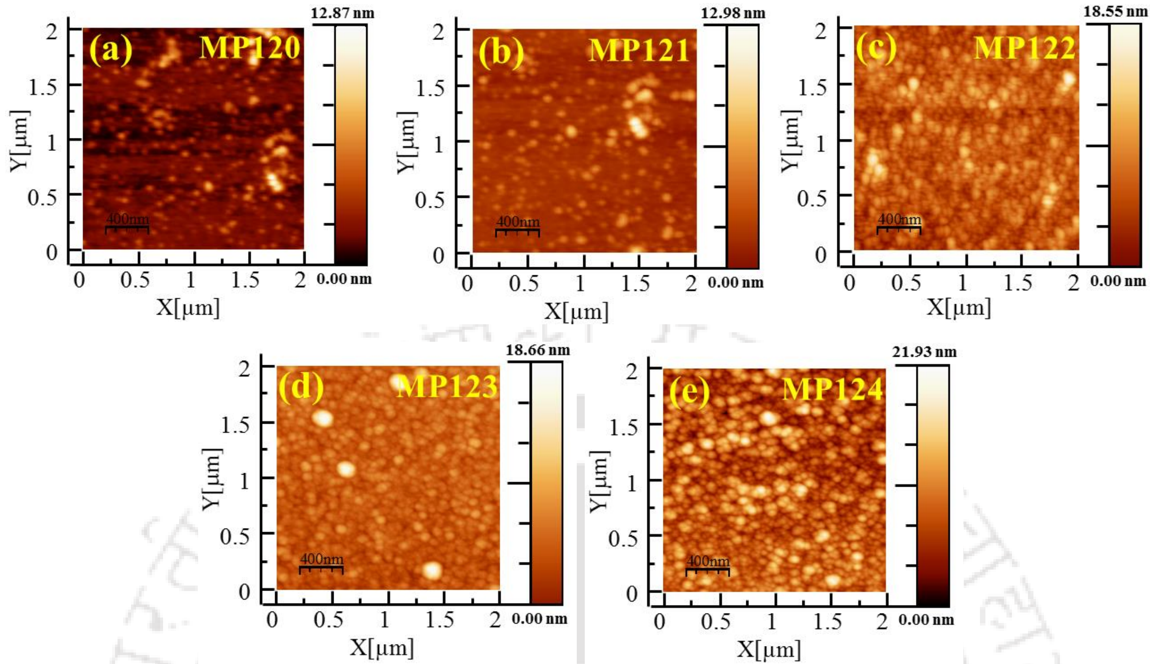

Fig. 4.7(a-e). AFM surface morphology of *MP120-MP124* films.

4.2.2. Influence of hydrogen flow rate on a-Si:H(n) films

4.2.2.1. SE studies

Fig. 4.8 (a, b) show the measured spectra of real ($< \varepsilon_1 >$) and imaginary ($< \varepsilon_2 >$) part of pseudo dielectric function (Eq. 2.7) of a-Si:H(n) films and also c-Si as a function of photon energy. The intense peak around 2 eV corresponds to interference of reflected light from the interface and surface of film and its position depends upon the thickness and refractive index of the films. The interference peak position in $< \varepsilon_1 >$ and $< \varepsilon_2 >$ spectra has shifted from 2 to 2.5 eV with increase in HFR of a-Si:H(n) films. This indicates a change in thickness of the films with variation of HFR.

The $< \varepsilon_2 >$ spectra of *MN87-MN89* (HFR of 30-50 SCCM) films show broad peak at 3.6 eV corresponding to direct band to band transitions in the a-Si:H films [7,11,12] and this peak is shifted to 3.7 eV for *MN90* (60 SCCM) film. For films deposited at HFR of 70 and 80 SCCM (*MN91* and *MN92*), the broad peak is further shifted to 3.9 and 4.1 eV with signature of a shoulder peak at 3.4 eV respectively. This is an indication of change in microstructure of the films from pure amorphous phase to that near the onset of nanocrystalline phase [7,13–16]. In case of *MN91* and *MN92,* the peak at 4.2 eV was integrated with more dominating peak at 2.5

TH-2097_126121019

eV (interference fringe due to thickness of films). A systematic increase in the amplitude of $< \varepsilon_2 >$ spectra is also observed from *MN87-MN91* films, which has decreased for *MN92* film. The magnitude of $< \varepsilon_1 >$ and $< \varepsilon_2 >$ is highest for *MN91* film. A decrease in broadening along with higher amplitude in these $< \varepsilon_1 >$ and $< \varepsilon_2 >$ spectra suggests decrease in disorder and an improvement in density of the a-Si:H(n) films deposited at higher H_2 flow rate.

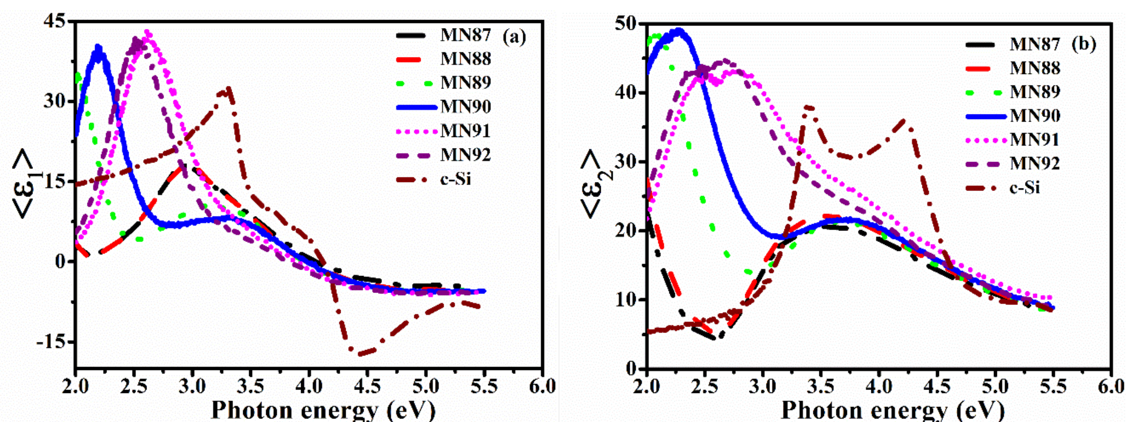

Fig. 4.8. a) Real ($< \varepsilon_1 >$) and b) Imaginary ($< \varepsilon_2 >$) part of pseudo dielectric function measured as a function of photon energy for a-Si:H(n) films along with c-Si substrate.

The thickness and optical bandgap of a-Si:H(n) films were estimated by TL model [7,11,12] using two-layer model structure similar to that used for a-Si:H(p) films. Fig. 4.9(a, b) show the measured and fitted (TL model) values of real ($< \varepsilon_1 >$) and imaginary ($< \varepsilon_2 >$) part of pseudo dielectric function of a-Si:H(n) films as a function of photon energy. Estimated thickness and optical band gap values are listed in Table 4.3. The quality of fitting (goodness of fitting) (R^2) is 99% and estimated errors are included in corresponding figures.

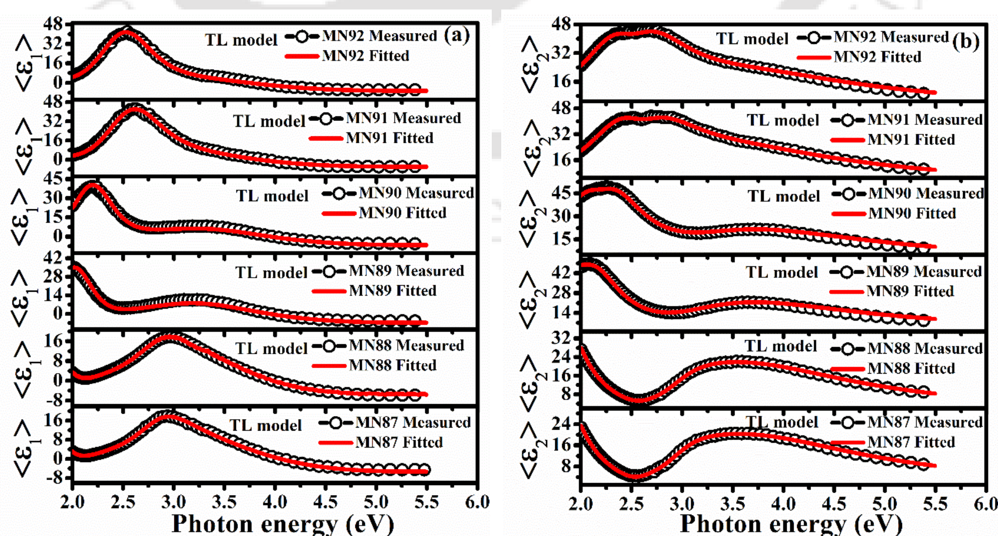

Fig. 4.9(a, b): Measured and fitted (TL model) values of $< \varepsilon_1 >$ and $< \varepsilon_2 >$ of a-Si:H(n) films as a function of photon energy.

TH-2097_126121019

Table 4.3. TL model fitted parameters (A, E_0, C and E_g) and estimated thickness of a-Si:H(n) films.

Sample	HFR (SCCM)	Thickness (nm)	A (eV)	E_0 (eV)	C (eV)	E_g (eV)	d_s (nm)	E_g(eV) (UV-Vis-NIR)
MN87	30	109	225	3.50	2.87	1.80	1.76	1.81
MN88	40	98	225	3.54	2.78	1.81	1.82	1.82
MN89	50	75	227	3.61	2.75	1.84	1.33	1.83
MN90	60	67	232	3.70	2.67	1.85	1.50	1.85
MN91	70	62	247	3.94	2.55	1.86	1.35	1.87
MN92	80	53	245	4.11	2.80	1.86	1.54	1.87

Fig. 4.10 shows the TL model fitted parameters of a-Si:H(n) films as a function of hydrogen flow rate. Amplitude parameter A has increased and broadening factor C has decreased with increase in the HFR of a-Si:H(n) film except for *MN92* film. For *MN92* (80 SCCM) film, the value of A has slightly decreased and C value has increased. At HFR of 80 SCCM, hydrogen concentration in the chamber is considerably high, thus hydrogen makes frequent collisions with neighbouring precursors. As a result, some of growth precursors may not be able to reach to surface as well bulk of the films and also do not occupy stable position on growing surface. This leads to increase in defect density, bond density of Si-H_2 (formation of higher hydride) and void fraction in the films, when HFR is very high (80 SCCM).

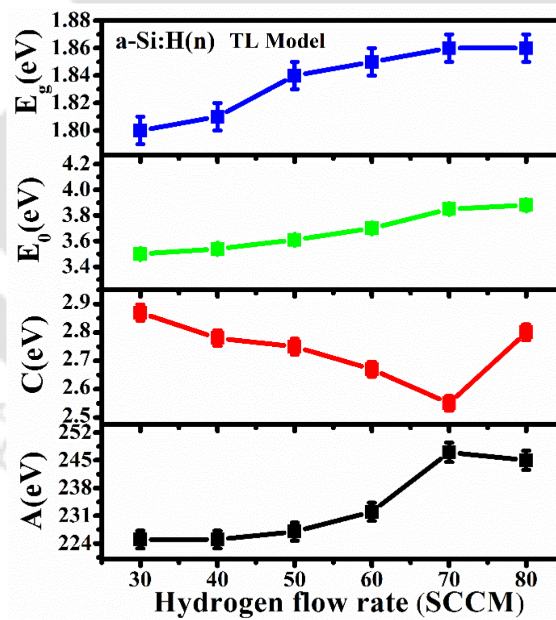

Fig. 4.10. TL model fitted parameters (A, E_0, C and E_g) of a-Si:H(n) film as a function of HFR.

BEMA model was used to estimate the amorphous, crystalline and void volume fraction in the films as described in section 2.2.3.2, Chapter 2 (Eq. 2.11) [7,18–20]. Fig. 4.11(a, b) show measured and fitted (BEMA model) spectra of real ($<\varepsilon_1>$) and imaginary ($<\varepsilon_2>$) part of pseudo dielectric function of a-Si:H(n) films as a function of photon energy. Estimated volume fractions and surface roughness of films are given in the Table 4.4.

TH-2097_126121019

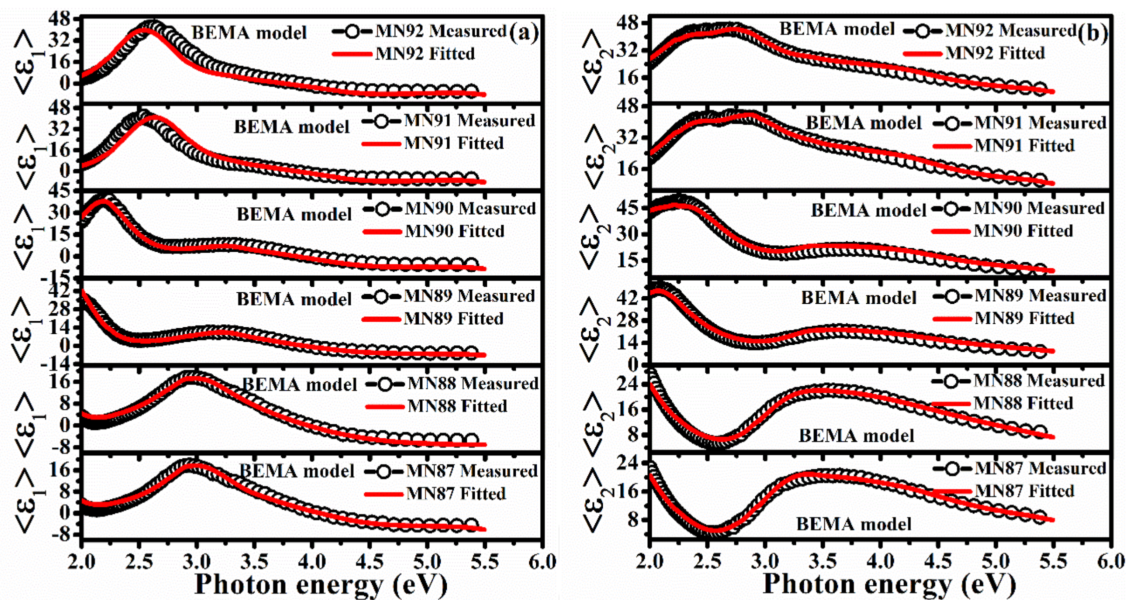

Fig. 4.11(a, b). Measured and fitted (BEMA model) values of $< \varepsilon_1 >$ and $< \varepsilon_2 >$ of a-Si:H(n) films as a function of photon energy.

Table 4.4. The estimated void (f_v), amorphous (f_a) and crystalline (f_c) volume fractions, thickness and surface roughness (d_s) of a-Si:H(n) films.

Sample	HFR (SCCM)	Thickness (nm)	f_v (%)	f_a (%)	f_c (%)	d_s (nm)	d_{RMS} (nm) (AFM)
MN87	30	109	17.59	80.86	1.53	1.46	1.6
MN88	40	98	16.86	81.92	1.21	1.82	1.8
MN89	50	75	15.94	80.95	3.10	2.03	2.0
MN90	60	67	14.67	79.83	5.50	2.50	2.1
MN91	70	62	11.49	79.08	9.42	2.65	3.0
MN92	80	53	13.35	72.89	13.98	3.14	3.3

Fig. 4.12 shows the void (f_v), amorphous (f_a) and crystalline (f_c) volume fractions of a-Si:H(n) films as a function of hydrogen flow rate. It is observed that void fraction has systematically decreased up to 70 SCCM of HFR and then increased at 80 SCCM of HFR. The least void fraction of 11.49% was observed at 70 SCCM of HFR (*MN91*), whereas crystalline fraction has continuously increased. The maximum crystalline fraction of 13.49% was observed at 80 SCCM of HFR. The amorphous fraction is found to be nearly independent of HFR till 70 SCCM and then decreased with further increase in HFR to 80 SCCM. The surface roughness of the films is found to increase from 1 to 3 nm with increase in HFR due to increased ion bombardment and number collisions among the neighbouring gas molecules of the films. The trend is similar to that observed for a-Si:H(p) films (Section 4.2.1.1).

TH-2097_126121019

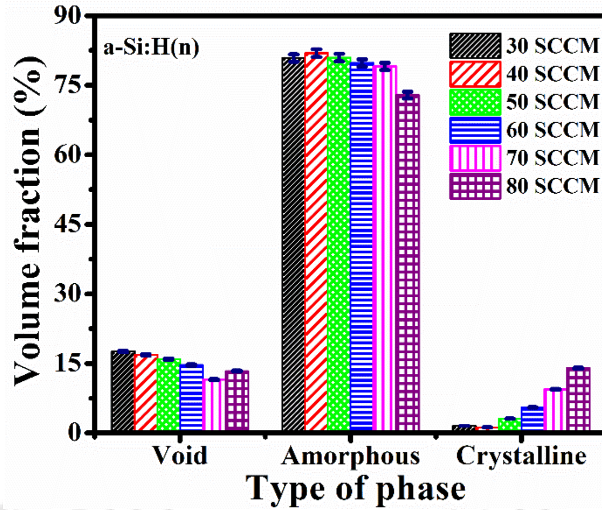

Fig. 4.12. Void, amorphous and crystalline volume fractions of a-Si:H(n) film corresponding to HFR.

4.2.2.2. UV-Vis-NIR studies

Fig. 4.13 shows the UV-Vis-NIR transmission spectra of *MN87-MN92* films. In Fig. 4.13, a clear shift in absorption edge of transmission spectra of films towards lower wavelength is observed with increase in HFR. The Tauc's plot has been used to calculate the optical band gap of the films using Eq. 2.21 [21,22] and the values are listed in Table 4.3. These values are in good agreement with those estimated from SE analysis. It is observed that thickness of the films has decreased and band gap has increased with increase in HFR during deposition. The trend is similar to that reported for undoped and boron doped a-Si:H films (Sec. 4.2.1.2) [19,23].

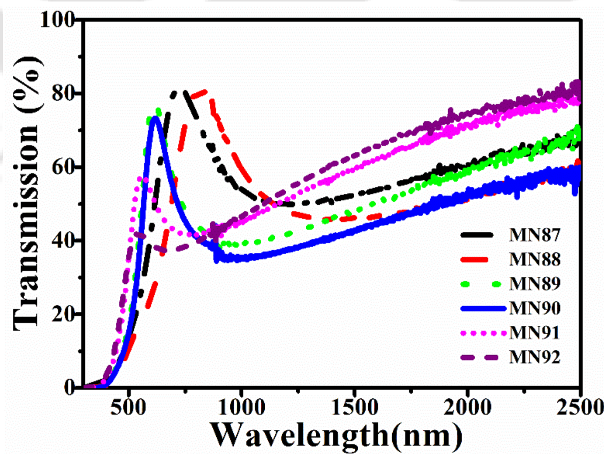

Fig. 4.13. The UV-Vis-NIR transmission spectra of a-Si:H(n) thin films.

4.2.2.3. AFM morphology studies

Fig. 4.14(a-f) show the AFM surface morphology of *MN87-MN92* thin films measured on scan area of 2x2 μm^2 in non-contact mode. It is observed that all the films are uniform throughout the sample and formation of voids took place at lower HFR of the films. The RMS surface roughness (d_{RMS}) values are found to be 1.6 to 3.3 nm corresponding to *MN87* to *MN92* films respectively and also listed in Table 4.4. The grain size and roughness of the films has increased with increase in HFR of the films. The roughness of the films from the AFM studies is also quite similar to the estimated surface roughness of the films from SE measurements.

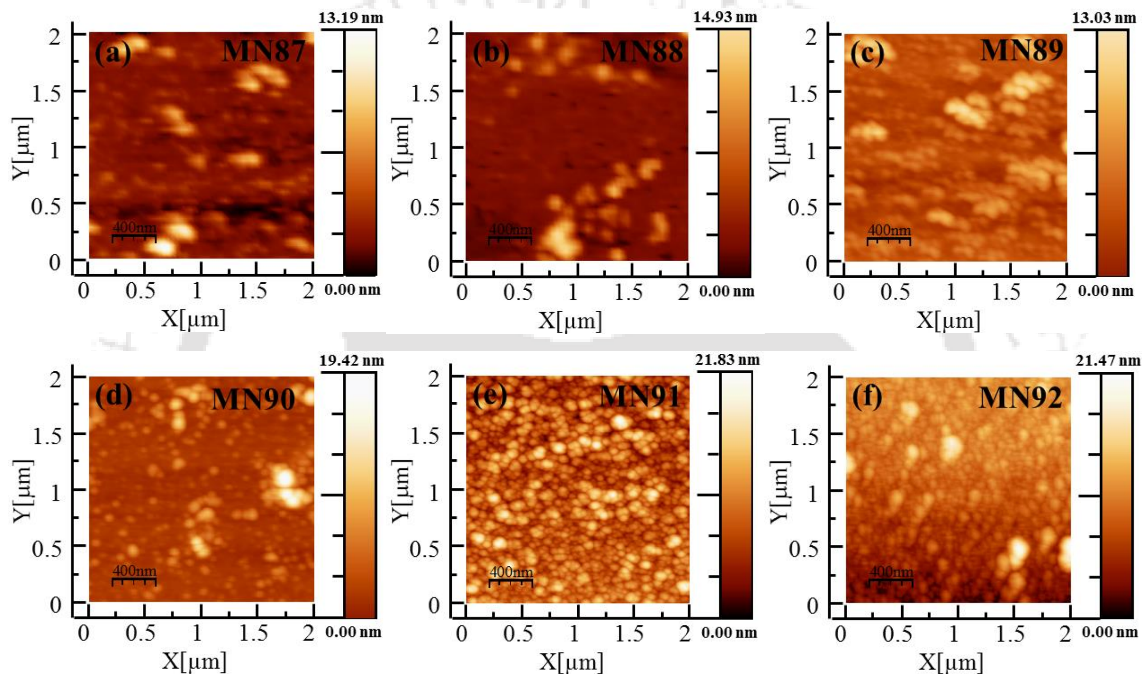

Fig. 4.14(a-f). AFM surface morphology of *MN87-MN92* films.

During growth of a-Si:H films, most of the hydrogen atoms and molecules interact with growing film and make possible chemical reactions. Three main processes take place during growth of film with hydrogen dilution, which are i) hydrogen coverage on the growing surface, ii) chemical etching and cleaning, and iii) migration of adsorbed precursors on surface [24–26]. The atomic hydrogen diffuses on growing surface as well as into the bulk of the films. The atomic hydrogen enhances surface diffusion of precursors such as SiH_3 and produce local heating through hydrogen exchange reactions on the growing surface [25]. These energetic precursors occupy more stable and favourable sites. Strong Si-Si and Si-H bonds are formed by removing weak Si-Si, Si-H_2 bonds. The hydrogen atoms also etch out some amorphous fraction [25,27]. This results in structural transition from amorphous to nano/micro crystalline phase depending on hydrogen dilution of the precursor gases. After certain hydrogen dilution,

TH-2097_126121019

film quality start to degrade and defects formation starts in growing film. The films deposited at 30-50 SCCM for a-Si:H(p) and 30-60 SCCM for a-Si:H(n) of HFR are amorphous in nature and have disordered Si network with most of the Si atoms bonded as Si-H_2. SE analysis revealed that these films have low A, high C value and higher void fraction, which are estimated by TL and BEMA model respectively. In our case, film microstructure, bonding arrangement and Si-H bonding configuration have improved up to 60 SCCM and 70 SCCM of HFR for a-Si:H(p) and a-Si:H(n) films respectively. This observed variation in HFR of films for similar type of microstructure is mainly due to higher hydrogen concentration in B_2H_6 than PH_3 gas. Beyond these flow rates, further increase in atomic hydrogen flux increases the rate of ion bombardment resulting in formation of microvoids and the reduced compactness of the films. However, crystallinity has enhanced due to increase in hydrogen radical density. This is confirmed by SE analysis; peak position and amplitude of $< \varepsilon_2 >$ spectra has changed with variation of hydrogen flow rate during deposition of films. Films deposited at 60 SCCM (a-Si:H(p)) and 70 SCCM (a-Si:H(n)) of HFR have best device quality microstructural properties and onset of nanocrystalline phase, which are used for p and n-layer of c-Si/a-Si:H heterojunction solar cells.

4.3. Conclusion

Influence of hydrogen flow rate on microstructure, optical properties of a-Si:H(p) and a-Si:H(n) films was studied by SE measurements. It is observed that microstructure of a-Si:H(p) and a-Si:H(n) films changes from amorphous to nano crystalline phase by increasing hydrogen flow rate during film growth. This phase transition is confirmed by SE analysis; shift in peak position of pseudo dielectric function of these films from 3.6 eV (for pure a-Si:H) to 4.1 eV with a shoulder peak at 3.4 eV (near onset of nanocrystalline) is observed as the hydrogen flow rate is increased. The bandgap, surface roughness and crystallinity of the films has increased with increase in HFR for the films. It is found that less defective a-Si:H films with smaller void fraction and improved Si-H bond density are obtained at 60 SCCM and 70 SCCM of HFR for a-Si:H(p) and a-Si:H(n) films respectively. This optimised parameters leading to films with improved microstructure and near the onset of nanocrystalline phase are used for fabrication of c-Si/a-Si:H heterojunction solar cells in Chapter 6 and Chapter 7.

TH-2097_126121019

4.4. References

[1] K. Masuko, M. Shigematsu, T. Hashiguchi, D. Fujishima, M. Kai, N. Yoshimura, T. Yamaguchi, Y. Ichihashi, T. Mishima, N. Matsubara, T. Yamanishi, T. Takahama, M. Taguchi, E. Maruyama, S. Okamoto, Achievement of More Than 25% Conversion Efficiency With Crystalline Silicon Heterojunction Solar Cell, IEEE J. Photovoltaics. 4 (2014) 1433–1435. doi:10.1109/JPHOTOV.2014.2352151.

[2] M. Taguchi, A. Yano, S. Tohoda, K. Matsuyama, Y. Nakamura, T. Nishiwaki, K. Fujita, E. Maruyama, 24.7% Record efficiency HIT solar cell on thin silicon wafer, IEEE J. Photovoltaics. 4 (2014) 96–99. doi:10.1109/JPHOTOV.2013.2282737.

[3] Y. Tsunomura, Y. Yoshimine, M. Taguchi, T. Baba, T. Kinoshita, H. Kanno, H. Sakata, E. Maruyama, M. Tanaka, Twenty-two percent efficiency HIT solar cell, Sol. Energy Mater. Sol. Cells. 93 (2009) 670–673. doi:10.1016/j.solmat.2008.02.037.

[4] M.A. Green, Y. Hishikawa, A.W.Y.H. Baillie, E.D. Dunlop, D.H. Levi, Solar cell efficiency tables (version 51), Prog. Photovoltaics Res. Appl. 26 (2018) 3–12. doi:10.1002/pip.2978.

[5] S. De Wolf, A. Descoeudres, Z.C. Holman, C. Ballif, High-efficiency Silicon Heterojunction Solar Cells: A Review, Green. 2 (2012) 7–24. doi:10.1515/green-2011-0018.

[6] J. Ramanujam, A. Verma, Photovoltaic Properties of a-Si : H Films Grown by Plasma Enhanced Chemical Vapor Deposition : A Review, Mater. Express. 2 (2012) 177–196. doi:10.1166/mex.2012.1073.

[7] H. Fujiwara, Spectroscopic Ellipsometry Principles and Applications, Willey Publ. (2007). doi:10.1002/9780470060193,ISBN:9780470016084.

[8] T. Yuguchi, Y. Kanie, N. Matsuki, H. Fujiwara, Complete parameterization of the dielectric function of microcrystalline silicon fabricated by plasma-enhanced chemical vapor deposition, J. Appl. Phys. 111 (2012) 083509. doi:10.1063/1.4704158.

[9] L.R. Dahal, J. Li, J.A. Stoke, Z. Huang, A. Shan, A.S. Ferlauto, C.R. Wronski, R.W. Collins, N.J. Podraza, Applications of real-time and mapping spectroscopic ellipsometry for process development and optimization in hydrogenated silicon thin-film photovoltaics technology, Sol. Energy Mater. Sol. Cells. 129 (2014) 32–56. doi:10.1016/j.solmat.2014.01.028.

[10] R.W. Collins, A.S. Ferlauto, G.M. Ferreira, C. Chen, J. Koh, R.J. Koval, Y. Lee, J.M. Pearce, C.R. Wronski, Evolution of microstructure and phase in amorphous, protocrystalline, and microcrystalline silicon studied by real time spectroscopic ellipsometry, Sol. Energy Mater. Sol. Cells. 78 (2003) 143–180. doi:10.1016/S0927-0248(02)00436-1.

[11] G.E.Jellison and F.A. Modine, Parameterization of the optical functions of amorphous materials in the interband region, Appl. Phys. Lett. 69 (1996) 371–373.

TH-2097_126121019

doi:10.1063/1.118064.

[12] S. Kageyama, M. Akagawa, H. Fujiwara, Dielectric function of a-Si:H based on local network structures, Phys. Rev. B. 83 (2011) 195205. doi:10.1103/PhysRevB.83.195205.

[13] A. Fontcuberta i Morral and P. Roca i Cabarrocas, C.Clerc, Structure and hydrogen content of polymorphous silicon thin films studied by spectroscopic ellipsometry and nuclear measurements, Phys. Rev. B. 69 (2004) 125307. doi:10.1103/PhysRevB.69.125307.

[14] H. Zhang, X. Zhang, G. Hou, C. Wei, J. Sun, X. Geng, S. Xiong, Y. Zhao, The microstructure and optical properties of p-type microcrystalline silicon thin films characterized by ex-situ spectroscopic ellipsometry, Thin Solid Films. 521 (2012) 17–21. doi:10.1016/j.tsf.2012.03.081.

[15] Y.-H. Chu, C.-C. Lee, T.-H. Chang, S.-Y. Chang, J.-Y. Chang, T. Li, I.-C. Chen, Investigation of hydrogenated amorphous silicon as passivation layer by high density plasma, Thin Solid Films. 570 (2014) 591–594. doi:10.1016/j.tsf.2014.03.064.

[16] F.I. Morral, P. Roca i Cabarrocas, Etching and hydrogen diffusion mechanisms during a hydrogen plasma treatment of silicon thin films, J. Non. Cryst. Solids. 299–302 (2002) 196–200. doi:10.1016/S0022-3093(01)01001-8.

[17] S. Kageyama, M. Akagawa, H. Fujiwara, Ellipsometry characterization of a-Si:H layers for thin-film solar cells, J. Non. Cryst. Solids. 358 (2012) 2257–2259. doi:10.1016/j.jnoncrysol.2011.12.042.

[18] Venkanna Kanneboina, R. Madaka, P. Agarwal, High open circuit voltage c-Si/a-Si:H heterojunction solar cells: Influence of hydrogen plasma treatment studied by spectroscopic ellipsometry, Sol. Energy. 166 (2018) 255–266. doi:10.1016/j.solener.2018.03.068.

[19] Venkanna Kanneboina, R. Madaka, P. Agarwal, Spectroscopic ellipsometry studies on microstructure evolution of a-Si:H to nc-Si:H films by H2 plasma exposure, Mater. Today Commun. 15 (2018) 18–29. doi:10.1016/j.mtcomm.2018.02.023.

[20] D.E. Aspnes, Optical properties of thin films, Thin Solid Films. 89 (1982) 249–262. doi:10.1016/0040-6090(82)90590-9.

[21] J. Tauc, R. Grigorovici, A. Vancu, Optical Properties and Electronic Structure of Amorphous Germanium, Phys. Status Solidi. 15 (1966) 627–637. doi:10.1002/pssb.19660150224.

[22] J. Tauc, A. Menth, States in the gap, J. Non. Cryst. Solids. 8–10 (1972) 569–585. doi:10.1016/0022-3093(72)90194-9.

[23] P. Gogoi, H.S. Jha, P. Agarwal, Effect of Silane flow rate on microstructure of Silicon films deposited by HWCVD, J. Non. Cryst. Solids. 358 (2012) 1990–1994. doi:10.1016/j.jnoncrysol.2011.12.095.

TH-2097_126121019

[24] R.A.Street, Hydrogenated amorphous silicon, Cambridge Solid State Ser. (1991). doi:10.1017/CBO9780511525247,ISBN:9780521371568.

[25] Akihisa Matsuda, Microcrystalline silicon. Growth and application, J. Non. Cryst. Solids. 338–340 (2004) 1–12. doi:10.1016/j.jnoncrysol.2004.02.012.

[26] A. Matsuda, M. Takai, T. Nishimoto, M. Kondo, Control of plasma chemistry for preparing highly stabilized amorphous silicon at high growth rate, Sol. Energy Mater. Sol. Cells. 78 (2003) 3–26. doi:10.1016/S0927-0248(02)00431-2.

[27] Z. Remes , M. Vanecek P. Torres , U. Kroll, A.H. Mahan, R.S. Crandall, Optical determination of the mass density of amorphous and microcrystalline silicon layers with different hydrogen contents, J. Non. Cryst. Solids. 227–230 (1998) 876–879. doi:10.1016/S0022-3093(98)00207-5.

TH-2097_126121019

Chapter 5

Influence of Deposition Temperature on Structural, Optical and Electrical Properties of ITO Thin Films

This chapter presents the influence of deposition temperature on microstructure, morphology, optical and electrical properties of Indium tin oxide (ITO) thin films. The transparent conductive oxide (TCO) layer is an important layer to improve the efficiency of solar cells. Indium tin oxide (ITO), Zinc oxide (ZnO), Alumina doped zinc oxide (ZnO:Al) are most commonly used TCO layers in solar cells. Indium tin oxide (ITO) thin films are used in many electronic devices such as solar cells [1–3], liquid crystal displays (LCDs) [4], light emitting diodes (LEDs) [5,6] and also in biology to determine glucose concentration due to electroluminescent properties of ITO films [7]. The ITO thin films have significant importance in solar cells as transparent conducting oxide and antireflection layer [1,8–10]. In order to improve performance of solar cells, the key requirements of ITO films are high transparency in visible region, high conductivity and low sheet resistance [2,11–13]. In order to optimize the deposition parameters to get high quality TCO, indium tin oxide (ITO) thin films were deposited on corning1737 glass substrate at deposition temperature ranging from 50 to 200 ^{o}C using RF Sputtering technique. The X-ray diffraction (XRD) was used to study the structure, crystallite size and micro strain of the ITO films. Transmission spectra of the ITO thin films were measured with UV-Vis-NIR spectrometer in the wavelength range of 200 to 1500 nm and used to estimate band gap of the films. Atomic Force Microscope (AFM) and Field Emission Scanning Electron Microscope (FESEM) measurements were used to study the surface morphology of the films. The sheet resistance of ITO films was measured using four probe current-voltage (I-V) measurements.

5.1. Experimental details

Indium tin oxide (ITO) thin films were deposited on corning 1737 glass substrate using radio frequency sputtering (RF Sputtering) technique. The parameters used for deposition of ITO films were: Argon flow rate (AFR) of 7 SCCM, RF power of 80 W, process pressure (PP) of

TH-2097_126121019

0.062 mbar and substrate temperature varied from 50 to 200 ºC. The samples *SP335-SP338* correspond to deposition temperature of 50-200 ºC respectively.

5.2. Results and discussion

5.2.1. X-Ray diffraction analysis

Fig. 5.1(a, b) show the XRD pattern of *SP335-SP338* ITO films and Lorentzian peak fitting of *SP338* film respectively. It is observed that the films deposited at 50ºC were nanocrystalline in nature. The film crystallinity was improved as deposition temperature was increased and films were completely crystallized at 150 ºC. The intensity of the diffraction peaks was also increased with increasing deposition temperature. This indicates that films deposited at higher temperature are highly crystalline and oriented with reduced crystalline defects [14–16]. The preferential direction of growth for films deposited at 50 and 100 ºC is [222], whereas for films deposited at higher temperature 150 and 200 ºC, growth direction corresponds to [400]. Here 2θ represents the angle between the direct X-ray beam and scattered beam.

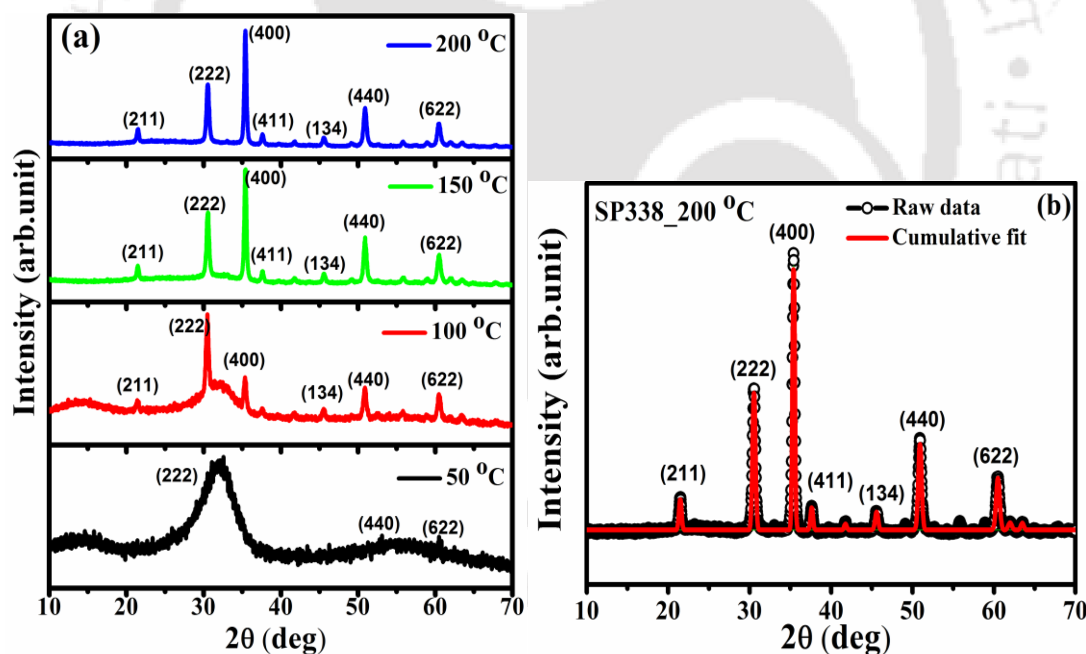

Fig. 5.1. (a) XRD pattern of *SP335-SP338* ITO films, (b) Fitted peaks in *SP338* film.

The Williamson-Hall (W-H) method has been used to calculate accurate crystallite size and microstrain in the films using Eq.2.15 given in section 2.2.4, Chapter 2 [17,18]. Fig. 5.2 shows the W-H plot of *SP338* film deposited at 200 ºC. The values of estimated crystallite size and micro strain of the ITO films are listed in Table 5.1. It was observed that the crystallite size of films has increased and micro strain in the films has decreased with increase in deposition

TH-2097_126121019

temperature from 50 to 200 °C. The ITO films have completely crystallized at 150 °C and then saturated at deposition temperature of 200 °C. The *SP337*(150 °C) and *SP338*(200 °C) films have crystallite size of 26.86 and 27.50 nm and very less micro strain of 0.1% in the films. The *SP336* (100 °C) showed crystallite size of 21.12 nm and also slightly higher micro strain than other films. The crystallite size of 1.57 nm of *SP335* at 50 °C film was calculated from Debye-Sherrer formula (Eq. 2.14) [19].

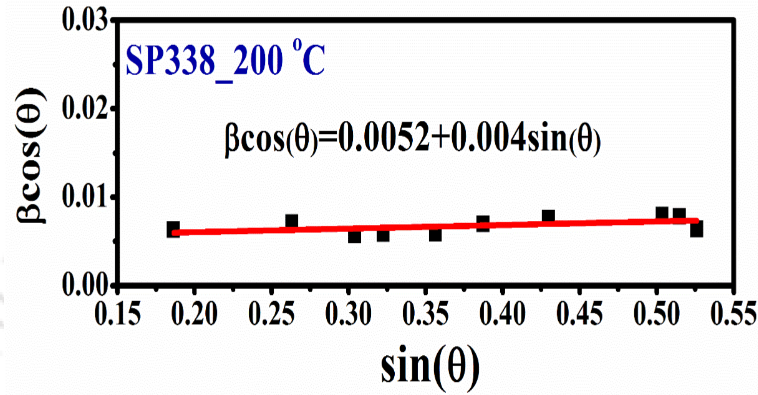

Fig. 5.2. Williamson-Hall plot of *SP338* ITO thin film.

Table 5.1. Calculated crystallite size (d_{XRD}) and micro strain (ϵ) in the films.

Sample	Dep. temp (°C)	d_{XRD} (nm)	Strain (%)
SP338	200	27.50±1.4	0.1
SP337	150	26.86±1.3	0.1
SP336	100	21.72±1.1	0.2
SP335	50	1.57±0.1	-

5.2.2. UV-Vis-NIR spectroscopy studies

Fig. 5.3a shows the UV-Vis-NIR transmission spectra of *SP335-SP338* films. All the films show high transmission of 90-98% in the wavelength range of 400-1500 nm. Fig. 5.3b shows the linear fit of $(\alpha h\nu)^2$ as function of $h\nu$ to estimate the optical bandgap. The optical bandgap of films has been estimated using Tauc's plot (Eq. 2.21) [20] and values are given in Table 5.2. It is clearly observed that absorption edge of the films has shifted to lower wavelength side with increase in deposition temperature (Fig. 5.3). These highly transparent ITO filmswith high bandgap allow most of the photons to reach the absorber layer in solar cells. Thickness of the ITO films was estimated by stylus profilometer. The estimated deposition rates are 10 nm/min, 9.1 nm/min, 8.2 nm/min and 7.8 nm/min correspond to *SP335* to *SP388*(50-200°C) films respectively. The optical bandgap of the ITO films has increased and thickness has slightly decreased as deposition temperature is increased.

TH-2097_126121019

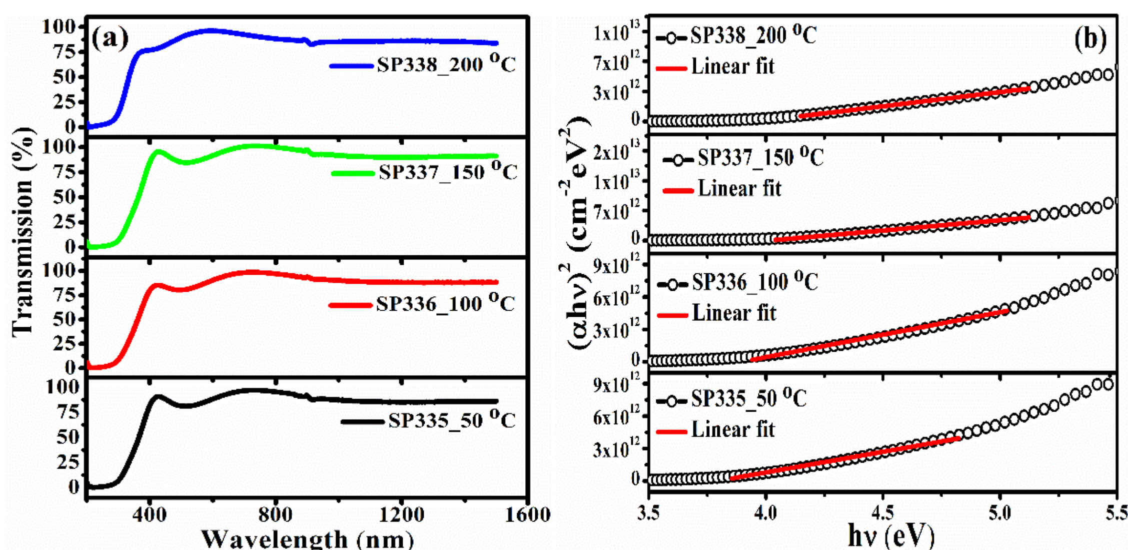

Fig 5.3. (a). UV-Vis-NIR transmission spectra, (b). Plot of $(\alpha h\nu)^2$ as function of $h\nu$ of ITO films.

5.2.3. FESEM morphology studies

Fig. 5.4(a-d) show the FESEM surface morphology of the *SP335-SP338* (50-200 °C) ITO films respectively. It is clearly observed that the growth and surface morphology of the films changes with change in deposition temperature. The films are uniform and the grain size of the films has increased with increase in deposition temperature.

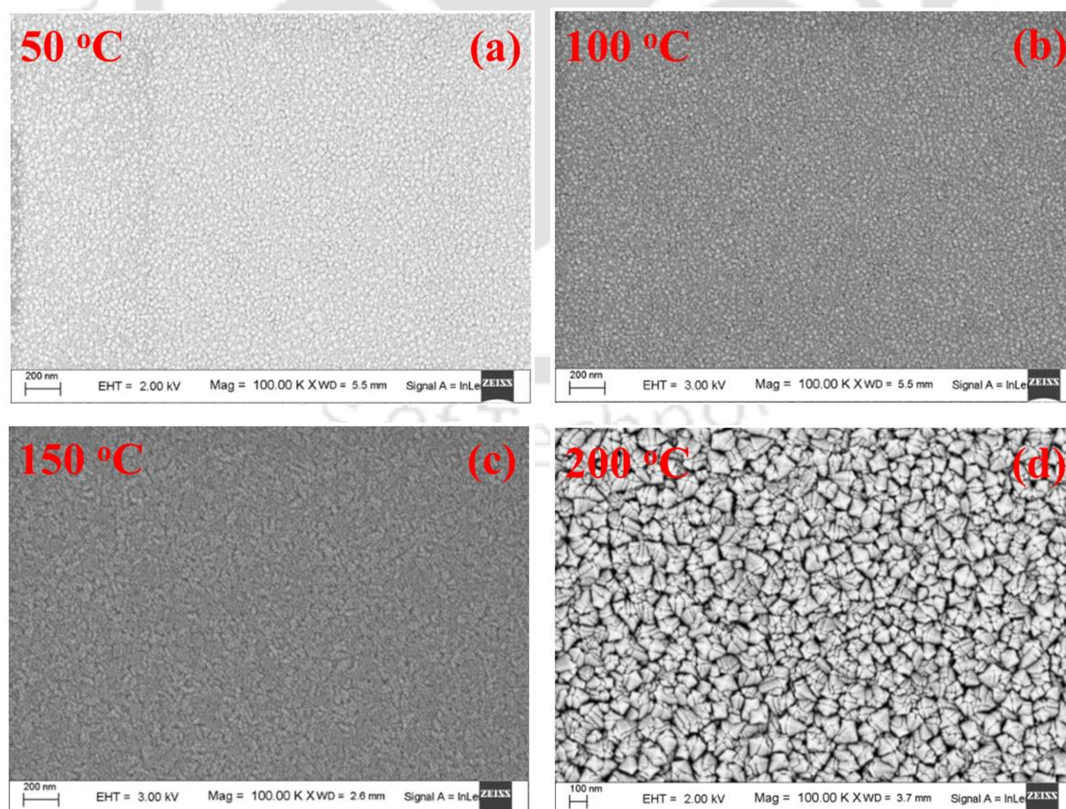

Fig. 5.4(a-d). FESEM surface morphology of the *SP335-SP338* (50-200 °C) ITO films.

TH-2097_126121019

Table 5.2. Estimated thickness, optical bandgap (E_g), surface roughness (d_{RMS}), resistivity (ρ) and sheet resistance (R_{sheet}) of films.

	Profilometer	UV-Vis-NIR	AFM	*I-V* measurement	
Sample	Thickness (nm)	E_g (eV)	d_{RMS} (nm)	ρ (Ωcm)(x10^{-5})	R_{sheet} (Ω/□)
SP338	86±7	3.98±0.02	10.77±0.4	6.4±0.2	7.49±0.3
SP337	90±8	3.85±0.01	6.11±0.5	6.7±0.1	7.51±0.2
SP336	100±7	3.74±0.01	13.81±0.4	25.0±0.4	25.01±0.3
SP335	110±6	3.55±0.02	14.38±0.6	37.3 ±0.2	33.94±0.5

5.2.4. AFM morphology studies

Fig. 5.5(a-d) show the AFM surface morphology of the ITO films deposited at 50-200 °C respectively. It is observed that at lower deposition temperature (50 and 100 °C), films are not uniform, with voids in the films and high surface roughness. With further increase in deposition temperature, uniform films are grown with less surface roughness.

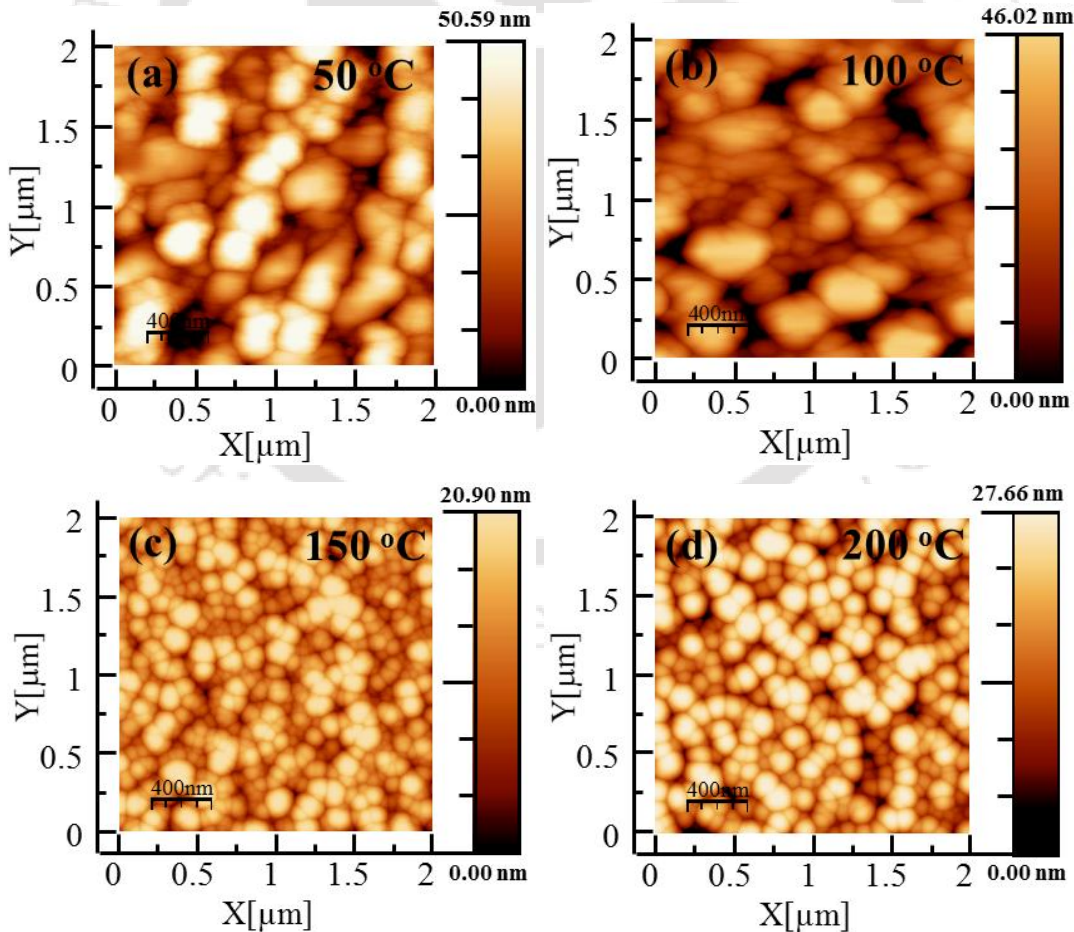

Fig. 5.5(a-d). AFM morphology of ITO films.

TH-2097_126121019

Measured RMS roughness values are 14.38, 13.81, 6.11 and 10.77 nm corresponding to deposition temperature 50, 100, 150 and 200°C respectively (Table 5.2). At lower deposition temperature, atoms have less energy to occupy stable position, which create path to formation of voids and rough films. At higher deposition temperature of 150 ^{o}C and above, atoms have sufficient energy to diffuse on surface as well as in the bulk of the films. This results in strong bonds with neighbouring atoms and very uniform films. It is observed that surface roughness of *SP338* film is higher than *SP337* film, this could be due to increased grain size and desorption of atoms from the growing surface at deposition temperature of 200 ^{o}C.

5.2.5. Four probe *I-V* measurements

Resistivity and sheet resistance of ITO films were estimated from four probe *I-V* measurements using Eq. 2.24 and Eq. 2.25 and values are given in Table 5.2. The separation between each probe was 1 mm and detailed description of four probe method was given in section 2.2.9.2, Chapter 2. It is found that sheet resistance and resistivity have decreased with increase in deposition temperature. The low sheet resistance of 7.5 Ω/□ and 7.4 Ω/□ and resistivity of 6.7×10^{-5} Ωcm and 6.4×10^{-5} Ωcm are obtained for films deposited at 150 and 200 ^{o}C respectively. These resistivity and sheet resistance values are one order of magnitude lower than films deposited at 50 and 100 ^{o}C.

5.3. Conclusion

Indium tin oxide (ITO) thin films were deposited by RF sputtering technique with varying deposition temperature of 50 to 200 ^{o}C. It is observed that the films deposited at 50°C were nanocrystalline in nature. The film crystallinity was enhanced with increases in deposition temperature and saturated at 150 ^{o}C. Williamson-Hall plot has been used to estimate crystallite size of the ITO films, which are 21.7, 26.8 and 27.5 nm corresponding to films deposited at 100, 150 and 200 ^{o}C respectively. It is found that films deposited at 150 ^{o}C have high transmission of 91-98% in the wavelength range of 400-1500 nm, low sheet resistance of 7.5 Ω/□ and surface roughness of 6.1 nm. These highly crystallized, transparent, low sheet resistance and low temperature ITO films were used for improving the interface properties between ITO and doped layers and efficiency of c-Si/a-Si:H heterojunction solar cells presented in Chapter 6 and Chapter 7.

TH-2097_126121019

5.4. References

[1] S. De Wolf, A. Descoeudres, Z.C. Holman, C. Ballif, High-efficiency Silicon Heterojunction Solar Cells: A Review, Green. 2 (2012) 7–24. doi:10.1515/green-2011-0018.

[2] T. Mishima, M. Taguchi, H. Sakata, E. Maruyama, Development status of high-efficiency HIT solar cells, Sol. Energy Mater. Sol. Cells. 95 (2011) 18–21. doi:10.1016/j.solmat.2010.04.030.

[3] M. Taguchi, A. Yano, S. Tohoda, K. Matsuyama, Y. Nakamura, T. Nishiwaki, K. Fujita, E. Maruyama, 24.7% Record efficiency HIT solar cell on thin silicon wafer, IEEE J. Photovoltaics. 4 (2014) 96–99. doi:10.1109/JPHOTOV.2013.2282737.

[4] H. Ryu, J. Kang, Y. Han, D. Kim, J.J. Pak, W.K. Park, M.S. Yang, Indium-tin oxide/Si contacts with In- and Sn-diffusion barriers in polycrystalline Si thin-film transistor liquid-crystal displays, J. Electron. Mater. 32 (2003) 919–924. doi:10.1007/s11664-003-0223-y.

[5] A.G. Macedo, E.A. de Vasconcelos, R. Valaski, F. Muchenski, E.F. da Silva, A.F. da Silva, L.S. Roman, Enhanced lifetime in porous silicon light-emitting diodes with fluorine doped tin oxide electrodes, Thin Solid Films. 517 (2008) 870–873. doi:10.1016/j.tsf.2008.07.007.

[6] H. Chen, C. Qiu, M. Wong, H.S. Kwok, DC sputtered indium-tin oxide transparent cathode for organic light-emitting diode, IEEE Electron Device Lett. 24 (2003) 315–317. doi:10.1109/LED.2003.812550.

[7] T. Miyasaka, Y. Jinbo, K. Sakai, Y. Yoshimi, Determination of glucose concentration by electrolumescence of an Indium tin oxide electrode, Trans IchemE. 76 (1998) 1–5.

[8] Venkanna Kanneboina, R. Madaka, P. Agarwal, High open circuit voltage c-Si/a-Si:H heterojunction solar cells: Influence of hydrogen plasma treatment studied by spectroscopic ellipsometry, Sol. Energy. 166 (2018) 255–266. doi:10.1016/j.solener.2018.03.068.

[9] K. Masuko, M. Shigematsu, T. Hashiguchi, D. Fujishima, M. Kai, N. Yoshimura, T. Yamaguchi, Y. Ichihashi, T. Mishima, N. Matsubara, T. Yamanishi, T. Takahama, M. Taguchi, E. Maruyama, S. Okamoto, Achievement of More Than 25% Conversion Efficiency With Crystalline Silicon Heterojunction Solar Cell, IEEE J. Photovoltaics. 4 (2014) 1433–1435. doi:10.1109/JPHOTOV.2014.2352151.

[10] W. Liu, L. Zhang, S. Cong, R. Chen, Z. Wu, F. Meng, Q. Shi, Z. Liu, Controllable a-Si:H/c-Si interface passivation by residual SiH4 molecules in H2 plasma, Sol. Energy Mater. Sol. Cells. 174 (2018) 233–239. doi:10.1016/j.solmat.2017.09.009.

[11] S.Y. Lien, Characterization and optimization of ITO thin films for application in

TH-2097_126121019

heterojunction silicon solar cells, Thin Solid Films. 518 (2010) S10–S13. doi:10.1016/j.tsf.2010.03.023.

[12] S. Tohoda, D. Fujishima, A. Yano, A. Ogane, K. Matsuyama, Y. Nakamura, N. Tokuoka, H. Kanno, T. Kinoshita, H. Sakata, M. Taguchi, E. Maruyama, Future directions for higher-efficiency HIT solar cells using a Thin Silicon Wafer, J. Non. Cryst. Solids. 358 (2012) 2219–2222. doi:10.1016/j.jnoncrysol.2012.03.025.

[13] L. Barraud, Z.C. Holman, N. Badel, P. Reiss, A. Descoeudres, C. Battaglia, S. De Wolf, C. Ballif, Hydrogen doped indium oxide/indium tin oxide bilayers for high efficiency silicon heterojunction solar cells, Sol. Energy Mater. Sol. Cells. 115 (2013) 151–156. doi:10.1016/j.solmat.2013.03.024.

[14] A. Monshi, M.R. Foroughi, M.R. Monshi, Modified Scherrer equation to estimate more accurately nano-crystallite size using XRD, World J. Nano Sci. Eng. 2 (2012) 154. doi:10.4236/wjnse.2012.23020.

[15] S. Lele, T.R. Anantharaman, Influence of crystallite shape on particle size broadening of Debye-Scherrer reflections, Proc. Indian Acad. Sci. - Sect. A. 64 (1966) 261–274. doi:10.1007/BF03047543.

[16] O. Tuna, Y. Selamet, G. Aygun, L. Ozyuzer, High quality ITO thin films grown by dc and RF sputtering without oxygen, J. Phys. D. Appl. Phys. 43 (2010) 055402. doi:10.1088/0022-3727/43/5/055402.

[17] G.K. Williamson, W.H. Hall, X-ray line broadening from filed aluminium and wolfram, Acta Metall. 1 (1953) 22–31. doi:10.1016/0001-6160(53)90006-6.

[18] G.K. Williamson, W.H. Hall, Discussion of the Theories of Line Broadening, Acta Metall. 1 (1953) 22. doi:10.1016/0001-6160(53)90006-6.

[19] A.L. Patterson, The scherrer formula for X-ray particle size determination, Phys. Rev. 56 (1939) 978–982. doi:10.1103/PhysRev.56.978.

[20] J. Tauc, R. Grigorovici, A. Vancu, Optical Properties and Electronic Structure of Amorphous Germanium, Phys. Status Solidi. 15 (1966) 627–637. doi:10.1002/pssb.19660150224.

TH-2097_126121019

Chapter 6

Influence of a-Si:H(i) Layer Thickness on the Performance of c-Si/a-Si:H Heterojunction Solar Cells

This chapter presents the influence of a-Si:H(i) thickness layer on the performance of the c-Si/a-Si:H heterojunction solar cells. Our main goal has been to achieve the high open circuit voltage and high efficiency with single side c-Si/a-Si:H heterojunction solar cells. As most of the research groups are focused on double side silicon heterojunction (SHJ) solar cells to improve the performance of the devices, less attention is paid to the single side solar cells. Number of processing steps and time are less in fabrication of single side c-Si/a-Si:H heterojunction solar cells. With this aim one sided c-Si/a-Si:H heterojunction solar cells (*Ag/Al/c-Si(n)/a-Si:H(i)/a-Si:H(p)/ITO/Ag*) were fabricated on double side polished n- type c-Si wafer by RFPECVD technique in multi-chamber system. To control the thickness of a-Si:H(i) layer, which plays a main role in the performance of solar cells, the cells were fabricated with hydrogen plasma treatment of a-Si:H(i) layer of different thicknesses prior to the deposition of top a-Si:H(p) layer. The thickness, optical band gap and microstructure of different a-Si:H layers in the cells were estimated using Spectroscopic ellipsometry. Influence of hydrogen plasma treatment of a-Si:H(i) layer on thickness, microstructure of the films and passivation of the interface defects was also studied in detail. This chapter also presents influence of H_2 plasma treatment (HPT) on the open circuit voltage (V_{oc}), short circuit current density (J_{sc}) and fill factor (FF) and then performance of solar cells. Surface morphology of c-Si wafer and a-Si:H films with and without HPT was studied by FESEM and AFM measurements. Spectral response of the solar cells was measured by quantum efficiency (QE) technique.

6.1. Experimental details

6.1.1. Fabrication of c-Si/a-Si:H heterojunction solar cells

One sided c-Si/a-Si:H heterojunction solar cells (*Ag/Al/c-Si(n)/a-Si:H(i)/a-Si:H(p)/ITO/Ag*) were fabricated by RFPECVD in multi chamber system. After standard RCA cleaning of the

TH-2097_126121019

c-Si wafer (detailed cleaning procedure is given in the section 2.1.3.1, Chapter 2) [1,2], aluminium (Al) was deposited by thermal evaporation on one surface of wafer. The wafers were subsequently annealed at 400 ^oC in high vacuum (10^{-6}-10^{-7} mbar) for 1 hr to ensure the diffusion of Al in Si for good back contact. The top surface of Si wafer was subjected to 10 min H_2 plasma and then a-Si:H(i) layer of varying thickness i.e 50, 45, 40 and 35 nm was deposited. The Si wafers were shifted to a-Si:H(p) layer deposition chamber, where the a-Si:H(i) layers were subjected to 2 min HPT prior to the deposition of top a-Si:H(p) layer. Subsequently 20 nm thick a-Si:H(p) layer was deposited to complete the cell. Deposition parameters used were: H_2 gas flow rate of 50 SCCM, pure SiH_4 flow rate of 4 SCCM, process pressure of 0.42 mbar, rf power of 30 W and deposition temperature of 200 ^oC for a-Si:H(i) layer. For a-Si:H(p) layer, B_2H_6 (2% of B_2H_6 diluted in H_2) gas at a flow rate of 6 SCCM along with H_2 (60 SCCM) was introduced with other parameters same as those for i-layer. For H_2 plasma treatment, only H_2 at a gas flow rate of 50 SCCM was used with other parameters; rf power, substrate temperature, process pressure maintained same as those for i and p- layers. In silicon heterojunction (SHJ) solar cells, the thickness of i- and p-layer is typically 5-10 nm [3,4]. However, it is very challenging to deposit very thin (5-10 nm) a-Si:H films with device quality. For this reason, thick a-Si:H(i) layers were deposited and then subjected to HPT to etch the film, as well as improve the quality of a-Si:H(i) layer and passivate defect states at the interface. After the deposition of a-Si:H(p) layer, 80 nm of ITO layer on top of the a-Si:H(p) and silver (Ag) layer on back side of wafer were deposited by RF sputtering. Finally, front Ag metal grid electrodes were made on cell with silver paste. The cells with initial thickness of i-layer being 50, 45, 40 and 35 nm have been named as *nip1*, *nip2*, *nip3* and *nip4* respectively. One more cell (*nip0*) was fabricated for comparison without any plasma treatment on c-Si(n) surface and 10 nm thick a-Si:H(i) layer, with same deposition conditions as those of other cells. In order to study influence of HPT on a-Si:H(i) thin films and also to compare and correlate with the properties of i-layer of cells, additional two set of samples having 35 and 50 nm thick a-Si:H(i) films with and without 2 min HPT, but without any top a-Si:H(p) layer, were deposited on identically treated c-Si substrate (c-Si subjected to 10 min HPT before a-Si:H(i) layer in both cases). The optimized deposition conditions for a-Si:H(p) and ITO layer in previous Chapters 4 and 5 were used in fabrication of solar cells.

Ex-situ SE measurements were carried out on cells (*c-Si(n)/a-Si:H(i)/a-Si:H(p)* structure) in the range of 1.5- 5.5 eV at an incident angle of 75° to determine thickness, optical constants such as refractive index, bandgap and microstructure (void, amorphous and crystalline volume

TH-2097_126121019

fractions) of each layer in the solar cell simultaneously (Section 2.2.3, Chapter 2). The FESEM and AFM measurements were performed on a-Si:H(i) films deposited on c-Si substrate without any a-Si:H(p) layer and also on c-Si(n) substrate before and after HPT. The conditions for a-Si:H(i) layer deposition and HPT were identical to those used for fabrication of solar cells. The cell *I-V* characteristics were measured under AM1.5 conditions and 100 mW/cm^2 of incident power density using 100 W Xenon lamp. External Quantum Efficiency (EQE) measurements were performed on the cells in the range of 350-1100 nm. Si photo diode calibrated for global AM1.5 spectra was used as reference to estimate the EQE of the solar cells (Section 2.2.10, Chapter 2).

6.2. Results and discussion

6.2.1. Spectroscopic ellipsometry analysis

SE measurements were performed on *c-Si(n)/a-Si:H(i)/a-Si:H(p)* solar cells to determine the thickness, optical constants such as refractive index, bandgap and microstructure (void, amorphous and crystalline fractions) of each layer in the solar cell simultaneously. Fig. 6.1 (a, b) show the measured spectra of real ($< \varepsilon_1 >$) and imaginary ($< \varepsilon_2 >$) part of pseudo dielectric function (Eq. 2.7) of solar cells and also c-Si substrate as a function of photon energy. The spectra for solar cells are characterised by peaks around 1.7-2.0 eV, which are due to interference of reflected beam from different interfaces (its position depends upon the thickness of different layers) and around 3.6 eV arising from the direct band to band transition in a-Si:H layers. The intensity and broadening of these peaks depend upon the quality of the films. In case of c-Si, the peak and dip in $< \varepsilon_1 >$ and two peaks in $< \varepsilon_2 >$ spectra at 3.4 eV and 4.2 eV correspond to direct band to band transition [5]. Similar features have also been reported for nc-Si:H and μc-Si:H films [6,7].

The $< \varepsilon_2 >$ spectra of *nip1* cells show broad peak at 3.6 eV which is shifted to 3.7 eV in case of *nip2* cells with an increase in its intensity. This broad peak around 3.6 eV corresponds to direct band to band transitions in the a-Si:H films [8–10]. Presence of this peak confirms that both i-layer and p-layer are amorphous in nature for these solar cells. For *nip3* and *nip4* cells, this broad peak has shifted to 3.80 and 3.83 eV respectively. This indicate that the structure of a-Si:H films in these cells has shifted to transition region between amorphous and nano crystalline phase [10–14]. A systematic increase in the amplitude of $< \varepsilon_2 >$ spectra is also observed from *nip1* to *nip4* cells. The amplitude of $< \varepsilon_2 >$ spectra represents the film density, void fraction in films and also type of bonding configuration such as Si-H, Si-H_2 and Si-H_n in

TH-2097_126121019

a-Si:H network [5]. The broadening of curve describes the disorder in the films. Higher amplitude accompanied with a lower broadening correspond to improved density and less disorder in the a-Si:H layers for *nip3* and *nip4* cells.

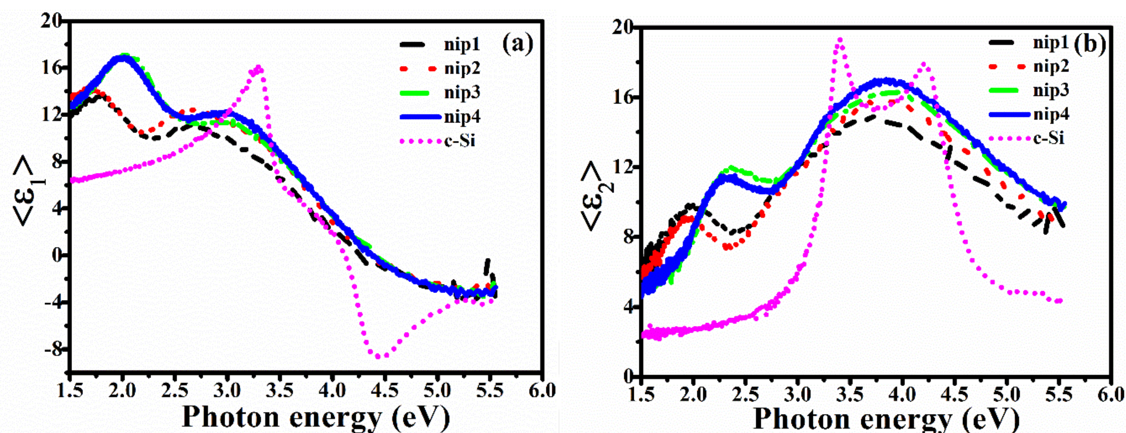

Fig. 6.1. a) Real ($< \varepsilon_1 >$) and b) Imaginary ($< \varepsilon_2 >$) part of pseudo dielectric function measured as a function of photon energy for *nip1* to *nip4* solar cells along with c-Si substrate. In case of c-Si, the spectra are normalised by a factor of two to fit in the range.

The Tauc-Lorentz (TL) model has been applied to calculate the thickness and optical bandgap of a-Si:H (i) and a-Si:H(p) layers of the cells and details of model is given in section 2.2.3.1. Chapter 2 [8,10]. Fig. 6.2a shows the schematic structure of four-layer model (substrate /interface layer 1 (i_1)/ a-Si:H(i) layer/interface layer 2 (i_2)/ a-Si:H(p) layer/air) which has been used to determine the thickness and optical bandgap of each a-Si:H layer in the cells for TL model. The refractive index and extinction coefficient (*n-k*) file from the library of the software has been used to find out thickness of these interface layers. Void (f_v), amorphous (f_a) and crystalline (f_c) volume fractions of each a-Si:H layer and interface layer in the cell have been estimated using BEMA model along with thickness of these layers and detailed description of model is given in Chapter 2 [10,15], the schematic is shown in Fig. 6.2b.

air (a)
a-Si:H(p) layer
Interface layer 2
a-Si:H(i) layer
Interface layer 1
c-Si(n)

air	(b)
a-Si:H(p) layer	f_v, f_a, f_c
Interface layer 2	f_v, f_a, f_c
a-Si:H(i) layer	f_v, f_a, f_c
Interface layer 1	f_v, f_a, f_c
c-Si(n)	

Fig. 6.2: Schematic four-layer model for a) TL and b) BEMA model.

Fig. 6.3 (a-d) show the measured and fitted real $< \varepsilon_1 >$ and imaginary $< \varepsilon_2 >$ part of pseudo dielectric function of *nip1* to *nip4* solar cells with TL model respectively. The fitted TL

TH-2097_126121019

parameters of a-Si:H layer along with estimated thickness of individual layers and band gap of a-Si:H(i) and a-Si:H(p) layers are listed in Table 6.1. The quality of fitting (goodness of fitting) (R^2) is 99% and estimated errors are within 1% of fitted results of all measurements.

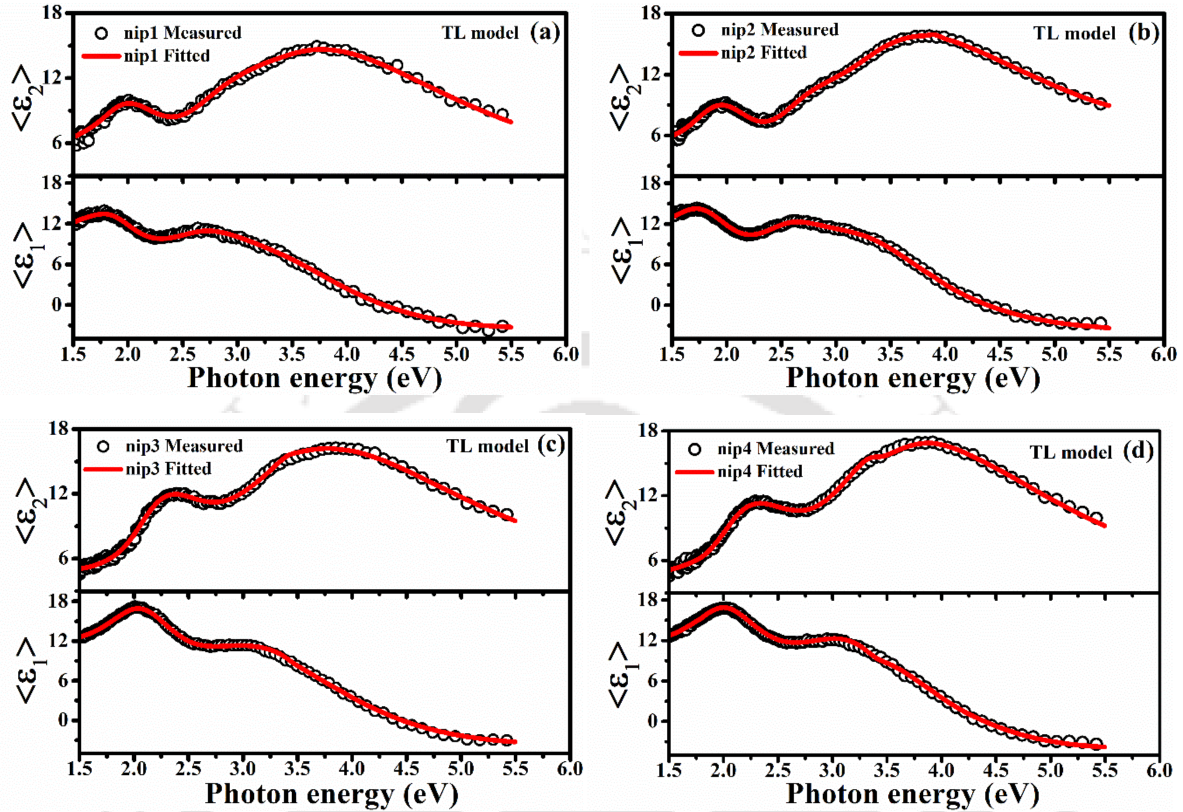

Fig. 6.3: Measured and fitted (TL model) values of real ($<\varepsilon_1>$) and imaginary ($<\varepsilon_2>$) part of pseudo dielectric function as a function of photon energy, (a)-(d) *nip1-nip4* solar cells.

Table 6.1. TL model fitted parameters (A, E_0, C and E_g) and estimated thickness of different layers of *nip1-nip4* solar cells.

	TL model: a-Si:H(i)					TL model: a-Si:H(p)					i_1	i_2
Cell	A (eV)	E_0 (eV)	C (eV)	E_g (eV)	d_i (nm)	A (eV)	E_0 (eV)	C (eV)	E_g (eV)	d_p (nm)	Thickness (nm)	
nip1	212	3.64	2.45	1.79	22.74	232	3.76	2.32	1.84	21.68	1.8	2.1
nip2	217	3.74	2.44	1.80	16.65	234	3.77	2.31	1.84	20.60	1.5	2.2
nip3	234	3.82	2.27	1.82	11.43	235	3.80	2.29	1.85	20.54	1.4	2.0
nip4	237	3.84	2.21	1.82	6.56	236	3.80	2.28	1.85	19.07	1.2	1.6

It is observed that the thickness of a-Si:H(i) layer has decreased from as deposited value of 50, 45, 40 and 35 nm to 22.74, 16.65, 11.43 and 6.56 nm respectively with 2 min HPT prior to the deposition of a-Si:H(p) layer, though not much significant change in thickness of a-Si:H(p) layer is observed. Thickness of the interface (a-Si:H) layers is found to be 1-2 nm for all the cells. Thickness of interface layer i_1 has decreased monotonically from *nip1* to *nip4*, whereas that of i_2 is nearly same for all the cells. SE measurements revealed that 2 min of HPT had

TH-2097_126121019

etched approximately 25±2 nm of i-layer and also changed the quality of films. The small variation in thickness of a-Si:H(i) layer of cells after HPT could be due to variation in thickness of initially deposited i-layer, which was estimated from the deposition rate of films deposited separately.

Fig. 6.4 shows the TL model fitted parameters of a-Si:H(i) layer of cells as a function of estimated thickness of a-Si:H(i) layer. Amplitude parameter (A) increases, whereas the broadening parameter (C) decreases with decrease in the thickness of a-Si:H(i) layer. This can be attributed to improvement in bonding arrangement and microstructure of these films.

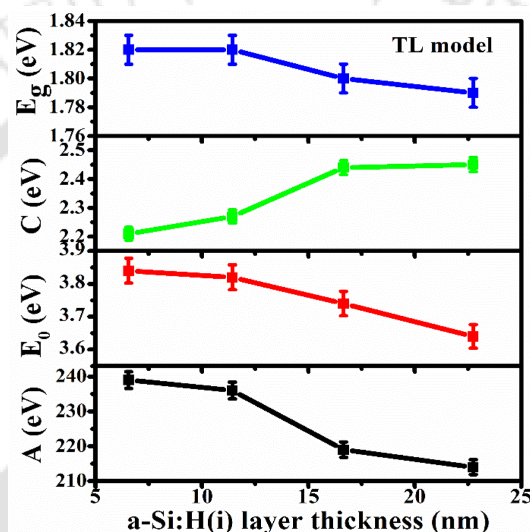

Fig. 6.4. TL model parameters (A, E_0, C and E_g) of a-Si:H(i) layer of *nip1-nip4* cells as a function of estimated thickness of a-Si:H(i) layer.

During HPT, large flux of atomic hydrogen not only etches out the top layers of a-Si:H, but also diffuses deeper in to the film and replaces weak Si-Si and Si-H_2 bonds with strong bonds thus increasing the density of the films and improving the microstructure [9,14,16]. When the thickness of a-Si:H(i) layer is more (*nip1* and *nip2*), atomic hydrogen is not able to reach the underlying layers close to interface to decrease the coordination defects there or replace the weak bond with strong bonds and films are still amorphous. On the other hand, when the thickness of a-Si:H(i) layer is low (*nip3* and *nip4*), the atomic hydrogen diffuses in to underlying layers near the n/i interface and replaces weak bonds with strong bonds resulting in films with less disorder and coordination defects. This is also reflected as a shift in peak energy in $< \varepsilon_2 >$ and an increase in band gap of a-Si:H(i) layer. The TL model fitted parameters of a-Si:H(p) layer of cells do not vary significantly. These values are listed in the Table 6.1. Slight

TH-2097_126121019

changes in TL parameters of a-Si:H(p) layer could be due to improvement in structural ordering of underneath a-Si:H(i) layer after HPT.

Fig. 6.5 (a-d) show the measured and fitted $< \varepsilon_1 >$ and $< \varepsilon_2 >$ spectra of *nip1* to *nip4* solar cells with BEMA model respectively. The estimated thickness and volume fractions of different phases of each layer are given in Table 6.2. It is observed that the thickness of individual layers in two models is almost similar.

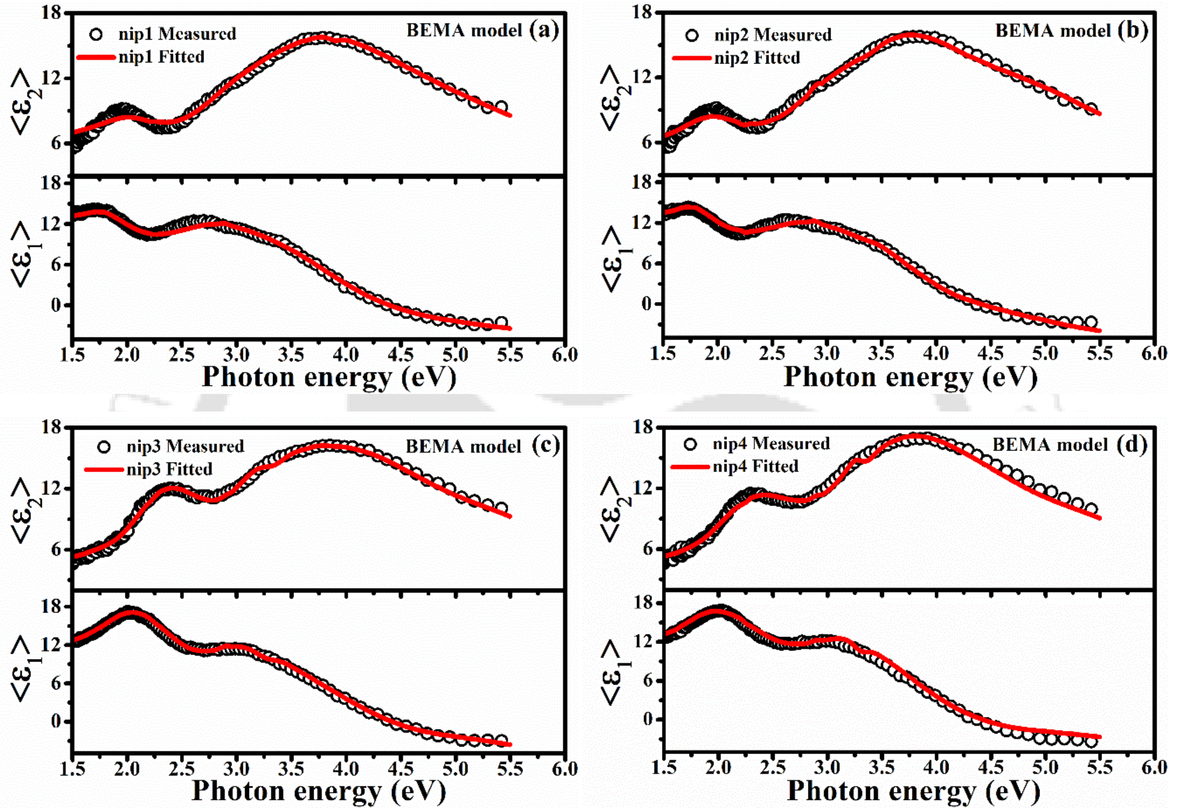

Fig. 6.5: Measured and fitted values of real ($< \varepsilon_1 >$) and imaginary ($< \varepsilon_2 >$) part of pseudo dielectric function as a function of photon energy, (a)-(d) *nip1-nip4* solar cells (fitted with BEMA model).

The void, amorphous and crystalline volume fraction of a-Si:H(i & p) layers of cells are shown in Fig. 6.6(a, b). It is found that void fraction of a-Si:H(i) layer (Fig. 6.6a) has decreased with decrease in its thickness, indicating that higher thickness cells have lower density. The observation is consistent with the lower amplitude of peak in $< \varepsilon_2 >$ spectra for *nip1* and *nip2* cells, which have higher thickness of a-Si:H(i) layer. This decrease in void fraction is accompanied by a simultaneous increase in crystalline fraction of a-Si:H(i) layer. No significant change in the void or crystalline fraction of the a-Si:H (p) layer is observed for these cells (Fig. 6.6b).

TH-2097_126121019

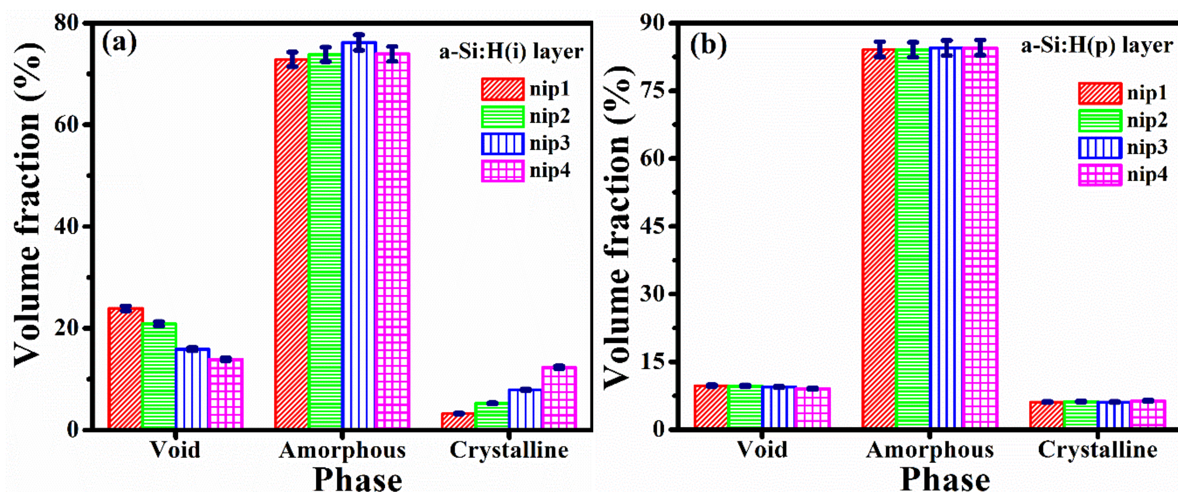

Fig. 6.6. The volume fraction of a-Si:H a) intrinsic and b) p layers of *nip1-nip4* cells.

Fig. 6.7(a, b) show the void, amorphous and crystalline volume fractions of interface layers i_1 and i_2 for *nip1-nip4* cells. For n/i interface, the void and amorphous volume fraction are found to decrease with decrease in thickness of a-Si:H(i) layer along with corresponding increase in crystalline volume fraction (Fig. 6.7a). In case of i/p interface, a small decrease in void fraction is observed (Fig. 6.7b). The void fraction of interfaces has reduced to about 4-6%. This lower void fraction is a result of decrease in interface defect density and concentration of Si-H_2 and other higher hydride bonds, which are responsible for formation of micro voids in the films [17,18]. The micro voids in a-Si:H films cause the light induced degradation effect in a-Si:H films [19,20]. A decrease in its density upon 2 min HPT is expected to improve the stability of these cells against exposure to light. These observations indicate that HPT is quite beneficial for n/i, & i/p interfaces by reducing the void fraction of these layers.

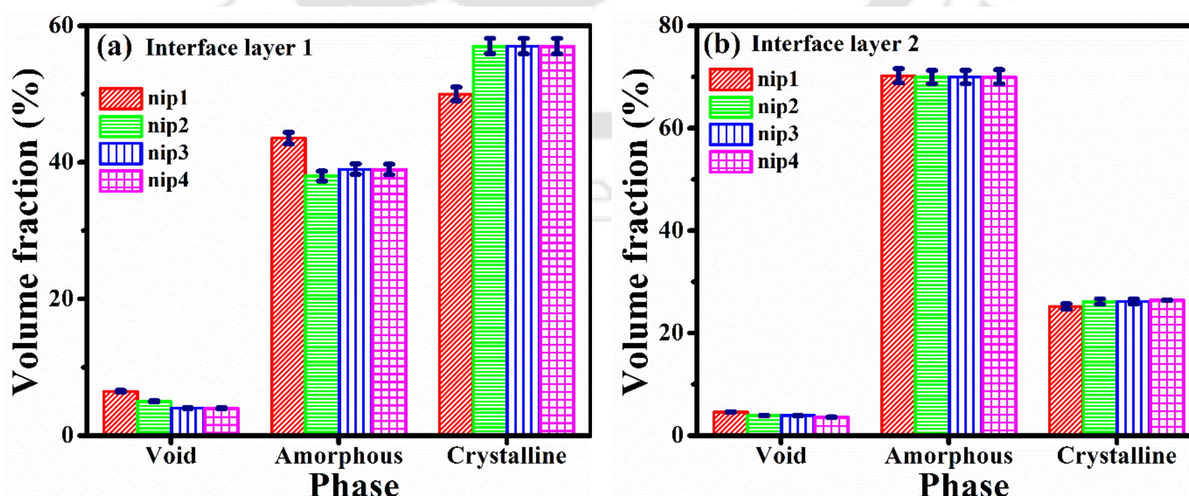

Fig. 6.7(a, b). The volume fraction of interface (i_1, i_2) layers of *nip1-nip4* cells.

TH-2097_126121019

Table 6.2. Thickness (d_{layer}), void (f_v), amorphous (f_a) and crystalline f_c fraction of layers of cells calculated from SE measurements.

Cell	d_{layer} (nm)	f_v (%)	f_a (%)	f_c (%)	layer
nip1	20.85	9.73	84.16	6.10	p
	2.34	4.57	70.24	25.18	i_2
	21.03	23.91	72.84	3.24	i
	1.72	6.47	43.53	50.0	i_1
nip2	21.90	9.69	84.10	6.21	p
	2.20	3.90	69.96	26.14	i_2
	16.37	20.9	73.83	5.27	i
	1.46	5.01	37.98	57.02	i_1
nip3	21.85	9.44	84.46	6.10	p
	2.01	3.90	69.96	26.14	i_2
	11.78	15.89	76.18	7.92	i
	1.36	4.01	38.97	57.02	i_1
nip4	21.91	9.07	84.55	6.38	p
	1.61	3.59	70.0	26.41	i_2
	6.16	13.91	73.84	12.25	i
	1.22	4.0	38.97	57.02	i_1

In order to study influence of HPT on a-Si:H(i) films and also to compare the properties of these films with i-layer of cells, SE measurements were performed on identically deposited 35 and 50 nm thick a-Si:H(i) films before and after exposure to 2 min H_2 plasma. Fig. 6.8(a-d) show the measured spectra of $< \varepsilon_1 >$ and $< \varepsilon_2 >$ of 35 and 50 nm thick films before and after 2 min HPT respectively. The $< \varepsilon_2 >$ spectra for both the films without any HPT is characterised by a peak at 3.5 eV corresponding to the amorphous nature of the films. The amplitude of the peak is also nearly same for both the films. After 2 min of HPT, a change in the spectra of 35 nm film has been observed whereas that of 50 nm thick film spectra remained nearly same as before. In addition to the enhancement of amplitude of $< \varepsilon_2 >$ spectra, a shoulder near 4.1 eV appeared after 2 min HPT of 35 nm thick film which indicates the formation of nanocrystalline phase. To estimate thickness and bandgap of these a-Si:H(i) films, TL and BEMA model have been used; the schematic three layer model is shown in Fig. 6.9.

TH-2097_126121019

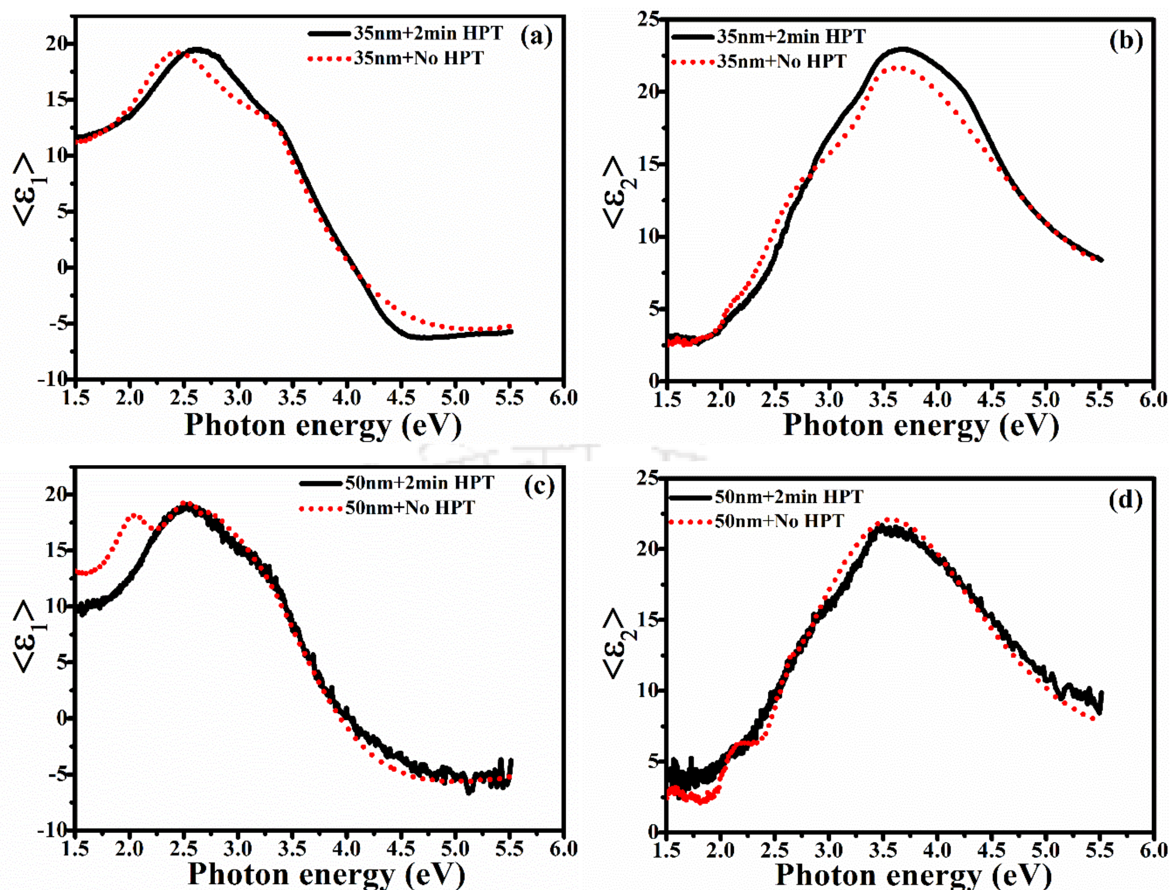

Fig. 6.8(a-d). Real ($<\varepsilon_1>$) and Imaginary ($<\varepsilon_2>$) part of pseudo dielectric function measured as a function of photon energy for 35 and 50 nm thick a-Si:H(i) films before and after 2 min HPT.

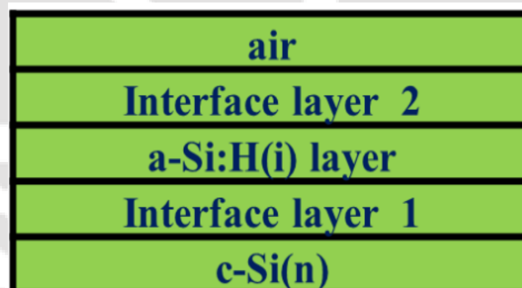

Fig. 6.9. Schematics model for TL and BEMA fitting.

Fig. 6.10 (a-d) show the measured and fitted (TL model) spectra of $<\varepsilon_1>$ and $<\varepsilon_2>$ as a function of photon energy for 35 and 50 nm thick a-Si:H(i) films before and after 2 min HPT. The estimated values of bandgap and thickness of a-Si:H(i) and interface layers are given in the Table 6.3. These values for hydrogen plasma treated films listed in Table 6.3 match well with those for corresponding layers in solar cells given in Table 6.1.

TH-2097_126121019

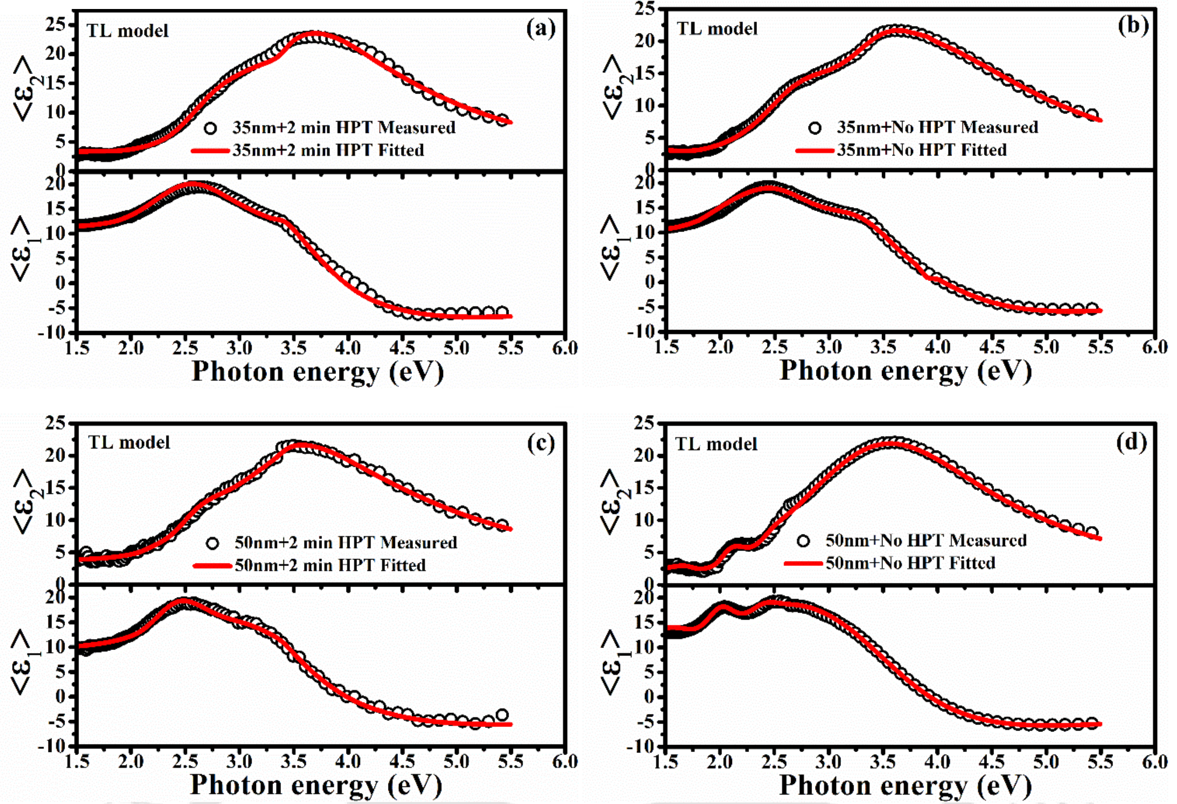

Fig. 6.10(a-d): Measured and fitted (TL model) values of $<\varepsilon_1>$ and $<\varepsilon_2>$ as a function of photon energy for 35 and 50 nm thick a-Si:H(i) films before and after 2 min HPT.

Table 6.3. TL model fitted parameters $(A, E_0, C$ and $E_g)$ and estimated thickness of interface and a-Si:H(i) layers.

	TL model: a-Si:H(i)					i_1	i_2
Sample	A (eV)	E_0 (eV)	C (eV)	E_g (eV)	Thickness (nm)	Thickness (nm)	Thickness (nm)
35nm + 2min HPT	232	3.83	2.30	1.82	7.11	1.3	1.9
35nm + No HPT	210	3.56	2.45	1.80	33.0	1.4	2.0
50nm + 2min HPT	215	3.45	2.43	1.79	22.25	2.6	1.8
50nm + No HPT	219	3.55	2.54	1.79	47.33	1.5	1.2

Fig. 6.11(a-d) show measured and fitted (BEMA model) spectra of real ($<\varepsilon_1>$) and imaginary ($<\varepsilon_2>$) part of pseudo dielectric function as a function of photon energy for 35 and 50 nm thick a-Si:H(i) films before and after 2 min HPT. The estimated thickness, void, amorphous and crystalline volume fraction of a-Si:H(i) and interface layers are given in the Table 6.4. The bandgap, thickness, void, amorphous and crystalline volume fractions of a-Si:H(i) films and interfaces are very consistent with those for a-Si:H(i) and interface layers of cells (Table 6.2).

TH-2097_126121019

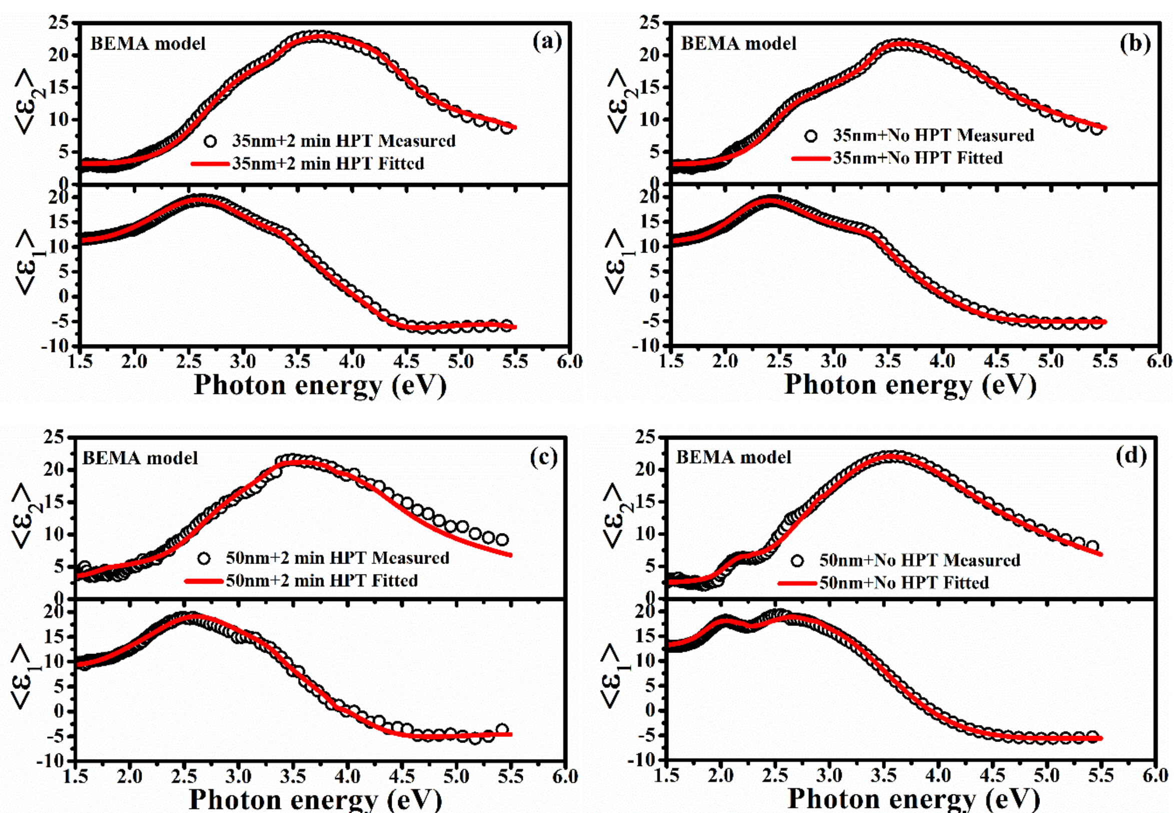

Fig. 6.11(a-d): Measured and fitted (BEMA model) values of $<\varepsilon_1>$ and $<\varepsilon_2>$ a function of photon energy for 35 and 50nm thick a-Si:H(i) films before and after 2 min HPT.

Table 6.4. Thickness, void, amorphous and crystalline fraction of interface and a-Si:H(i) layers calculated from BEMA model.

Sample	d_{layer} (nm)	f_v (%)	f_a (%)	f_c (%)	layer
35nm + 2min HPT	1.81	8.57	60.22	31.18	i_2
	6.91	13.67	74.56	11.77	i
	1.12	5.05	40.04	54.90	i_1
35nm + No HPT	1.70	25.01	71.82	3.08	i_2
	33.0	20.90	75.05	3.75	i
	1.54	4.85	42.11	53.01	i_1
50 nm + 2min HPT	2.55	10.98	66.74	22.28	i_2
	22.25	24.43	72.60	2.92	i
	1.75	6.03	42.40	51.57	i_1
50nm + No HPT	1.22	26	72.57	1.43	i_2
	47.17	25.75	71.60	2.80	i
	1.59	5.40	42.45	52.15	i_1

6.2.2. FESEM morphology studies

In order to understand the influence of H_2 plasma treatment on the surface of the c-Si(n) absorber wafer and a-Si:H layers, the FESEM was performed on c-Si(n) and a-Si:H(i) films.

TH-2097_126121019

Fig. 6.12 (a-d) show the FESEM image of c-Si(n) and a-Si:H(i) layer before and after H_2 plasma treatment respectively. From these figures, one can clearly see that the surface morphology of c-Si(n) wafer has not changed even after 10 min H_2 plasma treatment (Fig. 6.12b); though it might have etched out the top layer of c-Si wafer and passivated Si dangling bonds by forming strong Si-H bonds on the surface [21]. In case of a-Si:H layer, a fraction of amorphous phase has been etched out and small nano sized grains have formed by 2 min HPT (Fig. 6.12d) [14,22]. The growth of small nano size grains help in growth of more ordered structure during subsequent growth of a-Si:H(p) layer near the transition region of amorphous and nanocrystalline phase with lower void volume fraction, which is confirmed by SE measurements.

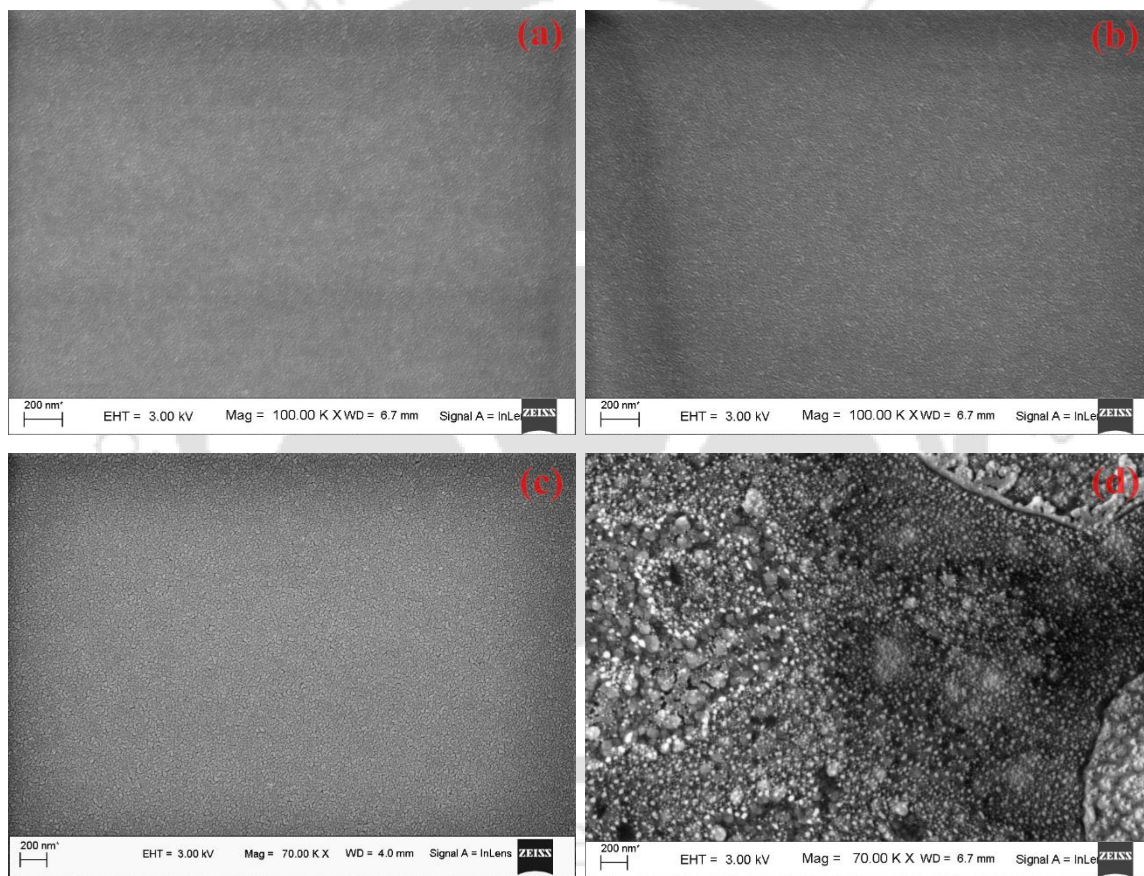

Fig. 6.12. FESEM image of i) c-Si(n) substrate a) before and b) after 10 min H_2 plasma; ii) a-Si:H(i) films (35nm thick) on c-Si c) before and d) after 2 minutes H_2 plasma treatment.

6.2.3. AFM morphology studies

The surface morphology of c-Si and a-Si:H films with and without HPT was also studied using AFM and shown in Fig. 6.13(a-d). The RMS roughness values obtained for c-Si substrate before and after 10 min HPT are found to be 0.29 nm and 0.43 nm respectively. The values for

TH-2097_126121019

a-Si:H(i) films before and after 2 min HPT are 0.36 nm and 0.62 nm respectively. It is observed that surface of the substrate is smooth enough for the growth of the a-Si:H films.

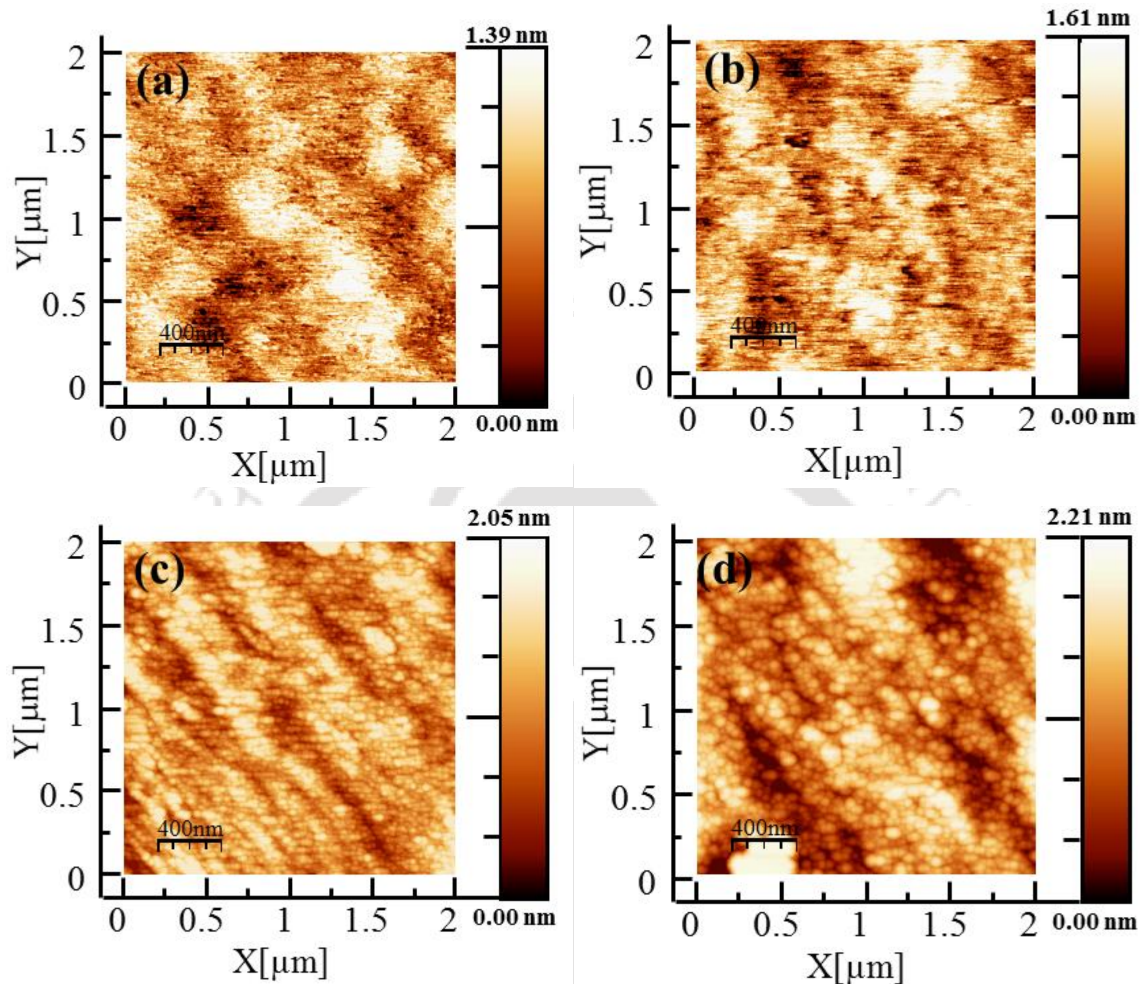

Fig. 6.13. AFM image of i) c-Si(n) substrate a) before and b) after 10 min H_2 plasma; ii) a-Si:H(i) films (35nm thick) on c-Si c) before and d) after 2 minutes H_2 plasma treatment.

6.2.4. Current-Voltage measurement

Fig. 6.14 shows the dark current density-voltage (J-V) characteristics of the *nip0*, *nip2*, *nip3* and *nip4* cells. The reverse saturation current density (J_0) for *nip0* cell is more than one order of magnitude higher than that of *nip3* and *nip4* cells. For *nip2* cell, J_0 is more than that of *nip4* cell, though it is smaller compared to *nip0* cell. The lowest J_0 is obtained for *nip3* cell. The forward to reverse bias current density ratio is also higher for *nip3* and *nip4* cells as compared to that for *nip0* and *nip2* cells. The high injection region started around 700 mV for *nip3* and *nip4* cells.

TH-2097_126121019

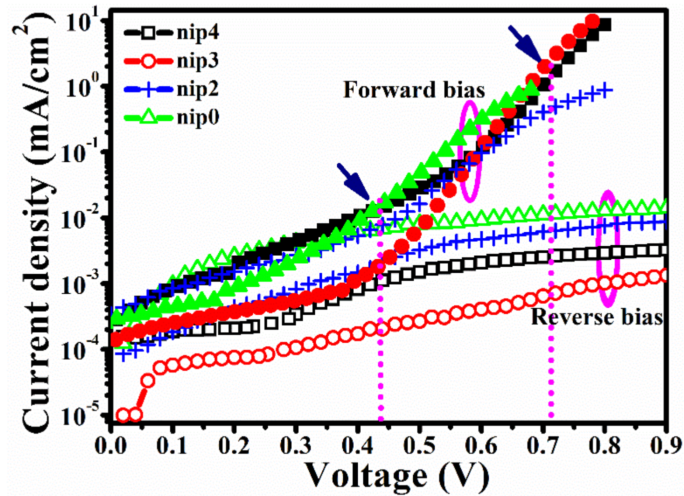

Fig. 6.14. Dark *J-V* characteristics of *nip0*, *nip2, nip3* and *nip4* cells (open symbols represent reverse bias, whereas filled symbols represent forward bias).

Fig. 6.15 show the *J-V* characteristics of c-Si/a-Si:H based hetero-junction *nip1-nip4* solar cells under AM1.5 illumination. The dark *J-V* characteristic of *nip3* and *nip4* cells is also shown in Fig. 6.15. For comparison, the *J-V* characteristics under illumination of *nip*0 cell, which was not subjected to any hydrogen plasma and having 10 nm thick a-Si:H(i) layer, is also included in this figure. The values of J_{sc}, V_{oc}, FF (Eq. 2.29) and efficiency (η) (Eq. 2.30) for all the cells are estimated and listed in Table 6.5. A systematic increase in these values are observed from *nip0* to *nip4* cells. This improvement in J_{sc} and V_{oc} values is due to the systematic decrease in thickness of a-Si:H(i) layer, reduction in void fractions of n/i and i/p interface layers and overall improvement in microstructure of a-Si:H layers, which is reflected as a shift in position of peak $< \varepsilon_2 >$ in SE spectra [22]. A crossover of *J-V* characteristic in dark and under illumination is observed around 700 mV for the *nip3* and *nip*4 cells. For these cells, the dark current density near V_{oc} is slightly low compared to J_{sc} value for corresponding cells.

The open circuit voltage for *nip3* and *nip 4* cells are 711 and 703 mV respectively, which are best among the values (628-635 mV) reported so far for single sided hetero-junction solar cells on n type c-Si [23–26]. To the best of our knowledge, the highest V_{oc} of 652 mV has been reported for single side c-Si/a-Si:H on p-type c-Si(FZ) by Wang et.al [27,28]. Though V_{oc} as high as 750 mV has been reported on double side heterojunction cells on thin n-type c-Si substrates [29]. For *nip2* cell, the V_{oc} is 645 mV, which is close to the values reported for such cells. For this cell *(nip2*), though J_{sc} is not very different than that of *nip3* and *nip4* cell, the V_{oc} is low due to relatively higher value of J_0.

TH-2097_126121019

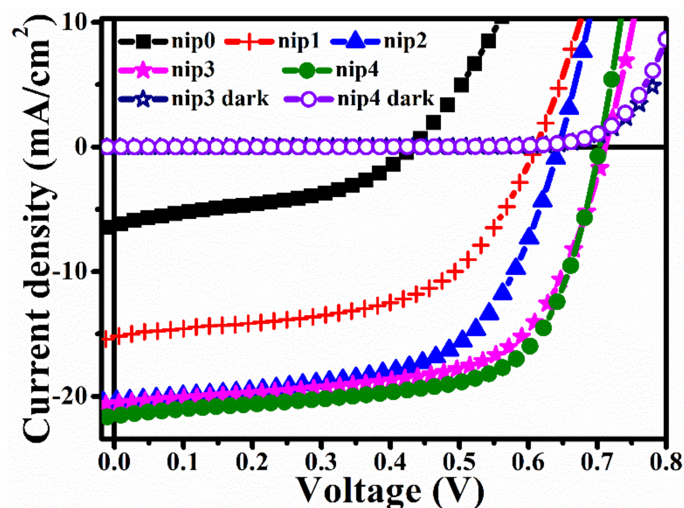

Fig. 6.15. *J-V* characteristics of c-Si/a-Si:H heterojunction solar cells.

It is very challenging to achieve such high open circuit voltage with one side c-Si/a-Si:H solar cells. However, in our case, it could be achieved since 10 min H_2 plasma treatment on c-Si(n) absorber layer has passivated most of the surface dangling bonds and reduced the defect density at n/i interface. This less defective interface layer further helped the growth of a-Si:H layer having an improved microstructure [30,31]. The 2 min H_2 plasma treatment on a-Si:H(i) layer has also improved the n/i interface when a-Si:H(i) layer thickness was low (*nip3* and *nip4* cells) and atomic hydrogen could diffuse to the interface layer and removed the weak Si-Si bonds. The hydrogen plasma treatment of a-Si:H(i) layer also improved the i/p interface by removing the weak Si-Si bonds and surface defects before the a-Si:H(p) layer was deposited [31,32]. It can be seen from Table 6.2, that for *nip3* and *nip4* cells, the void fraction of all the layers is significantly low compared to that for *nip1* and *nip2* cells. This has resulted in reduced recombination losses of photo generated carriers for *nip3* and *nip4* cells having good interfaces and transport properties [33]. The *nip1* and *nip2* cells have low V_{oc} values, though these values are close to those reported for single side SHJ solar cells, due to higher density of defects at interface and also in bulk of the layers as the thickness of a-Si:H layer is still high. The short circuit current density value has increased with decrease in thickness of a-Si:H(i) layer due to lower absorption of photons in the a-Si:H(i) layer and also smaller path length of photo generated carriers to reach metal contacts [23,34]. Our best *FF* values are 0.63 and 0.66 corresponding to the *nip3* and *nip4* cells respectively. The *FF* mainly depends on shunt and series resistance and void fraction in the different layers and also on micro voids and defects in band tail states [35–37]. The interface and a-Si:H layers of *nip3* and *nip4* cells have less void fraction as estimated from SE. In case of *nip1* and *nip2*, the thickness of a-Si:H(i) layer as well as void fraction are more, which has increased the series resistance of the device and a lower

TH-2097_126121019

value of FF is observed. The J_{sc}, V_{oc}, FF and η values of *nip0* cell are very low compared to plasma treated cells due to unpassivated surface, defective interface and a-Si:H(i) layers. It is found that the efficiency and FF of cells are directly related to the amplitude of $< \varepsilon_2 >$ spectra of cells (Fig. 6.16) which is in agreement with the reports in literature [37]. The shunt (R_{sh}) and series (R_s) resistance values are estimated from the *J-V* curve of the cells using Eq. 2.31 and Eq. 2.32 and listed in the Table 6.5. The series resistance has decreased, whereas shunt resistance has increased from *nip0* to *nip4* cells due to reduction in thickness of a-Si:H(i) layer and micro voids in the cells which has created path to shunting of device.

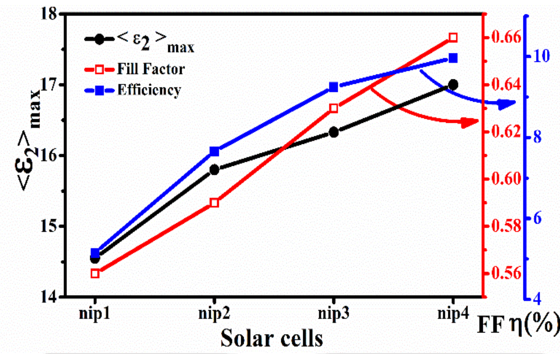

Fig. 6.16. The maximum of $< \varepsilon_2 >$ spectra, fill factor and efficiency of *nip1-nip4* cells.

Table 6.5. The estimated solar cell parameters for *nip1-nip4* c-Si/a-Si:H heterojunction solar cells.

cell	J-V measurement								EQE measurement	
	J_{sc} (mA/cm^2)	V_{oc} (mV)	J_{max} (mA/cm^2)	V_{max} (mV)	FF	η (%)	R_{sh} (Ωcm^2)	R_s (Ωcm^2)	J_{sc} (mA/cm^2)	η (%)
nip4	21.53	703	17.71	563	0.66	9.97	235	4.4	20.87	9.68
nip3	20.64	711	16.72	553	0.63	9.25	233	5.7	19.07	8.55
nip2	20.0	645	15.20	504	0.59	7.66	223	6.5	18	6.86
nip1	15.15	614	11.33	456	0.56	5.15	187	10.3	14	4.81
nip0	6.27	436	3.70	305	0.42	1.14	115	26.3	6.94	1.27

6.2.5. Quantum efficiency measurement

Fig. 6.17 shows the EQE of c-Si/a-Si:H heterojunction *nip0-nip4* solar cells. The EQE of the cells was estimated using Eq. 2.33. The highest quantum efficiency of *nip1-nip4* cells is around 75-80%. The *nip0* cell, which was directly fabricated on c-Si without any hydrogen plasma treatment, shows a very poor response with EQE values less than 30%. For *nip1-nip4* cells, both low as well as high wavelength response has improved as the thickness of a-Si:H(i) layer is reduced. The enhanced response in the low wavelength region with decrease in thickness of a-Si:H(i) layer corresponds to better passivation of interfaces and less absorption in i-layers. The EQE is around 75-80% over a broad range of wavelength (550-850 nm) for *nip4* cell,

which has the least thickness of a-Si:H(i) layer. The EQE has increased on either side of the wavelengths and is more than 50% at 450 and 900 nm respectively. This is a signature of the good quality abrupt junction [38], which has also resulted in higher V_{oc} for these cells. This good response of spectra is mainly due to reduction in defect density and void fraction at n/i, p/i interface and a-Si:H layers, which are confirmed by SE measurements. The EQE of *nip3* cell is slightly lower (72-76%) as compared to *nip4* cell. The blue, red response and broadening of EQE of *nip3* spectra is also slightly less as compared to that of *nip4* cell. This may be attributed to slightly higher thickness of a-Si:H(i) layer [23]. The *nip1* and *nip2* cells show high EQE of 80% in the range of 550-700 nm which has dropped sharply at lower and higher wavelength regions. The broadening of spectra is less as compared to *nip3* and *nip4* cells. The poor response of these cells (*nip1* and *nip2*) in the short and long wavelength range is mainly due to recombination losses of photo generated carries at i/p and n/i interface, absorption of photons in the a-Si:H(i) layer and reduced charge carrier collection in these cells. In the intermediate wavelength (550-700 nm) range, the possible reason for better performance of *nip2* cell could be due to improved microstructure of a-Si:H(i) layer after HPT. The electron-hole pair generated by the absorption of photons in relatively thick i-layer could separate and reached the respective interface/electrodes without recombining in the i-layer. In case of *nip3* and *nip4* cells, where the i-layer thickness is less, the mid-range photons are mostly absorbed in c-Si near i/n interface. The integrated short circuit current density of the *nip0-nip4* cells was calculated using Eq. 2.35 from EQE measurement and values are listed in Table 6.5. The efficiency of the cells was again calculated with the J_{sc} values obtained from EQE spectra and V_{oc}, FF values from *J-V* measurements. The estimated efficiency of cells is also listed in Table 6.5. These calculated value of efficiency of cells are well matched with those estimated from *J-V* measurements.

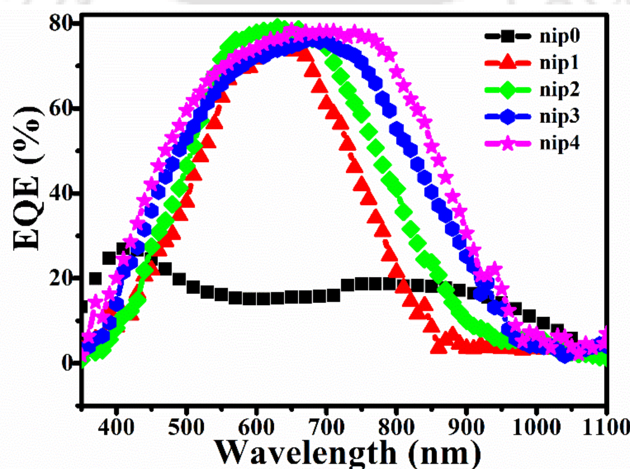

Fig. 6.17. EQE spectra of c-Si/a-Si:H heterojunction solar cells.

TH-2097_126121019

6.3. Conclusion

c-Si/a-Si:H single side heterojunction solar cells with open circuit voltage as high as 711 mV were fabricated successfully. This high V_{oc}, which is highest among those reported so far for single side c-Si/a-Si:H heterojunction cells, could be achieved because of improvement in microstructure of a-Si:H(i) layer and interface layers by the hydrogen plasma treatment of this layer prior to the deposition of a-Si:H(p) layer. The SE studies confirmed that H_2 plasma treatment of a-Si:H(i) layer not only etched out the significant amorphous fraction of this layer but also reduced the void fraction. The hydrogen plasma treatment has also passivated and improved the n/i, i/p interfaces and a-Si:H layers without deteriorating the electronic quality of layers. The microstructure of a-Si:H(i) layer move to near transition region of amorphous to crystalline phase. This is confirmed by SE, as the peak energy is shifted towards higher energy side of 3.83 eV. We found that the efficiency and fill factor of cells have a direct correlation with the amplitude of $< \varepsilon_2 >$ spectra of cells. Our results suggest H_2 plasma treatment as an effective approach to achieve surface passivation and improve the open circuit voltage of c-Si/a-Si:H heterojunction solar cells.

6.4. References

[1] W. Kern , Puotinen D A, Cleaning solutions based on hydrogen peroxide for use in silicon semiconductor technology, RCA Rev. 31 (1970) 187–206.

[2] Werner Kern, The Evolution of Silicon Wafer Cleaning Technology, J. Electrochem. Soc. 137 (1990) 1887–1892. doi:10.1149/1.2086825.

[3] Y. Tsunomura, Y. Yoshimine, M. Taguchi, T. Baba, T. Kinoshita, H. Kanno, H. Sakata, E. Maruyama, M. Tanaka, Twenty-two percent efficiency HIT solar cell, Sol. Energy Mater. Sol. Cells. 93 (2009) 670–673. doi:10.1016/j.solmat.2008.02.037.

[4] T. Mishima, M. Taguchi, H. Sakata, E. Maruyama, Development status of high-efficiency HIT solar cells, Sol. Energy Mater. Sol. Cells. 95 (2011) 18–21. doi:10.1016/j.solmat.2010.04.030.

[5] T. Yuguchi, Y. Kanie, N. Matsuki, H. Fujiwara, Complete parameterization of the dielectric function of microcrystalline silicon fabricated by plasma-enhanced chemical vapor deposition, J. Appl. Phys. 111 (2012) 083509. doi:10.1063/1.4704158.

[6] L.R. Dahal, J. Li, J.A. Stoke, Z. Huang, A. Shan, A.S. Ferlauto, C.R. Wronski, R.W. Collins, N.J. Podraza, Applications of real-time and mapping spectroscopic ellipsometry for process development and optimization in hydrogenated silicon thin-film photovoltaics technology, Sol. Energy Mater. Sol. Cells. 129 (2014) 32–56. doi:10.1016/j.solmat.2014.01.028.

TH-2097_126121019

[7] R.W. Collins, A.S. Ferlauto, G.M. Ferreira, C. Chen, J. Koh, R.J. Koval, Y. Lee, J.M. Pearce, C.R. Wronski, Evolution of microstructure and phase in amorphous, protocrystalline, and microcrystalline silicon studied by real time spectroscopic ellipsometry, Sol. Energy Mater. Sol. Cells. 78 (2003) 143–180. doi:10.1016/S0927-0248(02)00436-1.

[8] G.E.Jellison and F.A. Modine, Parameterization of the optical functions of amorphous materials in the interband region, Appl. Phys. Lett. 69 (1996) 371–373. doi:10.1063/1.118064.

[9] S. Kageyama, M. Akagawa, H. Fujiwara, Dielectric function of a-Si:H based on local network structures, Phys. Rev. B. 83 (2011) 195205. doi:10.1103/PhysRevB.83.195205.

[10] H. Fujiwara, Spectroscopic Ellipsometry Principles and Applications, Willey Publ. (2007). doi:10.1002/9780470060193,ISBN:9780470016084.

[11] A. Fontcuberta i Morral and P. Roca i Cabarrocas, C.Clerc, Structure and hydrogen content of polymorphous silicon thin films studied by spectroscopic ellipsometry and nuclear measurements, Phys. Rev. B. 69 (2004) 125307. doi:10.1103/PhysRevB.69.125307.

[12] H. Zhang, X. Zhang, G. Hou, C. Wei, J. Sun, X. Geng, S. Xiong, Y. Zhao, The microstructure and optical properties of p-type microcrystalline silicon thin films characterized by ex-situ spectroscopic ellipsometry, Thin Solid Films. 521 (2012) 17–21. doi:10.1016/j.tsf.2012.03.081.

[13] Y.-H. Chu, C.-C. Lee, T.-H. Chang, S.-Y. Chang, J.-Y. Chang, T. Li, I.-C. Chen, Investigation of hydrogenated amorphous silicon as passivation layer by high density plasma, Thin Solid Films. 570 (2014) 591–594. doi:10.1016/j.tsf.2014.03.064.

[14] F.I. Morral, P. Roca i Cabarrocas, Etching and hydrogen diffusion mechanisms during a hydrogen plasma treatment of silicon thin films, J. Non. Cryst. Solids. 299–302 (2002) 196–200. doi:10.1016/S0022-3093(01)01001-8.

[15] D.E. Aspnes, Optical properties of thin films, Thin Solid Films. 89 (1982) 249–262. doi:10.1016/0040-6090(82)90590-9.

[16] S. Kageyama, M. Akagawa, H. Fujiwara, Ellipsometry characterization of a-Si:H layers for thin-film solar cells, J. Non. Cryst. Solids. 358 (2012) 2257–2259. doi:10.1016/j.jnoncrysol.2011.12.042.

[17] F. Wang, X. Zhang, L. Wang, Y. Jiang, C. Wei, S. Xu, Y. Zhao, Improved amorphous/crystalline silicon interface passivation for heterojunction solar cells by low-temperature chemical vapor deposition and post-annealing treatment, Phys. Chem. Chem. Phys. 16 (2014) 20202. doi:10.1039/C4CP02212B.

[18] A.H.M. Smets, W.M.M. Kessels, M.C.M. Van de Sanden, Vacancies and voids in hydrogenated amorphous silicon, Appl. Phys. Lett. 82 (2003) 1547–1549. doi:10.1063/1.1559657.

TH-2097_126121019

[19] K.L. M.Fehr, A. Schnegg, B. Rech, O. Astakhov, F. Finger, R. Bittl, C. Teutloff, Metastable Defect Formation at Microvoids Identified as a Source of Light-Induced Degradation in a-Si:H, Phys. Rev. Lett. 112 (2014) 066403. doi:10.1103/PhysRevLett.112.066403.

[20] D.L. Staebler, C.R. Wronski, Reversible conductivity changes in discharge-produced amorphous Si, Appl. Phys. Lett. 31 (1977) 292. doi:10.1063/1.89674.

[21] A. Hadjadj, F. Larbi, M. Gilliot, P. Roca I Cabarrocas, Etching of a-Si:H thin films by hydrogen plasma: A view from in situ spectroscopic ellipsometry, J. Chem. Phys. 141 (2014) 084708. doi:10.1063/1.4893558.

[22] A. Hadjadj, N. Pham, P. Roca I Cabarrocas, O. Jbara, G. Djellouli, Ellipsometry investigation of the amorphous-to-microcrystalline transition in a-Si:H under hydrogen-plasma treatment, J. Appl. Phys. 107 (2010) 083509. doi:10.1063/1.3393273.

[23] H. Fujiwara, M. Kondo, Effects of a-Si:H layer thicknesses on the performance of a-Si:H/c-Si heterojunction solar cells, J. Appl. Phys. 101 (2007) 054516. doi:10.1063/1.2559975.

[24] H. Fujiwara, M. Kondo, Impact of epitaxial growth at the heterointerface of a-Si:H/c-Si solar cells, Appl. Phys. Lett. 90 (2007) 2005–2008. doi:10.1063/1.2426900.

[25] H. Fujiwara, T. Kaneko, M. Kondo, Optimization of interface structures in crystalline silicon heterojunction solar cells, Sol. Energy Mater. Sol. Cells. 93 (2009) 725–728. doi:10.1016/j.solmat.2008.09.007.

[26] W.K. Oh, S.Q. Hussain, Y.J. Lee, Y. Lee, S. Ahn, J. Yi, Study on the ITO work function and hole injection barrier at the interface of ITO/a-Si:H(p) in amorphous/crystalline silicon heterojunction solar cells, Mater. Res. Bull. 47 (2012) 3032–3035. doi:10.1016/j.materresbull.2012.04.106.

[27] T.H. Wang, M.R. Page, E. Iwaniczko, Q. Wang, Y. Xu, Y. Yan, L. Roybal, D. Levi, R. Bauer, H.M. Branz, 17.5% p-Type Silicon Heterojunction Solar Cells with HWCVD a-Si : H as the Emitter and Back Contact, in: NREL/CP-520-38942, 2005: pp. 1–5. doi:https://digital.library.unt.edu/ark:/67531/metadc892630/m1/3/.

[28] T.H. Wang, E. Iwaniczko, M.R. Page, Q. Wang, Y. Xu, Y. Yan, D. Levi, L. Roybal, R. Bauer, H.M. Branz, High-Efficiency Silicon Heterojunction Solar Cells by HWCVD, in: IEEE 4th World Conf., 2006: pp. 1439–1442. doi:10.1109/WCPEC.2006.279723.

[29] M. Taguchi, A. Yano, S. Tohoda, K. Matsuyama, Y. Nakamura, T. Nishiwaki, K. Fujita, E. Maruyama, 24.7% Record efficiency HIT solar cell on thin silicon wafer, IEEE J. Photovoltaics. 4 (2014) 96–99. doi:10.1109/JPHOTOV.2013.2282737.

[30] M. Taguchi, A. Terakawa, E. Maruyama, M. Tanaka, Obtaining a higher Voc in HIT cells, Prog. Photovoltaics Res. Appl. 13 (2005) 481–488. doi:10.1002/pip.646.

[31] A. Descoeudres, L. Barraud, S. De Wolf, B. Strahm, D. Lachenal, C. Guérin, Z.C. Holman, F. Zicarelli, B. Demaurex, J. Seif, J. Holovsky, C. Ballif, Improved

TH-2097_126121019

amorphous/crystalline silicon interface passivation by hydrogen plasma treatment, Appl. Phys. Lett. 99 (2011) 123506. doi:10.1063/1.3641899.

[32] M. Mews, T.F. Schulze, N. Mingirulli, L. Korte, Hydrogen plasma treatments for passivation of amorphous-crystalline silicon-heterojunctions on surfaces promoting epitaxy, Appl. Phys. Lett. 102 (2013) 122106. doi:10.1063/1.4798292.

[33] F. Meng, L. Shen, J. Shi, L. Zhang, J. Liu, Y. Liu, Z. Liu, Role of the buffer at the interface of intrinsic a-Si:H and p-type a-Si:H on amorphous/crystalline silicon heterojunction solar cells, Appl. Phys. Lett. 107 (2015) 223901.

[34] M.R. Page, E. Iwaniczko, Y.Q. Xu, L. Roybal, F. Hasoon, Q. Wang, R.S. Crandall, Amorphous/crystalline silicon heterojunction solar cells with varying i-layer thickness, Thin Solid Films. 519 (2011) 4527–4530. doi:10.1016/j.tsf.2011.01.293.

[35] H. Sonobe, A. Sato, S. Shimizu, T. Matsui, M. Kondo, A. Matsuda, Highly stabilized hydrogenated amorphous silicon solar cells fabricated by triode-plasma CVD, Thin Solid Films. 502 (2006) 306–310. doi:10.1016/j.tsf.2005.07.300.

[36] Q. Wang, Fill factor related issues in hydrogenated amorphous Si solar cells, Sol. Energy Mater. Sol. Cells. 129 (2014) 64–69. doi:10.1016/j.solmat.2014.02.015.

[37] S.Y. Lee, J.H. Shim, D.J. You, S.W. Ahn, H.M. Lee, The novel usage of spectroscopic ellipsometry for the development of amorphous Si solar cells, Sol. Energy Mater. Sol. Cells. 95 (2011) 142–145. doi:10.1016/j.solmat.2010.04.054.

[38] M. Agarwal, A. Pawar, N. Wadibhasme, R. Dusane, Controlling the c-Si/a-Si:H interface in silicon heterojunction solar cells fabricated by HWCVD, Sol. Energy. 144 (2017) 417–423. doi:10.1016/j.solener.2017.01.039.

TH-2097_126121019

Chapter 7

Influence of Boron Doping and Thickness of a-Si:H(p) Layer on the Performance of c-Si/a-Si:H Heterojunction Solar Cells

In this chapter, influence of boron doping concentration and thickness of a-Si:H(p) layer on the performance of the c-Si/a-Si:H heterojunction solar cells has been presented. High open circuit voltage of 711 mV and efficiency of 10% for single side c-Si(n)/a-Si:H(p) solar cells are presented in the previous Chapter 6. This efficiency is still low compared to those reported silicon heterojunction solar cells. However, this V_{oc} is almost comparable with double side SHJ solar cells [1–6]. Low doping of a-Si:H(p) layer could not provide enough electric field at the interface, which results in recombination losses of photo-generated charge carriers before reaching to contacts and higher thickness of a-Si:H(p) layer adds resistance and optical losses [3,7,8]. With the motivation to sort out these problems and improve the efficiency of c-Si/a-Si:H solar cells, one sided c-Si/a-Si:H heterojunction solar cells (*Ag/Al/c-Si(n)/a-Si:H(i)/a-Si:H(p)/ITO/Ag*) were fabricated by tuning the thickness and doping of a-Si:H(p) layer by RFPECVD technique. A systematic investigation has been caried out to study the influence of diborane flow rate and thickness of i and p- layers to identify the role of doping and thickness of a-Si:H(p) layer on the performance of c-Si/a-Si:H heterojunction solar cells. The open circuit voltage (V_{oc}), short circuit density (J_{sc}), fill factor (FF) and efficiency (η) of solar cells were estimated by I-V measurements. EQE measurements were carried out on the cells with and without external reverse bias to study interface properties and significance of electric field at interface.

7.1. Experimental details

7.1.1. Fabrication of c-Si/a-Si:H heterojunction solar cells

One sided c-Si/a-Si:H heterojunction solar cells (*Ag/Al/c-Si(n)/a-Si:H(i)/a-Si:H(p)/ITO/Ag*) were fabricated by RFPECVD in multichamber system. For fabrication of solar cells, we have followed standard RCA cleaning of Si wafers [9,10] (Chapter 2) and other process for c-Si (Al deposition, annealing at 400 °C and 10 min HPT of c-Si wafer) presented in Chapter 6.

Subsequently, a-Si:H(i) layer of varying thickness i.e 35/33 nm was deposited. The Si wafers were then shifted to a-Si:H(p) layer deposition chamber, where the a-Si:H(i) layers were subjected to 2 min HPT prior to the deposition of top a-Si:H(p) layer. Subsequently 10 or 7 nm thick a-Si:H(p) layer with different boron doping concentration was deposited to complete the cells. Deposition conditions for c-Si/a-Si:H heterojunction solar cells are listed in Table 7.1. For H_2 plasma treatment, only hydrogen at flow rate of 50 SCCM was used with other parameters; rf power, substrate temperature, process pressure maintained same as those for i-layer. We have adopted similar procedure for deposition of ITO layer and Ag contacts as presented in Chapter 6.

Table 7.1. Deposition conditions for c-Si/a-Si:H heterojunction solar cells.

Cell	Layer	H_2 (SCCM)	SiH_4 (SCCM)	B_2H_6 (SCCM)	PP (mbar)	Dep.temp. (ºC)	Layer thickness (nm)
nip5	a-Si:H(p)	60	4	6	0.42	200	10
	a-Si:H(i)	50		-			7
nip6	a-Si:H(p)	60		10			10
	a-Si:H(i)	50		-			7
nip7	a-Si:H(p)	60		14			10
	a-Si:H(i)	50		-			7
nip8	a-Si:H(p)	60		14			10
	a-Si:H(i)	50		-			5
nip9	a-Si:H(p)	60		20			10
	a-Si:H(i)	50		-			5
nip10	a-Si:H(p)	60		20			7
	a-Si:H(i)	50		-			5

The *I-V* characteristics measurements on c-Si/a-Si:H heterojunction solar cells were done under 100 mW/cm^2 of incident power density from a Xenon lamp with AM1.5 conditions. External Quantum Efficiency (EQE) measurements were carried out in the range 350-1100 nm. Si photo diode calibrated for global AM1.5 spectra was used as reference to estimate the EQE of the cells as discussed in section 2.2.10, Chapter 2 and reported in our publication [11–13].

7.2. Results and discussion

7.2.1. Current voltage measurement of solar cells

Fig. 7.1 shows the dark current density-voltage (*J-V*) characteristics of all the c-Si/a-Si:H heterojunction solar cells under reverse and forward bias conditions. A systematic decrease in reverse saturation current density (J_0) of cells is observed from *nip5* to *nip10*; as the diborane flow rate is increased and/or thickness of the a-Si:H(i) and a-Si:H(p) layer is decreased. The

TH-2097_126121019

lowest value of J_0 is obtained for the *nip10* cell, which was fabricated with diborane flow rate at 20 SCCM and a-Si:H(i) and a-Si:H(p) layers being 5 and 7 nm thick respectively. For all the cells, the high injection region started at a forward bias of about 700 mV. This is an indication that the solar cells are likely to have a high V_{oc} of ~700 mV and increase in efficiency with increase in the doping of the a-Si:H(p) layer and reduction in thickness of a-Si:H layers.

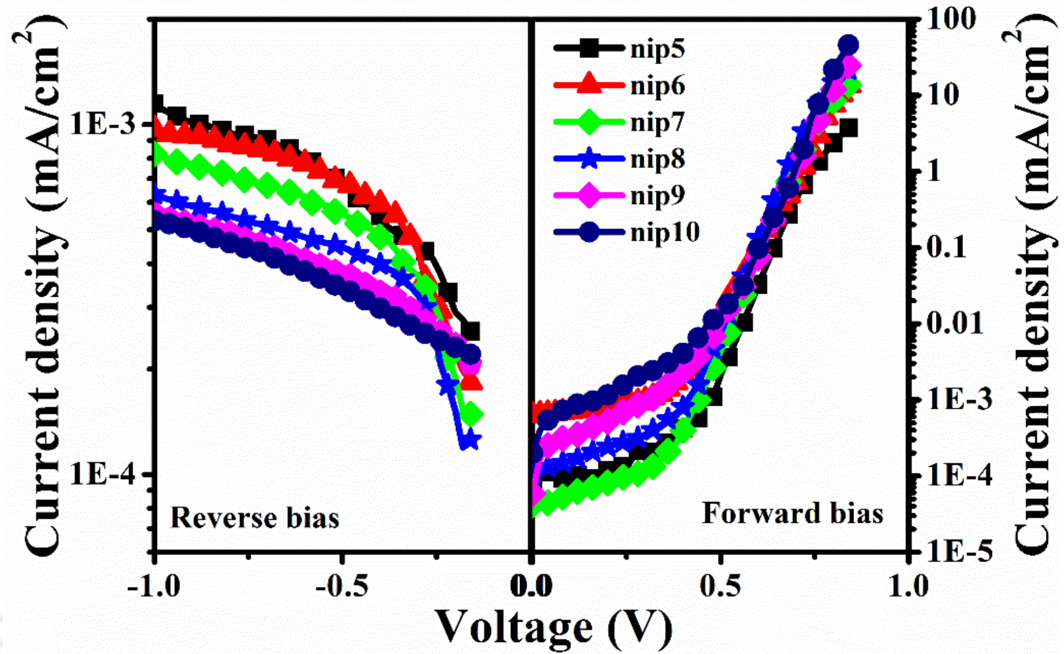

Fig. 7.1. Dark *J-V* characteristics of cells under reverse and forward bias condition.

Fig. 7.2 shows the *J-V* characteristics of c-Si/a-Si:H solar cells under AM1.5 illumination. The dark *J-V* characteristic of two cells (*nip5* and *nip10)* has also been included in Fig. 7.2 for quick reference. The values of solar cell parameter; J_{sc}, V_{oc}, FF (Eq. 2.29), and efficiency (η) (Eq. 2.30) for all the cells calculated from the *J-V* curve are listed in Table 7.2. A systematic increase in these values is observed from *nip5* to *nip10* cells. This improvement in J_{sc} and V_{oc} values is due to the systematic increase of doping of a-Si:H(p) and decrease in thickness of a-Si:H(i) and a-Si:H(p) layer accompanied with the reduction in void fraction at n/i and i/p interfaces and overall improvement in microstructure of a-Si:H layers. A crossover of *J-V* characteristic in dark and under illumination is observed around 700 mV for the *nip5-nip10* cells. We have achieved high V_{oc} of 705 mV and efficiency of 17.3% for single side c-Si/a-Si:H heterojunction solar cells fabricated at diborane flow rate at 20 SCCM and a-Si:H(i) and a-Si:H(p) layers being 5 and 7 nm thick respectively.

TH-2097_126121019

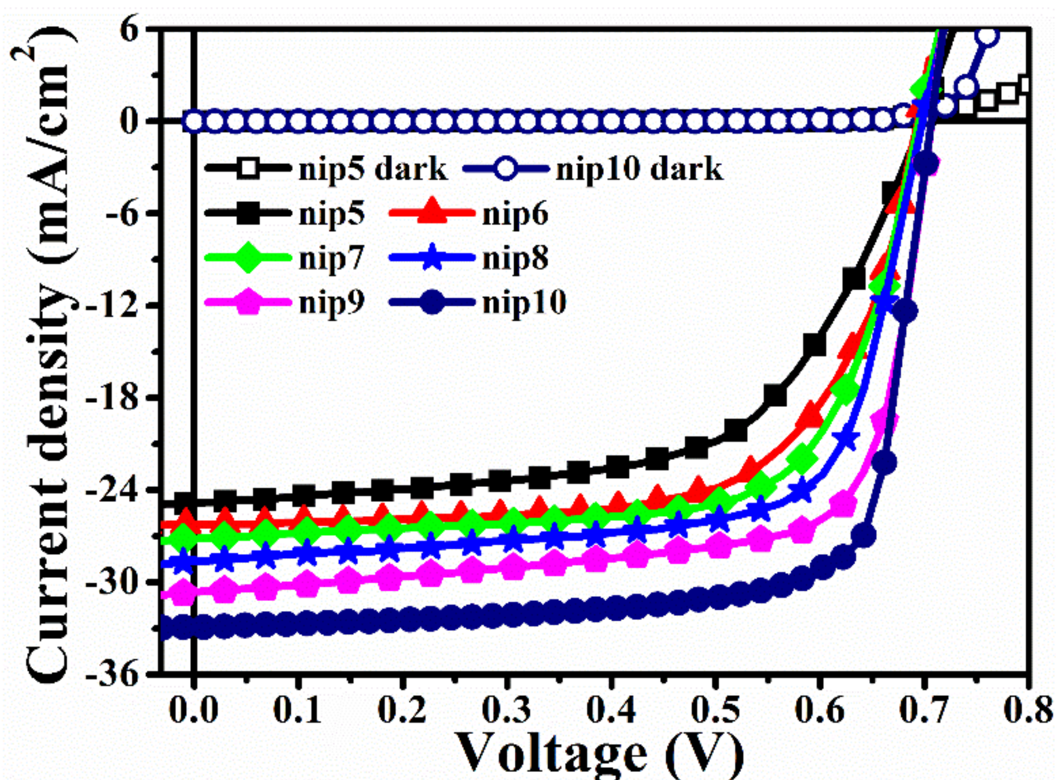

Fig. 7.2. *J-V* characteristics of *Ag/Al/c-Si(n)/a-Si:H(i)/a-Si:H(p)/ITO/Ag* heterojunction solar cells.

Table 7.2: The solar cell parameters of c-Si/a-Si:H heterojunction solar cells.

J-V measurement									EQE measurement	
Cell	J_{sc} (mA/cm^2)	V_{oc} (mV)	J_{max} (mA/cm^2)	V_{max} (mV)	FF	η (%)	R_{sh} (Ωcm^2)	R_s (Ωcm^2)	J_{sc} (mA/cm^2)	η (%)
nip5	24.81	694	20.10	519	0.60	10.43	185	7.6	23.47	9.87
nip6	26.23	694	22.85	533	0.67	12.18	323	4.3	24.92	11.60
nip7	27.15	695	23.06	563	0.69	12.98	307	3.8	26.33	12.61
nip8	28.65	698	24.03	483	0.70	14.01	305	3.0	28.20	13.79
nip9	31.07	705	26.83	602	0.74	16.15	315	2.5	30.69	15.96
nip10	32.72	705	28.11	620	0.75	17.30	583	2.0	32.11	16.97

The open circuit voltage has systematically increased from 694 to 705 mV for *nip5* to *nip10* cells respectively. These values are slightly lower than reported value of 711 mV in Chapter 6 [11], however still the present V_{oc} values are higher than values reported by other groups so far for single sided heterojunction solar cells on n-and p- type c-Si [14–19].

The detailed studies of influence of HPT on c-Si and a-Si:H layer were presented in previous Chapter 6. These results suggest that HPT has passivated c-Si surface, a-Si:H(i) layer, interfaces and also improve the microstructure of a-Si:H layers of c-Si/a-Si:H heterojunction solar cells. Therefore, recombination losses of photo generated carriers are reduced for *nip5-nip10* cells having good interfaces and transport properties [20]. The V_{oc} of cells has increased

TH-2097_126121019

with increase in boron doping of a-Si:H(p) layer. In this series of cells, we have obtained high V_{oc} of 705 mV for *nip9* and *nip10* cells. The J_{sc} of these cells is systematically increased due to increase in doping of a-Si:H(p) layer, which provided enough charge density in the depletion region to overcome any field distortion at the interface. An increase in electric field at the interface also helped in quick separation of photo-generated charge carriers before these recombine, which further increased the J_{sc}. In case of cells (*nip5*) prepared at low boron concentration (DBFR 6 SCCM), the J_{sc} of 24.81 mA/cm^2 was obtained, which was enhanced to 26.23 and 27.15 mA/cm^2 for *nip6* (DBFR 10 SCCM) and *nip7* (DBFR 14 SCCM) cells respectively along with a systematic increase in FF. To further improve J_{sc}, thickness of i-layer was decreased to 5 nm from 7 nm for *nip8* keeping the DBFR at 14 SCCM. The J_{sc} of *nip8* has further improved to 28.65 mA/cm^2 due to lower absorption of photons in the less thick a-Si:H(i) layer than *nip7* and also smaller path length of photo generated carriers to reach metal contacts [5,14]. This J_{sc} value (28.65 mA/cm^2) is still lower than that expected in SHJ solar cells [1,21,22]. In an attempt to increase the J_{sc} further, DBFR was again increased to 20 SCCM to increase the doping of a-Si:H(p) layer. This increase in doping resulted in the decrease of series resistance of the cell; J_{sc} value was increased to 31.07 mA/cm^2 for *nip9* cell along with the V_{oc} of 705 mV and FF of 0.74. To further increase the J_{sc}, another solar cell (*nip10*) was fabricated with a lower thickness (7 nm) of a-Si:H(p) keeping DBFR at 20 SCCM and thickness of a-Si:H(i) layer at 5 nm. The J_{sc} for this cell (*nip10*) was 32.72 mA/cm^2 with a V_{oc} of 705 mV and FF of 0.75. This increment in J_{sc} is mainly due to improvement in the generation and collection of free charge carriers, reducing the resistance losses and decreasing the minority carrier path length by decreasing the thickness of i- and p- layers. Our best FF values are 0.74 and 0.75 corresponding to the *nip9* and *nip10* cells respectively. The FF mainly depends on shunt and series resistance and also void fraction in the different layers [23–25]. Table 7.2 lists the shunt (R_{sh}) and series (R_s) resistance values estimated from the *J-V* curve of the cells using Eq. 2.31 and Eq. 2.32. As evident from the Table 7.2, a systematic decrease in series resistance and increase in shunt resistance is observed as the DBFR is increased and thickness of a-Si:H(i) and a-Si:H(p) layer is decreased from *nip5* to *nip10* cells. The improvement in V_{oc}, J_{sc} and FF resulted in improvement in the efficiency of solar cells. We have achieved best efficiency of 17.3% for *nip10* cell.

7.2.2. Quantum efficiency measurement of solar cells

Fig. 7.3 shows the EQE of c-Si/a-Si:H heterojunction *nip5-nip10* solar cells. The EQE of the cells was estimated using Eq. 2.33. The highest quantum efficiency of *nip10* cells is nearly 94

TH-2097_126121019

to 96% over a broad spectral range (450-850 nm). For *nip5* cell EQE is ~ 77% in the spectral range of 550-800 nm. The EQE has slightly enhanced for *nip6* cell as compared to *nip5* cell. For *nip7* cell, EQE has further improved in lower (450-550 nm) and mid (550-800 nm) wavelength range. This is due to better collection of charge carriers and smaller series resistance with increase in doping of a-Si:H(p) layer. A significant improvement in EQE (~87%), over a broad spectral range (500-850 nm), for *nip8* is observed. The cell was fabricated with the same DBFR (14 SCCM) as that for *nip7,* but with a lower thickness of a-Si:H(i) layer. For this cell, the EQE is more than 70%, both in the low wavelength region (~450 nm) as well as high wavelength region (~900 nm). For *nip9* and *nip10,* where the doping of a-Si:H(p) layer was increased along with a decrease in thickness of p layer keeping the thickness of the a-Si:H(i) layer same as that for *nip8*, EQE crossed 90% in the mid wavelength range along with a significant improvement in both low as well as high wavelength range. The EQE for these cells is ~80% at 450 nm as well as 850 nm. The improvement at low wavelength range is mainly due to decrease in thickness of p- and i-layer, which helped more photons to be absorbed in the c-Si wafer. A significant improvement in EQE in both low and high wavelength range is a signature of good quality abrupt junction [26]. The EQE spectra are used to estimate the integrated short circuit current density J_{sc} for AM1.5G spectra using Eq. 2.35 and the values are listed in Table 7.2. It is evident that J_{sc} values obtained from *J-V* measurements and calculated from EQE spectra are in good agreement. Table 7.2 also lists the efficiency of these solar cells calculated using the J_{sc} values from EQE spectra and V_{oc} and FF obtained from *J-V* measurements.

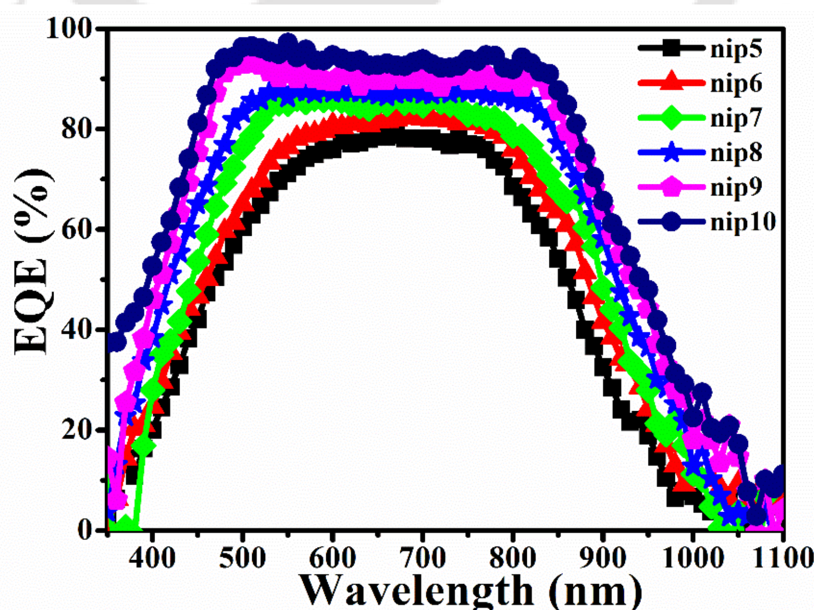

Fig. 7.3. EQE spectra of c-Si/a-Si:H heterojunction solar cells.

TH-2097_126121019

In order to check if the improvement in EQE is due to only less absorption of photons in p and i-layer, or whether the increase in doping concentration had any role in improving the electric field at the p/i and i/n interfaces, the EQE spectra were measured under slight reverse bias condition (-1V). Fig. 7.4 show these spectra under no bias as well as under reverse bias conditions for each of the cell fabricated for this study.

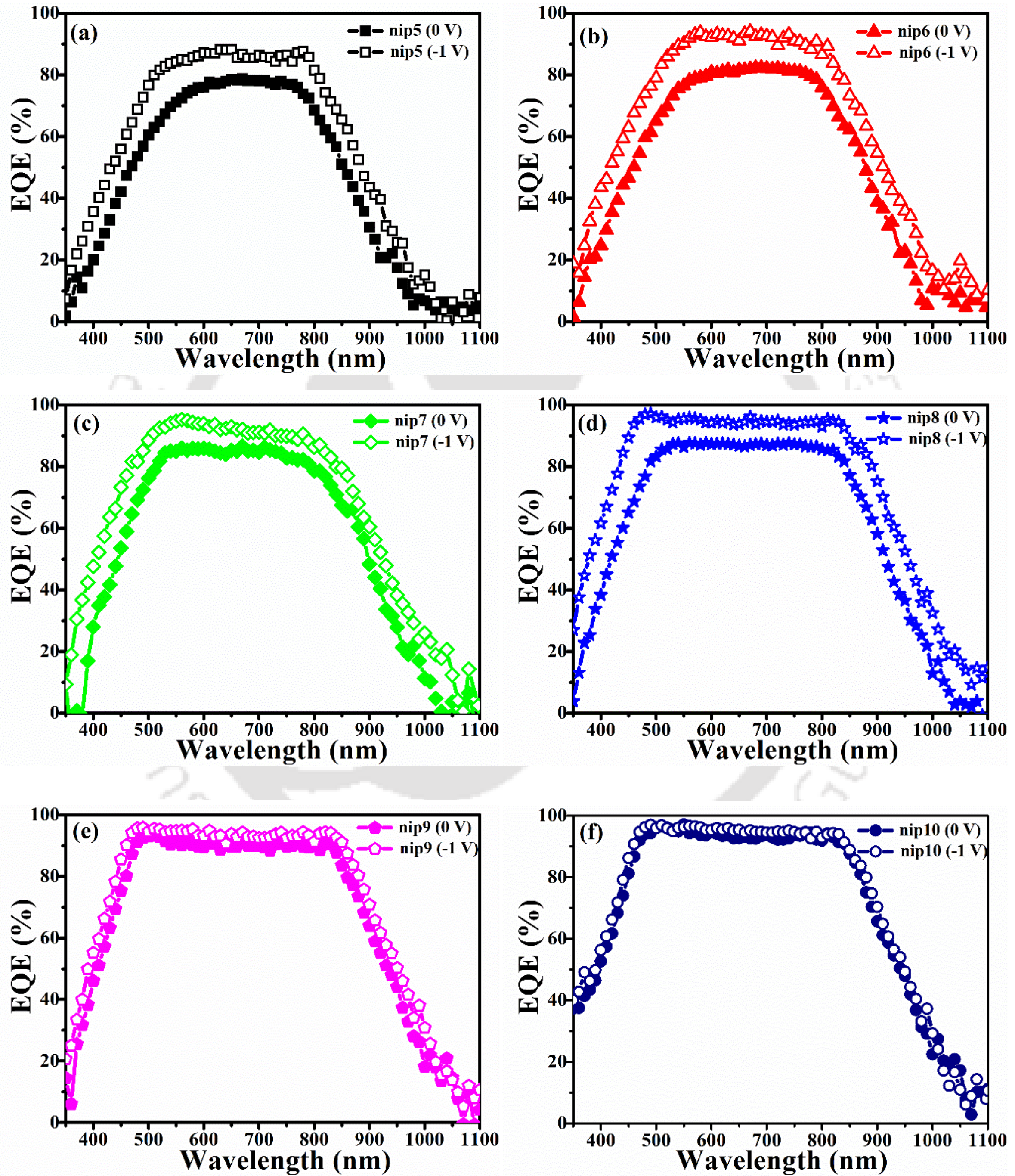

Fig. 7.4(a-f). EQE spectra of c-Si/a-Si:H heterojunction solar cells with and without reverse biasing.

It can be seen from these spectra that for *nip5* to *nip8* cells, the EQE measured under reverse bias conditions is more than that under no bias condition (Fig. 7.4(a-d)). This clearly indicates

TH-2097_126121019

that with increase in doping of p-layer, though, we have been able to collect more carriers to the respective electrodes, the electric field at the interface and in the i-layer is still not sufficient to sweep all the carriers to the respective electrodes. By decreasing the thickness of i-layer in *nip8* cell (Fig. 7.4d), response in the mid wavelength range, as well as in the low and high wavelength range was significantly improved as compared to *nip7* cell, which has the same doping and thickness of p layer. This is due to less absorption of photons in the i-layer. When the doping of p-layer is further increased for *nip9*, not only EQE has increased, the response under zero bias condition and reverse bias condition has also been almost same (Fig. 7.4e). For *nip10* cell, for which the thickness of p-layer was decreased to 7 nm, the EQE is almost ~94-96% in a broad wavelength range with an increase in response below 400 nm and no change in EQE under reverse bias conditions (Fig. 7.4f). The increase in response below 400 nm for *nip10* cell is attributed to the less absorption in p-layer. The observations also suggest that the p-layer deposited with a DBFR of 20 SCCM provides enough electric field at the interface to sweep all the photo-generated charge carriers to the respective electrodes and reduce recombination loss at bulk of layer and the i/p as well as p/ITO interfaces.

7.3. Conclusion

Single side c-Si/a-Si:H heterojunction solar cells were fabricated by varying doping and thickness of a-Si:H(p) layer. We have achieved high open circuit voltage of 705 mV and efficiency of 17.3% on n-type c-Si substrates. These high performance device results are obtained by H_2 plasma treatment on c-Si and a-Si:H(i) layer, increase of doping and decrease of thickness of a-Si:H(p) layer. These values are highest so far among those reported by other groups for single side c-Si/a-Si:H solar cells. Electric field at the junction of solar cells has enhanced significantly with increase in doping of p-layer. Generated electron-hole pairs are separated immediately and swept to metal contacts without any recombination losses at the interfaces and bulk of a-Si:H layers by enhanced electric field. Further, this is confirmed by EQE measurements with and without external biasing conditions.

7.4. References

[1] Y. Tsunomura, Y. Yoshimine, M. Taguchi, T. Baba, T. Kinoshita, H. Kanno, H. Sakata, E. Maruyama, M. Tanaka, Twenty-two percent efficiency HIT solar cell, Sol. Energy Mater. Sol. Cells. 93 (2009) 670–673. doi:10.1016/j.solmat.2008.02.037.

[2] M. Taguchi, A. Terakawa, E. Maruyama, M. Tanaka, Obtaining a higher Voc in HIT cells, Prog. Photovoltaics Res. Appl. 13 (2005) 481–488. doi:10.1002/pip.646.

TH-2097_126121019

[3] S. De Wolf, A. Descoeudres, Z.C. Holman, C. Ballif, High-efficiency Silicon Heterojunction Solar Cells: A Review, Green. 2 (2012) 7–24. doi:10.1515/green-2011-0018.

[4] S. Kim, V. Ai Dao, Y. Lee, C. Shin, J. Park, J. Cho, J. Yi, Processed optimization for excellent interface passivation quality of amorphous/crystalline silicon solar cells, Sol. Energy Mater. Sol. Cells. 117 (2013) 174–177. doi:10.1016/j.solmat.2013.05.042.

[5] M.R. Page, E. Iwaniczko, Y. Xu, L. Roybal, F. Hasoon, Q. Wang, R.S. Crandall, Amorphous / crystalline silicon heterojunction solar cells with varying i-layer thickness, Thin Solid Films. 519 (2011) 4527–4530. doi:10.1016/j.tsf.2011.01.293.

[6] J. Zhao, A. Wang, M.A. Green, High-efficiency PERL and PERT silicon solar cells on FZ and MCZ substrates, Sol. Energy Mater. Sol. Cells. 65 (2001) 429–435. doi:10.1016/S0927-0248(00)00123-9.

[7] R.V.K. Chavali, S. De Wolf, M.A. Alam, Device physics underlying silicon heterojunction and passivating-contact solar cells: A topical review, Prog. Photovoltaics Res. Appl. 26 (2018) 241–260. doi:10.1002/pip.2959.

[8] S. Tohoda, D. Fujishima, A. Yano, A. Ogane, K. Matsuyama, Y. Nakamura, N. Tokuoka, H. Kanno, T. Kinoshita, H. Sakata, M. Taguchi, E. Maruyama, Future directions for higher-efficiency HIT solar cells using a Thin Silicon Wafer, J. Non. Cryst. Solids. 358 (2012) 2219–2222. doi:10.1016/j.jnoncrysol.2012.03.025.

[9] W. Kern , Puotinen D A, Cleaning solutions based on hydrogen peroxide for use in silicon semiconductor technology, RCA Rev. 31 (1970) 187–206.

[10] Werner Kern, The Evolution of Silicon Wafer Cleaning Technology, J. Electrochem. Soc. 137 (1990) 1887–1892. doi:10.1149/1.2086825.

[11] Venkanna Kanneboina, R. Madaka, P. Agarwal, High open circuit voltage c-Si/a-Si:H heterojunction solar cells: Influence of hydrogen plasma treatment studied by spectroscopic ellipsometry, Sol. Energy. 166 (2018) 255–266. doi:10.1016/j.solener.2018.03.068.

[12] Ramakrishna Madaka, Venkanna Kanneboina, Pratima Agarwal, Low-Temperature Growth of Amorphous Silicon Films and Direct Fabrication of Solar Cells on Flexible Polyimide and Photo-Paper Substrates, J. Eectronic Mater. 47 (2018) 4710–4720. doi:10.1007/s11664-018-6344-0.

[13] Ramakrishna Madaka, Venkanna Kanneboina, Pratima Agarwal, Enhanced performance of amorphous silicon solar cells (110°C) on flexible substrates with a-SiC:H(p) window layer and H2 plasma treatment at n/i and i/p interface, Semicond. Sci. Technol. 33 (2018) 3.

[14] H. Fujiwara, M. Kondo, Effects of a-Si:H layer thicknesses on the performance of a-Si:H/c-Si heterojunction solar cells, J. Appl. Phys. 101 (2007) 054516. doi:10.1063/1.2559975.

TH-2097_126121019

[15] H. Fujiwara, M. Kondo, Impact of epitaxial growth at the heterointerface of a-Si:H/c-Si solar cells, Appl. Phys. Lett. 90 (2007) 2005–2008. doi:10.1063/1.2426900.

[16] H. Fujiwara, T. Kaneko, M. Kondo, Optimization of interface structures in crystalline silicon heterojunction solar cells, Sol. Energy Mater. Sol. Cells. 93 (2009) 725–728. doi:10.1016/j.solmat.2008.09.007.

[17] W.K. Oh, S.Q. Hussain, Y.J. Lee, Y. Lee, S. Ahn, J. Yi, Study on the ITO work function and hole injection barrier at the interface of ITO/a-Si:H(p) in amorphous/crystalline silicon heterojunction solar cells, Mater. Res. Bull. 47 (2012) 3032–3035. doi:10.1016/j.materresbull.2012.04.106.

[18] T.H. Wang, M.R. Page, E. Iwaniczko, Q. Wang, Y. Xu, Y. Yan, L. Roybal, D. Levi, R. Bauer, H.M. Branz, 17.5% p-Type Silicon Heterojunction Solar Cells with HWCVD a-Si : H as the Emitter and Back Contact, in: NREL/CP-520-38942, 2005: pp. 1–5. doi:https://digital.library.unt.edu/ark:/67531/metadc892630/m1/3/.

[19] T.H. Wang, E. Iwaniczko, M.R. Page, Q. Wang, Y. Xu, Y. Yan, D. Levi, L. Roybal, R. Bauer, H.M. Branz, High-Efficiency Silicon Heterojunction Solar Cells by HWCVD, in: IEEE 4th World Conf., 2006: pp. 1439–1442. doi:10.1109/WCPEC.2006.279723.

[20] F. Meng, L. Shen, J. Shi, L. Zhang, J. Liu, Y. Liu, Z. Liu, Role of the buffer at the interface of intrinsic a-Si:H and p-type a-Si:H on amorphous/crystalline silicon heterojunction solar cells, Appl. Phys. Lett. 107 (2015) 223901.

[21] T. Mishima, M. Taguchi, H. Sakata, E. Maruyama, Development status of high-efficiency HIT solar cells, Sol. Energy Mater. Sol. Cells. 95 (2011) 18–21. doi:10.1016/j.solmat.2010.04.030.

[22] M. Taguchi, A. Yano, S. Tohoda, K. Matsuyama, Y. Nakamura, T. Nishiwaki, K. Fujita, E. Maruyama, 24.7% Record efficiency HIT solar cell on thin silicon wafer, IEEE J. Photovoltaics. 4 (2014) 96–99. doi:10.1109/JPHOTOV.2013.2282737.

[23] H. Sonobe, A. Sato, S. Shimizu, T. Matsui, M. Kondo, A. Matsuda, Highly stabilized hydrogenated amorphous silicon solar cells fabricated by triode-plasma CVD, Thin Solid Films. 502 (2006) 306–310. doi:10.1016/j.tsf.2005.07.300.

[24] Q. Wang, Fill factor related issues in hydrogenated amorphous Si solar cells, Sol. Energy Mater. Sol. Cells. 129 (2014) 64–69. doi:10.1016/j.solmat.2014.02.015.

[25] S.Y. Lee, J.H. Shim, D.J. You, S.W. Ahn, H.M. Lee, The novel usage of spectroscopic ellipsometry for the development of amorphous Si solar cells, Sol. Energy Mater. Sol. Cells. 95 (2011) 142–145. doi:10.1016/j.solmat.2010.04.054.

[26] M. Agarwal, A. Pawar, N. Wadibhasme, R. Dusane, Controlling the c-Si/a-Si:H interface in silicon heterojunction solar cells fabricated by HWCVD, Sol. Energy. 144 (2017) 417–423. doi:10.1016/j.solener.2017.01.039.

TH-2097_126121019

Chapter 8

Conclusions and Future Scope

The main aim of the work presented in this thesis was to fabricate high efficiency and high open circuit voltage single side c-Si(n)/a-Si:H(p) heterojunction solar cells. In order to improve the device performance, we have studied the influence of hydrogen plasma treatment and hydrogen flow rate on the microstructural, optical and electrical properties of intrinsic and doped a-Si:H films. Solar cells were fabricated with optimized parameters for best quality a-Si:H films. Properties of interfaces and each layer of solar cells were studied with different characterization tools. We have achieved high open circuit voltage and efficiency for single side c-Si/a-Si:H heterojunction solar cells, which are highest among those reported so far for single side c-Si/a-Si:H heterojunction cells. The overall conclusions of the thesis work and future research scope are presented in this chapter.

8.1. Thesis conclusions

1. The influence of intermittent hydrogen plasma treatment on the microstructure of a-Si:H films was studied. It was observed that exposure to hydrogen plasma during deposition of a-Si:H films improves the microstructure of the films by etching the amorphous phase and replacing the weak Si-Si and Si-H_2 bonds by strong Si-H bonds.
2. We observed that microstructure factor is directly related to the void volume fraction in the films and also to the amplitude of the imaginary part of pseudo dielectric function. The single TL model could not give accurate results in case of mixed phase of a-Si:H and nc-Si:H films and TL+Gauss model has to be used to calculate the optical constants, thickness and band gap of the films. Further, results obtained from the TL+Gauss model had been compared with those obtained using TL+BEMA for accuracy of the model.
3. Estimated optical constants, thickness and band gap of the a-Si:H films match well with those obtained from the analysis of UV-Vis-NIR transmission data.
4. The void, amorphous and crystalline volume fractions and surface roughness of the films from BEMA model values are well correlated with those obtained from FTIR,

TH-2097_126121019

Raman and AFM measurements results. The overall deposition rate of these nc-Si films was higher than that obtained by hydrogen dilution of silane for similar films.

5. Process of H_2 plasma treatment is used to fabricate stable c-Si/a-Si:H solar cells and also to increase the efficiency of c-Si/a-Si:H heterojunction solar cells by reducing the interface defects and improving the passivation of coordination defects.
6. Influence of hydrogen flow rate on microstructure, optical properties of a-Si:H(p) and a-Si:H(n) films was studied by SE measurements. It is observed that microstructure of a-Si:H(p) and a-Si:H(n) films changes from amorphous to nano crystalline phase by increasing the hydrogen dilution.
7. The phase transition is confirmed by SE analysis; shift in peak position of pseudo dielectric function of these films from 3.6 eV (for pure a-Si:H) to 4.1 eV with a shoulder peak at 3.4 eV (near onset of nanocrystalline) as the hydrogen flow rate is increased. The bandgap, surface roughness and crystallinity of the films has increased with increase in HFR of the films.
8. It is found that less defective a-Si:H films with smaller void fraction and improved Si-H bond density are obtained at 60 SCCM and 70 SCCM of HFR for a-Si:H(p) and a-Si:H(p) films respectively. This optimised parameters were used to deposit a-Si:H(p) films with improved microstructure for fabrication and improve the performance of c-Si/a-Si:H solar cells.
9. Indium tin oxide (ITO) thin films were deposited by RF Sputtering technique by varying deposition temperature of 50 to 200 °C. It is observed that the films deposited at 50°C were nanocrystalline in nature. The film crystallinity was enhanced with increases in deposition temperature and saturated at 150 °C. Williamson-Hall plot has been used to estimate crystallite size of the ITO films, which are 21.7, 26.8 and 27.5 nm corresponding to films deposited at 100, 150 and 200 °C respectively.
10. It is found that films deposited at 150 °C have high transmission of 91-98% in the wavelength range of 400-1500 nm, low sheet resistance of 7.5 Ω/□ and surface roughness of 6.1 nm. These highly crystallized, transparent, low sheet resistance ITO films deposited at low temperature are used for improving the interface properties and efficiency of solar cells.
11. Single side c-Si(n)/a-Si:H(p) heterojunction solar cells with open circuit voltage as high as 711 mV were fabricated successfully. This high V_{oc}, which is highest among those reported so far for single side c-Si/a-Si:H heterojunction cells, could be achieved

TH-2097_126121019

because of improvement in microstructure of a-Si:H(i) layer and interface layers by the hydrogen plasma treatment of this layer prior to the deposition of a-Si:H(p) layer.

12. The SE studies confirmed that H_2 plasma treatment of a-Si:H(i) layer not only etched out the significant amorphous fraction of this layer but also reduced the void fraction. The hydrogen plasma treatment has also passivated and improved the n/i, i/p interfaces and a-Si:H layers without deteriorating the electronic quality of layers. The HPT is also used to control the thickness of a-Si:H(i) layer, where is otherwise very difficult to control.
13. It is observed that the efficiency and fill factor of cells have a direct correlation with the amplitude of $< \varepsilon_2 >$ spectra of cells. The results suggest H_2 plasma treatment as an approach to achieve surface passivation and improve the open circuit voltage of c-Si/a-Si:H heterojunction solar cells.
14. High open circuit voltage of 705 mV and efficiency of 17.3% for single side c-Si(n)/a-Si:H(p) heterojunction solar cells is achieved by varying boron doping and thickness of a-Si:H(p) layer.
15. High performance device results are obtained mainly due to H_2 plasma treatment on c-Si and a-Si:H(i) layer, increase of doping and decrease of thickness of a-Si:H(p) layer.
16. EQE measurements were done on the c-Si/a-Si:H heterojunction solar cells with and without external biasing conditions to investigate spectral response and interface properties of the cells.
17. Electric field at the junction of solar cells has enhanced significantly with increase in doping of p-layer. Generated electron-hole pair are separated immediately and swept to metal contacts without any recombination losses at the interfaces and bulk of a-Si:H layers by enhanced electric field. Further, this is confirmed by EQE measurements with and without external biasing conditions.

8.2. Future scope

Present thesis is mainly focused on improvement of the interface properties, open circuit voltage and efficiency of single side c-Si(n)/a-Si:H(p) heterojunction solar cells. The present work can be extended in several ways, as described below.

1. Surface texturing can be done to improve the short circuit current density of solar cells by reducing the absorption losses, reducing the reflection of light at front surface and increasing internal reflection on the rear side.

TH-2097_126121019

2. Passivation of surface and interface can be improved by deposited very thin silicon oxide or silicon nitride layers along with hydrogen plasma treatment.
3. Efficiency of solar cells can be improved by deposited a-Si:H back surface field and also double side silicon heterojunction solar cells.
4. Fabrication of tunnel oxide passivated contact silicon (TOPCon), interdigitated back contact silicon heterojunction (IBC-SHJ) solar cells with hydrogen plasma treatment to improve the efficiency of solar cells.
5. In order to reduce the cost of Si wafer, thinner wafers and multi crystalline Si (mc-Si) can be used for fabrication of solar cells. Efficiency of solar cells on mc-Si wafers can be improved by different processes.

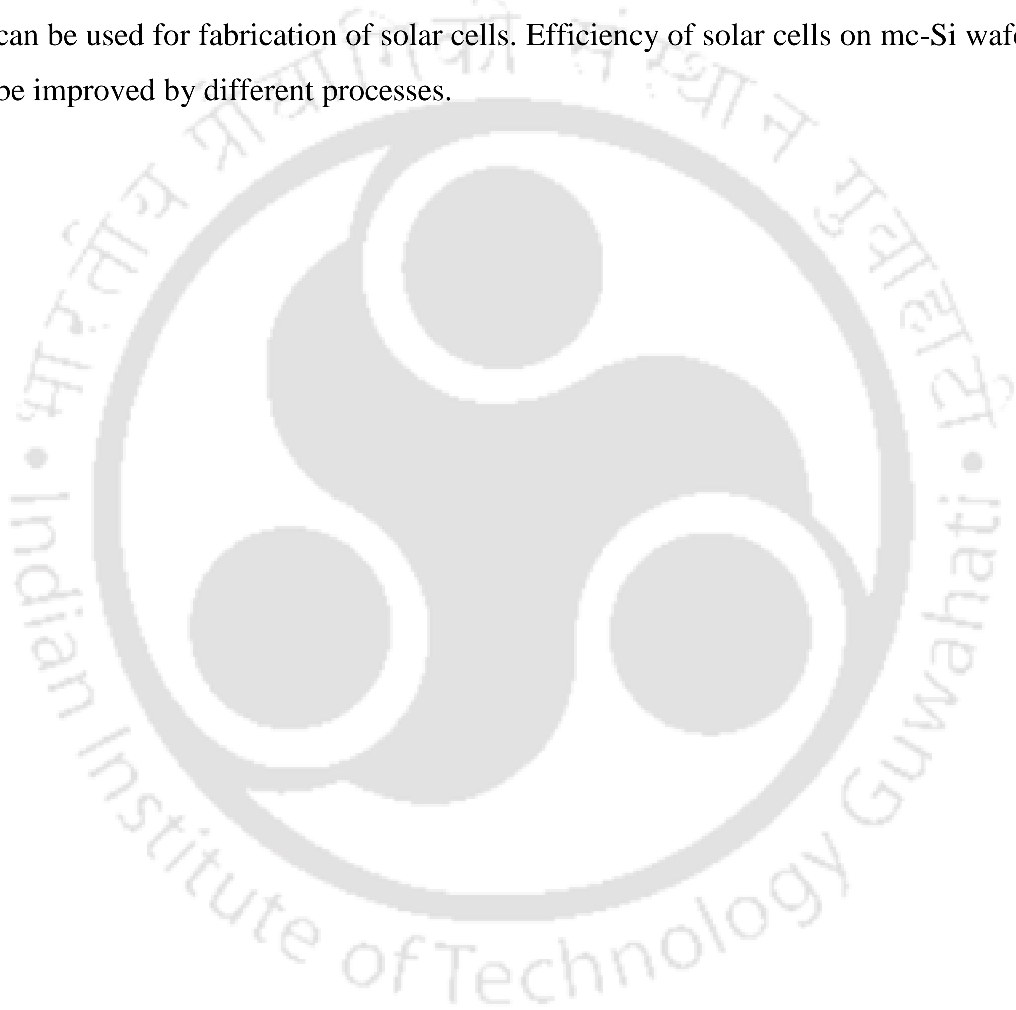

TH-2097_126121019

Appendix I

Tauc-Lorentz model

An expression for the real part of the dielectric function is obtained by Kramers-kroning integration, given by Eq. A.1

$$< \varepsilon_1(E) >= \varepsilon_1(\infty) + \frac{2}{\pi} P \int_{E_g}^{\infty} \frac{\xi \varepsilon_2(\xi)}{\xi^2 - E^2} d\xi \qquad \text{------------- (A.1)}$$

Where P represents the Cauchy principal part of the integral and $\varepsilon_1(\infty)$ is additional fitting parameter.

After solving above express, the real part of the dielectric function is given by

$$< \varepsilon_{1TL}(E) > = \varepsilon_{1TL}(\infty) + \frac{1}{2}\frac{A}{\pi}\frac{C}{\zeta^4}\frac{a_{ln}}{\alpha E_0} ln\left[\frac{(E_0^2+E_g^2+\alpha E_g)}{(E_0^2+E_g^2-\alpha E_g)}\right] - \frac{A}{\pi}\frac{1}{\zeta^4}\frac{a_{atan}}{E_0}\left[\pi - arctan\left(\frac{2E_g+\alpha}{C}\right) + arctan\left(\frac{2E_g+\alpha}{C}\right)\right] + 2\frac{AE_0C}{\pi\zeta^4}\left\{E_g(E^2-\gamma^2)\left[\pi + 2arctan\left(\frac{\gamma^2-E_g^2}{\alpha C}\right)\right]\right\} - 2\frac{AE_0C}{\pi\zeta^4}\frac{E^2+E_g^2}{E} ln\left(\frac{|E-E_g|}{E+E_g}\right) + 2\frac{AE_0C}{\pi\zeta^4}E_g ln\left[\frac{|E-E_g|(E+E_g)}{\sqrt{(E_0^2-E_g^2)^2+E_g^2C^2}}\right]$$

Where, $a_{ln} = (E_g^2 - E_0^2)E^2 + E_g^2C^2 - E_0^2(E_0^2 + 3E_g^2)$,

$a_{atan} = (E^2 - E_0^2)(E_0^2 + E_g^2) + E_g^2C^2$,

$\zeta^4 = (E^2 - \gamma^2)^2 + \frac{\alpha^2C^2}{4}$,

$\alpha = \sqrt{4E_0^2 - C^2}$,

$\gamma = \sqrt{E_0^2 - C^2/2}$

Tauc et.al [1] derived an expression for imaginary part of the dielectric function which describes inter-band transitions above the band edge and is given by Eq. A.2.

TH-2097_126121019

$$\varepsilon_{2,T}(E > E_g) = A_T \cdot \left(\frac{E-E_g}{E}\right)^2 \quad \text{------------- (A.2)}$$

The imaginary part of dielectric function from the Lorentz oscillator model [2] is given by Eq.A.3

$$\varepsilon_{2,L}(E) = \frac{A_L \cdot E_0 \cdot C \cdot E}{\left(E^2-E_0^2\right)^2 + C^2 E^2} \quad \text{------------- (2.10)}$$

The expression for the imaginary part of the dielectric function in Tauc Lorentz model [3] is given by Eq.A.4 (multiplying Eq.A.2 and Eq.A.3)

$$\varepsilon_{2,TL}(E) = \begin{cases} \left[\frac{A E_0 C \left(E-E_g\right)^2}{\left(E^2-E_0^2\right)^2 + C^2 E^2} \frac{1}{E}\right] & \text{for } E > E_g \\ 0 & \text{for } E \leq E_g \end{cases} \quad \text{------------- (A.4)}$$

Where A is oscillator strength, E_0 is peak transition energy, E_g is optical band gap and C is broadening parameter.

References

[1] J. Tauc, R. Grigorovici, A. Vancu, Optical Properties and Electronic Structure of Amorphous Germanium, Phys. Status Solidi. 15 (1966) 627–637. doi:10.1002/pssb.19660150224.

[2] H. Fujiwara, Spectroscopic Ellipsometry Principles and Applications, Willey Publ. (2007). doi:10.1002/9780470060193,ISBN:9780470016084.

[3] G.E.Jellison and F.A. Modine, Parameterization of the optical functions of amorphous materials in the interband region, Appl. Phys. Lett. 69 (1996) 371–373. doi:10.1063/1.118064.

List of Publications

1. **Venkanna Kanneboina** and Pratima Agarwal "Influence of Hydrogen Flow Rate on a-Si:H(n) Thin Films Studied by Spectroscopic Ellipsometry" **Journal of Electronic Materials,** Vol:48, pp: 2404-2410, 2019.
2. **Venkanna Kanneboina**, Ramakrishna Madaka and Pratima Agarwal, "High open circuit voltage c-Si/a-Si:H heterojunction solar cells with hydrogen plasma treatment" **Solar Energy**, Vol: 166, pp: 255-266, 2018.
3. **Venkanna Kanneboina**, Ramakrishna Madaka and Pratima Agarwal "Spectroscopic ellipsometry studies on microstructure evolution of a-Si:H to nc-Si:H films by H_2 plasma exposure" **Materials Today Communications**, Vol: 15, pp: 18-29, 2018.
4. **Venkanna Kanneboina**, Ramakrishna Madaka and Pratima Agarwal "Influence of hydrogen plasma treatment of intrinsic a-Si:H layer on the performance of the c-Si/a-Si:H heterojunction solar cells" **Materials Today: Proceedings**, Vol: 4, Issue: 14, pp: 12726-12729, 2017.
5. **Venkanna Kanneboina** and Pratima Agarwal "Influence of Deposition Temperature on Indium Tin Oxide Thin Films for Solar Cell Applications" **AIP Conference Proceedings,** 2091, 020016, 2019.
6. **Venkanna Kanneboina**, Ramakrishna Madaka and Pratima Agarwal "Single side c-Si/a-Si:H heterojunction solar cells with high open circuit voltage of 705 mV and 17.3% efficiency: Role of a-Si:H(p) layer doping and thickness" **(*Under review*).**
7. **Venkanna Kanneboina,** Ramakrishna Madaka and Pratima Agarwal "Growth of H_2 plasma subjected a-Si:H films studied through surface morphology" (***To be Submitted***).
8. **Venkanna Kanneboina**, Ramakrishna Madaka and Pratima Agarwal "Spectroscopic Ellipsometry Investigation of Optical and Structural Properties of a-Si:H Thin Films", (***To be submitted***).

List of Publications (*not related to thesis*)

9. Ramakrishna Madaka, Juhi Kumari, **Venkanna Kanneboina**, Himanshu S Jha Pratima Agarwal, "Role of chamber pressure on crystallinity and composition of silicon films using Silane and Methane as precursors in hot wire chemical vapour deposition technique" **Thin Solid Films** (***Accepted***).

TH-2097_126121019

10. Ramakrishna Madaka, **Venkanna Kanneboina**, Pratima Agarwal, "Exploring the photo paper as flexible substrate for fabrication of a-Si:H based thin film solar cells at low temperature (110°C) and influence of rf-power on opto-electronic properties" **Thin Solid Films,** 662, 155-164, 2018.
11. Madaka, **Venkanna Kanneboina**, Pratima Agarwal, "Low temperature growth of amorphous silicon films and direct fabrication of solar cells on flexible polyimide and photo paper substrate" **Journal of Electronic Materials**, 47, 4710-4720, 2018.
12. Ramakrishna Madaka, **Venkanna Kanneboina**, Pratima Agarwal, "Enhanced performance of amorphous silicon solar cells (110°C) on flexible substrates with p-a-SiC:H window layer and H_2 plasma treatment at n/i and i/p interface" "**Semiconductor Science and Technology**", 33, 8, 2018.
13. Ramakrishna Madaka, **Venkanna Kanneboina**, Pratima Agarwal," Evolution of nanostructure in hydrogenated amorphous silicon thin films with substrate temperature studied by Raman mapping, Ramanscattering and spectroscopic ellipsometry" **Journal of material science: materials in electronics**, (2017) 28:8885-8894.
14. Ramakrishna Madaka, **Venkanna Kanneboina**, Pratima Agarwal, "Raman and spectroscopic ellipsometry studies of a-Si:H thin films on low-cost photo paper substrate" **Materials Today: Proceedings** 4 (2017) 12666–12670.
15. Ramakeishna Madaka, Juhi Kumari, **Venkanna Kanneboina**, Pratima Agarwal, "Hydrogenated amorphous silicon solar cells fabricated at low substrate temperature 110ºC on flexible PETsubstrate" **AIP Conf. Proc**. May 2018,1953(1),100040.
16. Ramakrishna Madaka, Pilik Basumatary, **Venkanna Kanneboina**, Pratima Agarwal, "Amorphous silicon thin film solar cells fabricated on different substrates", **Springer Conf. Proc.** (***Accepted***).
17. Ramakrishna Madaka, **Venkanna Kanneboina,** Pilik Basumatary, Pratima Agarwal, "Influence of radio frequency power on opto-electronic properties of boron doped hydrogenated amorphous silicon films at low substrate temperature" (***To be submitted***).

TH-2097_126121019

Research Work Presented in International/National Conferences

1. **Venkanna Kanneboina**, Ramakrishna Madaka and Pratima Agarwal, "High open circuit voltage c-Si/a-Si:H heterojunction solar cells with hydrogen plasma treatment" "Research conclave" 08th -11th March 2018, IIT Guwahati, India.

2. **Venkanna Kanneboina**, Ramakrishna Madaka and Pratima Agarwal, **"**Hydrogen Plasma Treatment Induced crystallinity in a-Si:H Films Studied by Ellipsometry and Raman Spectroscopy" Abs Id: OP024, pp: 136, "National Workshop on Fluorescence and Raman Spectroscopy", 17th-21st December, 2017, IIT Guwahati, India**.**

3. **Venkanna Kanneboina**, Ramakrishna Madaka and Pratima Agarwal, **"**Improved performance of the c-Si/a-Si:H heterojunction solar cells with hydrogen plasma treatment" Abs Id: O84-K4, pp: 79 "International Conference on Thin Films", 13th-17th November, 2017, National Physical Laboratory, New Delhi, India**.**

4. **Venkanna Kanneboina**, Ramakrishna Madaka and Pratima Agarwal, "Spectroscopic ellipsometry investigation of hydrogenated amorphous and nano crystalline silicon thin films", Abs Id: PP82, pp: 144, "International Conference on Sophisticated Instruments in Modern Research", June 30th -1st July, 2017, IIT Guwahati, India**.**

5. **Venkanna Kanneboina,** Ramakrishna Madaka, Pilik Basumatary and Pratima Agarwal, "Spectroscopic Ellipsometry Investigation of Optical and Structural Properties of a-Si:H Thin Films" Abs Id: 20, pp: 43, "International conference on energy options tomorrow: Technology to sustainability" 17-19th April 2017, The Neotia University, Kolkata, India.

6. **Venkanna Kanneboina**, Ramakrishna Madaka and Pratima Agarwal, "Influence of hydrogen plasma treatment on the performance of the c-Si/a-Si:H solar cells", "Research conclave" pp: 223, 16-19 March 2017, IIT Guwahati, India.

7. **Venkanna Kanneboina**, Ramakrishna Madaka and Pratima Agarwal, "Influence of hydrogen plasma treatment of intrinsic a-Si:H layer on the performance of the c-Si/a-Si:H heterojunction solar cells", "Annual Physics Meet" 28th January 2017, Dept. of Physics, IIT Guwahati, India.

8. **Venkanna Kanneboina,** Ramakrishna Madaka and Pratima Agarwal, "Influence of hydrogen plasma treatment of intrinsic a-Si:H layer on the performance of the c-Si/a-

TH-2097_126121019

Si:H heterojunction solar cells", Abs Id: S-0411, pp: 43, "2nd International conference on solar energy photovoltaic", 17-19th December 2016, KIIT Bhubaneswar, Odisha, India.

9. **Venkanna Kanneboina**, Ramakrishna Madaka and Pratima Agarwal, "Low temperature RF sputtered ITO thin films as TCO layer for solar cells", "Research conclave" 18-20 March 2016, IIT Guwahati, India.

10. **Venkanna Kanneboina,** Ramakrishna.M and Pratima Agarwal, "c-Si/a-Si:H Heterojunction Solar Cells by Simulation and Experimental", "Department Day" 12th March 2016, Dept. of Physics, IIT Guwahati.

11. **Venkanna Kanneboina**, Ramakrishna Madaka, Mukesh Singh and Pratima Agarwal, "Spectroscopic Ellipsometry Investigation of Optical and Structural Properties of a-Si:H Thin Films" Abs Id: B3-12, pp: 71, "International Conference on Nanoscience, Nanotechnology and Advanced Materials" 14-17, December 2015, GITAM University, Visakhapatnam, India.

12. **Venkanna Kanneboina**, Ramakrishna Madaka, Mukesh Singh and Pratima Agarwal, "Effect of substrate temperature on structural and optical properties of RF sputtered ITO thin films for solar cell applications", Abs Id: PP183, pp: 32, "4th International Conference on Advanced Nanomaterials and Nanotechnology" 08-11 December 2015, IIT Guwahati, India.

13. **Venkanna Kanneboina**, Ramakrishna Madaka, Lalhriatzuala and Pratima Agarwal, "Spectroscopic ellipsometry studies on a-Si:H thin films deposited with electrode distance variation", Abs Id: PV-40, pp: 357, "18th International Workshop on Physics of Semiconductor Devices" 07-10 December 2015, IISc Bangalore, India.

List of workshops attended

1. **Venkanna Kanneboina,** "4th National workshop on NEMS/MEMS and Theranostic Devices" 26-28 February 2018, IIT Guwahati, India.

2. **Venkanna Kanneboina,** "One-Day workshop on Vacuum Technology and its Application in Optical Science" 19th August 2017, IIT Guwahati, India.

TH-2097_126121019

3. **Venkanna Kanneboina,** “National workshop on Advanced Probing Techniques in TEM” 15-16 February 2016, IIT Guwahati, India.

4. **Venkanna Kanneboina,** “Research Conclave”, held at IIT Guwahati during 23-26th March 2015, India

5. **Venkanna Kanneboina,** “National Workshop on Fluorescence and Raman Techniques” 13-19 December 2014, IISER Pune, India.

6. **Venkanna Kanneboina,** “IUCr workshop on X-ray diffraction systems and related applications”, 11-12th September 2014, IIT Guwahati, India.

7. **Venkanna Kanneboina,** “Workshop on MATLAB”, 22-23rd June 2013, IIT Guwahati, India.

TH-2097_126121019